https://ntrs.nasa.gov/search.jsp?R=19880016095 2020-03-20T06:40:00+00:00Z

NASA Contractor Report 4163

NASA-CR-4163 19880016095

Solid-State Combustion Synthesis of Ceramics and Alloys in Reduced Gravity

FOR REFERENCE

S. M. Valone and R. G. Behrens

PURCHASE ORDER C-80011-F
JULY 1988

NF01820

NASA Contractor Report 4163

Solid-State Combustion Synthesis of Ceramics and Alloys in Reduced Gravity

S. M. Valone and R. G. Behrens
Los Alamos National Laboratory
Los Alamos, New Mexico

Prepared for
Lewis Research Center
under Purchase Order C-80011-F

National Aeronautics
and Space Administration

Scientific and Technical
Information Division

1988

SOLID-STATE COMBUSTION SYNTHESIS OF CERAMICS AND ALLOYS IN REDUCED GRAVITY

FINAL REPORT

S. M. Valone
Tritium Science and Technology Group
and
R. G. Behrens
Nuclear Materials Process Technology
Materials Science and Technology Division
Los Alamos National Laboratory
Los Alamos, NM 87545

I. INTRODUCTION

A. SHS Processing of ceramics and alloys.

Refractory ceramics and alloys are known to exhibit one or more of the following properties: substantial chemical stability at high temperatures, resistance to chemical corrosion, radiation and mechanical wear, intrinsic hardness, and/or toughness. Such properties make refractory ceramics and alloys useful materials in a wide variety of structural and protective fields. Consequently, low cost manufacture of benchmark materials or particularly critical ceramics and alloys in space is of notable importance if the future development and production of advanced high technology systems in outer space is to play a significant role in the U.S. space effort. Also, there is a probability that the synthesis of ceramics and alloys in low gravity conditions may yield certain materials of improved properties which will find application as advanced materials on earth.

Current techniques for processing ceramic or alloy products usually require the initial synthesis of chemical compounds and alloys from their constituent chemical elements often represents one of the major technical difficulties in the overall manufacturing process. As examples, major technical problems associated with ceramic or alloy synthesis include:

* The need for temperatures on the order of 1800-3300 K along with chemically stable containment materials.

* Reaction time on the order of many hours are required for significant chemical reaction between chemical elements to occur.

* Contamination of the final product by unreacted materials or unwanted side products which may cause degradation of chemical and mechanical properties of the end product.

An alternative process for producing ceramics, alloys, and even ceramic composite materials, combustion synthesis, (also called self-sustaining or self-propagating high-temperature synthesis) has recently captured the attention of U.S. scientists because of its potential for economical processing of advanced materials for a wide variety of applications. Interest among U.S. scientists also stems from major research and technical successes reportedly achieved within the U.S.S.R. in producing a significant number of different materials by this process [1, 2].

The combustion synthesis process may be briefly described as follows. (See Figure 1.) A powder mixture of two or more chemical elements or compounds is pre-formed into some desired shape or placed into an appropriate container as a loose mixture. An electric heating wire (or some other thermal energy source) is placed in contact with the shape or loose powder in order to ignite the powder mixture. Upon ignition, an adiabatic chemical reaction between the chemical elements and compounds occurs with a significant release of heat (about 500 cal/g of reactant). The intrinsic heat released from the reaction propagates along the unreacted mixture as a combustion wave at typical velocities of 0.4 - 4 cm/s. Temperatures within the combustion wave front may be between 2000 and 4300 K depending on the chemical system. The final result of the combustion front passing through the powder mixture is "complete" conversion of the starting materials into a chemical compound or alloy.

As may be readily noted, some advantages of the combustion synthesis technique over conventional metallurgical powder synthesis techniques are:

* Heat for the chemical reaction (other than ignition) is supplied internal as a result of combustion. Therefore large, complex processing equipment and high temperature furnaces are not required. This should be especially advantageous for materials processing in Low Earth Orbit or on the lunar surface.

* Containment is often unnecessary.

* High-purity, near-net-shape ceramics and alloys can be rapidly produced.

* Synthesis times are short, on the order of seconds.

* Secondary products are not formed during synthesis in chemical systems where the reacting components are not significantly volatile.

* Adiabatic temperatures often are high enough to melt the ceramic being formed. This the ceramic can be cast into high-density complex shapes.

* Powers of high surface reactivity may be formed.

A wide variety of applications for SHS produced materials has been reviewed by Merzhanov [3].

Table 1 lists examples of exothermic chemical reactions currently being studied at Los Alamos. As can be seen from the table, adiabatic combustion temperatures for these systems are greater than 2000 K and the chemical systems being studied cover a wide range of ceramics and ceramic composite materials. Reactions 9 through 12 presented in Table 1 are examples of other solid-state exothermic processes which may be of importance to materials scientists and engineers. Reactions 9 and 10 produce ceramic oxide + silicon carbide composite materials which are known to exhibit increased fracture resistance over that exhibited by silicon barbide alone [4]. These chemical systems are of direct interest to NASA-LeRC and are being synthesized by combustion at Los Alamos in conjunction with the NASA-LeRC structural ceramics programs. Reaction 11 is also of interest to NASA-LeRC as it may be used to form a nickel dispersed and silicon carbide material. These ceramic composite systems also may prove to be possible benchmark reactions for future study under reduced gravity conditions.

Reaction 12 is similar to Reaction 9 except that reaction 12 uses sodium peroxide rather than using SiO_2 as an oxidizer. Reaction 12 also has a much higher adiabatic temperature than does reaction 9. The final product of reaction 12 (a ZrO_2 + SiC composite) should be similar to that formed by reaction 9 as the sodium in reaction 11 readily volatilizes from the reaction mixture during combustion.

Each of the example exothermic reactions listed in Table 1 involves either a completely melted or partially molten phase of at least one reactant and/or product. In the fluid state, mixing is strongly influenced by the presence or absence of gravity through a variety of buoyancy and convection processes. The magnitude of a gravitational effect on combustion in some or all of these systems may conceivably be large enough that the mass transport generated by gravity successfully competes with all other transport processes, most notable diffusion from density and temperature gradients. In turn, the mixing of reactants and/or products in solid-state exothermic systems such as those described above frequently, if not universally, control many of the crucial

TABLE 1. Exothermic Reactions Being Studies at Los Alamos

Reaction	Adiabatic Combustion Temperature (K)*	Heat of Reaction at 298 15 K (kcal mol^{-1}
CERAMIC SYSTEMS		
1. $Ti(s) + C(s) = TiC(s, l)$	3050	-44 0
2. $Zr(s) + C(s) = ZrC(s, l)$	3400	-48.0
3. $Hf(s) + C(s) = HfC(s, l)$	3900	-55.0
4. $U(s) + Te(s) = UTe(s, l)$	2013	-43.6
5. $Th(s) + Te(s) = ThTe(s)$	2243	-58 0
METAL - METAL SYSTEMS		
6. $3Ni + Al = Ni_3Al$	1543	-37.6
METAL - CERAMIC SYSTEMS		
7. $7Al(s) + 5Ni(s) + Fe_2O_3(s) = 2Fe(s, l) + Al_2O_3(s) + 5AlNi(s)$	2570	-344 6
CERAMIC-CERAMIC AND METAL-CERAMIC COMPOSITES		
8. $3Ti(s) + B4C(s) = TiC(s) + 2TiB_2(s)$	2900	-164.0
9. $Zr(s) + SiO_2(s) + C = ZrO_2 + SiC$	2326	-61.7
10. $4Y(s) + 3SiO_2(s) + 3C(s) = 2Y_2O_3(s) + 3SiC(s)$	3150	-309.0
11. $Si(s) + 2NiO(s) + Zr(s) + C = ZrO_2(s) + SiC(s) + 2Ni(s, l)$	3023	-164.8
12. $Na_2O_2(s) + Si(s) + Zr(s) + C(s) = ZrO_2(s) + SiC(s) + 2Na(g)$	3000	-105.0

*Assuming products are heated from 298.15 K

properties of the chemical reaction such as reaction rate, ignition characteristics, aggregate state and stratification of products, degree of reaction completeness, and structure of the combustion wave. Thus studying these or similar reactions under reduced gravity environments will add to our understanding of gravitational effects on physical and chemical phenomena such as solid and fluid phase mixing and dispersion, and on combustion kinetics and mechanisms. This will be discussed in further detail below.

B. Motivation for the Proposal.

There are three sources of evidence suggesting the possibility of microgravity effects on the combustion process. One is micrographic evidence of melting in Ti + C combustion products. In addition, there is visual evidence of melting in the form of slumping during combustion in both the Ti + C and the Ni + Al systems. Another is the thermodynamic arguments that melting temperatures are reached during the combustion process at least in an adiabatic approximation. Finally there is the dimensional analysis of the Ti + C system which suggests that the temperature and density gradients are sufficiently large that natural convection and reactive diffusion are of comparable importance, as measured by the Peclet number for the system.

The dimensional analysis proceeds as follows. An estimate of an order of magnitude value for the convective velocity is obtained using two crude models of fluid flow in a porous system. The corresponding Peclet number [5] is then computed. This number indicates the relative importance of convection and diffusion.

The following represents physical properties which may describe the reaction front in solid-state combustion:

* Kinematic viscosity, $\nu = 10^{-3}\ cm^2\ s^{-1}$
* Coefficient of thermal expansion, $\beta = 10^{-5}\ K^{-1}$
* Temperature variation, $\Delta T = 10^3\ K$
* Density, $\rho = 1\ g\ cm^{-3}$
* Density variation, $\Delta\rho = \rho$
* Diffusion constant, $D = 10^{-4} - 10^{-5}\ cm^2\ s^{-1}$

We take as a characteristic length $L = 10^{-3}$ cm, a typical titanium particle size, in our consideration of the flow of molten titanium and for consideration of density variations. On the other hand, we take $L = 10^{-2}$ cm, which is a typical distance in front of the reaction zone over which temperature decreases from the adiabatic combustion temperature (3050 K) to the melting temperature of titanium (1933 K), for consideration of thermal variations. Also, for convenience, we take the earth gravitational constant to be $10^3\ cm\ s^{-2}$.

First, consider the flow of molten titanium under gravitational forces. The velocity for viscous flow down a tube is estimated by [6]:

$$v \sim \frac{gL^2}{\nu} \sim \frac{10^3 \cdot 10^{-6}}{10^{-3}} \tag{1}$$

$$\sim 1 \text{ cm s}^{-1}$$

Next, consider flow in a gravitational field due to temperature and density gradients. The Grashof number, Gr, is ordinarily used to characterize the relative importance of buoyancy and viscous forces. For thermal gradients (30),

$$Gr \equiv \frac{\beta g \Delta T L^3}{\nu^3} \sim \frac{10^{-5} \cdot 10^3 \cdot 10^3\, 10^{-6}}{10^{-6}} \tag{2}$$

$$\sim 10,$$

while for density gradients,

$$Gr \equiv \frac{g \Delta \rho L^3}{\rho \nu^2} \sim \frac{10^3 \cdot \rho \cdot 10^{-9}}{\rho \cdot 10^{-6}} \tag{3}$$

$$\sim 1.$$

In either case, the characteristics velocity induced by thermal or density gradients is on the order of 1 cm s^{-1} [7]. The Peclet number, Pe [5], is on the order of:

$$P_e \equiv \frac{vL}{D} \sim 1 - 100. \tag{4}$$

On the basis of these estimates, free convection may be an important transport mechanism in solid-state combustion systems. If we perform the same analysis using $g = 10^{-1}$ cm s^{-2} (10^{-4} g_{earth}), the corresponding Peclet number is decreased to the range 0.01 - 0.1. This suggests that convection as a mass transport mechanism is for the solid-state combustion of titanium and carbon, and possibly for the combustion of other ceramic and alloy systems as well.

On this basis, one argues for gravitational effects in the following manner. In the steady combustion regime, the square of the propagation velocity, u, is roughly proportional to the product of the reaction rate, k, and the thermal conductivity, a [8]:

$$u^2 \sim ka. \tag{5}$$

The result follows from the sharply localized spatial distribution of the reaction front. At this point, no mechanism for the reaction or for the transport of reagents is assumed, although the mechanism is known to influence the proportionality constant in Eq. (5). Existing models [9, 10] typically go on to assume a diffusion controlled reaction, decomposing k as

$$k=2D/r^2, \tag{6}$$

where D is the diffusion constant for the process and r is an effective reaction length scale.

It seems natural to assume that r is related to the metal particle size. Given this model, and other things being equal, the analysis presented in the proposal indicates that the effective reaction length in a gravitational field could be reduced by as much as a factor of two,

$$r_g/r_0 \sim 1/2 \tag{7}$$

where r_g and r_0 are the reaction length scales at one earth gravity and in a microgravity environment, respectively. On the basis of Eqs. (5) and (6), one would expect a two-fold decrease in the propagation velocity in a microgravity environment.

This prediction contradicts observations in the form of recent centrifuge experiments by Kirdyashkii and coworkers [11] in which almost no gravitational effect is seen. We argue below that the predicted microgravity effect is masked by other convective mechanisms, primarily wall-contact and surface-tension driven forces. While this notion is not entirely new, the masking mechanism to be presented below differs markedly form the prevailing view of the process [9, 10] in that the capillary action of the molten components on the nonmelting or higher melting component is not the dominate mechanism.

There are two main reasons for abandoning the prevailing view. The first is that little of the void space consists of capillaries. This is because the low melting component tends to be softer and is compressed during the compaction of forming a sample. That is the void volume is usually unevenly distributed between the two components. The second is that computer simulation [12] show that the time scale for rearrangement of molten particles is comparable to that for capillary spreading. A third reason is that the capillary model is hard pressed to explain certain results such as the milling experiments of Epishin and Pityulin [13] and the laser ignition studies of Fredin and coworkers [19]. We note that the centrifuge experiments do conform to a plausible, although not unique, explanation in terms of capillary action. The reaction length used there is inconsistent with the one used by Olkolovich et al. [9] and Nekrasov et al. [10], hereafter referred to as the OMKS model. In our model, the reaction length will be nominal size of the metal powders, while in the OMKS model, the value of the nonmelting component is used.

C. Proposed Tasks

This program attempted to combine experimental and modeling research to investigate microgravity effects on refractory ceramics, alloys, and ceramic composite materials formed by solid-state combustion. The tasks incorporate wetting experiments, combustion experiments, fluid flow simulations and modeling, thermodynamic modeling, and molecular dynamics simulators in an effort both to gain a more complete view of the combustion process and to assess the influence of gravity on it. Model systems are chosen for their suitability for showing microgravity effects. In this case we have focused on the Ti + C and Ni + Al systems. The ceramic composite is chosen for its interest to the contractors.

The program is broken into six tasks, each of which will be discussed in more detail below:

1. Perform wetting experiments of titanium pellets on dense graphite to measure both the dynamic and the etatic contact angles.

2. Perform fluid flow simulations of the wetting process on a microscopic scale to examine the detailed nature of the flow field and to explore possible microgravity effects.

3. Perform a series of combustion experiments on the Ni + Al systems to measure the combustion velocity as a function of propagation direction and to examine the microstructure of the products for gravitational effects.

4. Combine the results of tasks 1-3 and evidence from the literature into a comprehensive fluid flow model showing the influence of gravity on the combustion process.

5. Explore the combustion conditions most favorable for the foundation of ceramics compositions from a SHS process.

6. Explore the reactivity of the Ti + C system at an atomic level through molecular dynamics simulations.

The results for each task are described in detail in the next section.

II. RESULTS

A. Wetting Experiments

Background

The aim of this project has been to explore the possible interaction of gravity with the wetting dynamics which take place during a combustion reaction between titanium and graphite powders. Since wetting of the carbon by molten metal seems to be such an important feature of

the process and the literature on the subject is very sparse, we decided to perform our own measurements of the static contact angle. However, given the dynamical nature of the wetting process in the combustion reaction, the study of the dynamic contact angle, that is, the dependence of the contact angle on the spreading front velocity is also deemed appropriate. To this end, we provide a brief review of the main concepts of dynamic contact angles and their measurement.

The primary relationship thought to hold for dynamic contact angles is that they increase monotonically with increasing velocity. We wish to examine this empirical statement for a case of wetting accompanied by a reaction and melting. Typically there is a range of contact angles which product no movement in the fluid and consequently renders the static contact angle nonunique. This often referred to an contact angle hysteresis.

Frequently, hysteresis is caused by surface roughness, although this need not be the only cause. In spite of the roughness in these experiments, the value of the static advancing contact angle is very reproducible [15, 16].

Capillary studies of dynamic contact behavior are the most popular methods. However, the high temperatures and the requirement of melting the metal during the experiment make this alternative impractical. The next most popular method is to photograph the spreading of droplets on a flat surface. Here the flat surface is a disk of Poco graphite [17]. The droplet is replaced by a section of Ti rod which subsequently melts in the rf field as a part of the experiment. Unsteady behavior is the hallmark of the method. Abundant examples of this occur in the results reported below.

A variety of analytical procedures are available from the literature for relating the instantaneous geometry of the sample to the apparent contact angle [18-21]. The first is a spherical cap model (Fig. 2) which relates the initial volume, V, and the instantaneous radius, r, to the apparent contact angle, θ_a, through the equation [15]

$$r^3/V = 3/\pi(1 + \cos\theta_a)\sin\theta_a/((1 - \cos\theta_a)(2 + \cos\theta_a)) \tag{8}$$

or,

$$h/r = (1 - \cos\theta_a)/\sin\theta_a, \tag{9}$$

where h is the height of the apex. Because some molten material penetrates the solid substrate during the experiment, the latter relationship is used in analyzing the film data. In addition, it is used to find the static contact angle from the samples after the metal has resolidified.

In viewing the high-speed films, it is obvious that during most of the experiment the system is not spherical but trapezpoidal due to the presence of the melt front. This naturally suggests the

use of a trapezoidal model to calculate an apparent contact angel from geometric information. From Fig. (2), we have the relationship

$$\theta_a = \arctan[2h/(2r-d)], \tag{10}$$

where d is the original diameter of the metal cylinder.

Next there is an empirical relationship between dynamic contact angle and the front velocity and the static contact angle due to Hoffman [18]. A correlation curve gives contact angles of no greater than 12° in the velocity range of the experiment. This is considered unusable for our purposes. Given that the relationship is empirical, it is of little value to explain the deviation.

Finally, the present system exhibits both thick (secondary) and thin (primary) fronts as is observed in other systems [22, 23]. The presence of the thin film can be seen both in the photography and the final product. In the films, the luminance of the substrate changes markedly as the thin film passes. In the resolidified samples, the presence of the two fronts is self-evident.

Design

The experiment consists of six sections of Ti rod set on six different Poco graphite substrates. The samples are placed inside a radio frequency (rf) field produced by a Lepel 30 kW induction heating unit operated at 376 kHz, a very unique feature of these experiments (Fig. (3)). The rf field couples primarily to a carbon suspector which, in turn, heats the Poco graphite substrate which heats the Ti pellet to its melting point. Each metal pellet is approximately 3 mm in diameter and 4 mm high. This size is chosen to prevent fluid from spilling over the edge of the substrate. The substrates are 25 mm in diameter and 13 mm thick. A 0.5 mm diameter, 3 mm deep hole is bored into the top of the substrate to allow pyrometric measurements of the substrate temperature.

Another unique feature of this experiment is the high-speed filming technique used to record the wetting process. To gain adequate magnification, only the right hand spreading front and the melt front are in the field of the camera. Additional magnification comes from projection of the developed films on a screen to give roughly a factor of 400 enlargement. This allows location of fronts to within approximately 0.05 mm and angles to within 3°. The primary limitation in this particular set of experiments is the contrast between the thick and thin fronts and between the latter stages of the melt front and the thin front. The limitation can be substantially reduced by choosing different photographic settings. The framing speed is 185 m/s for the first sample and 123 m/s for the remaining five. The slower speed gives satisfactory temporal resolution.

The experimental stage is enclosed in a glass mandrel with a quartz window on the side for the high-speed camera to view the wetting process. In addition, the substrate temperature is monitored through a fast-response pyrometer viewing the black-body hole in the top of the

substrate from a right-angle mirror set on the top of the mandrel (Fig. (3)). The pyrometer is, in turn, connected to a two-scale strip chart recorder. The high-sped camera is set at a 10° angle to gain a slightly downward perspective on the fluid fronts. This angle is actually reduced by a few degrees during the experiment due to thermal expansion of the assemble.

To minimize arcing and to improve thermal equilibration, the system is baked at 1300 K in a 10^{-5} torr vacuum for 10 minutes and then back-filled with He to 100 torr.

After the bake-out period, the rf power is stepped up until the black-body temperature is approximately 1700 K. When the temperature reading becomes stable, in 30 to 120 s, the power is again raised to a level which ultimately gives a black-body temperature of approximately 2000 K. The required power level was found by trial and error in some preliminary runs, but is fairly reproducible.

When the power level becomes stable, the filming begins and the metal pellets metals within 1 or 2 s of this time. The procedure gives reproducible results. In earlier trials, longer bake-out periods and equilibration times at the 1700 K level were used with much less success.

Results

The high-speed films of six samples are analyzed for thin and melt front positions and observed apparent contact angle, picture contrast permitting, at 0.25 s intervals for the duration of the experiment. Rapid changes in the flow patterns when the sample first becomes fully melted dictated that the above quantities be recorded at intervals of 0.025 s. The positional data are then converted to velocities by simple first-order, forward differencing. In turn, the velocities are plotted against time along with the measured apparent contact angle.

Each pair of temporal plots may then be rearranged as a plot of contact angle verses velocity, that is the dynamic contact angle. Use of the two geometric models described earlier [15] allow for independent estimates of the apparent contact angle from the positions of the thick front and the melt front.

As an additional note, the velocity data for the post-melt phase (0.025 s resolution) are too noisy to analyze as is. This is not surprising because of the small differneces in positions and angles which result from the high temporal resolution. Consequently, all the velocities and contact angles are averaged in moving groups of eight points. For the larger time intervals, no averaging is necessary.

From Ref. (15), we have the conjecture that the dynamic contact angle always increases with increasing velocity:

$$d\theta/dv \geq 0, \tag{11}$$

which is a mathematical statement of monotoncity. For instance, the empirical correlation of Hoffman [18] embodies this notion and is supposed to be true for both positive and negative velocities, i.e. both advancing and receding fronts. In the present study, only advancing fronts can be studied because of the initial solid starting configuration.

As may be seen in Figs. (4)-(8), the relationship between contact angle and velocity is anything but monotone. From Figs. (9)-(14), the irregularity is apparently due primarily to oscillations in the front velocities. At the onset of melting, the velocity is large but then decays rapidly, in about 0.5 s, with the front sometimes even coming to a complete standstill. Whether or not there is any relationship between this behavior and that examined by Buckmaster is unknown [24]. This phase continues until the entire sample is melted. At that time the front velocity increases abruptly, again decaying rapidly, in about 0.2 s. A third spike occurs when the sample looses all vestiges of its solid cylindrical configuration and becomes a spherical cap (Figs. (10)-(14)). Here the decay is much slower as the sample approaches its final configuration. Unfortunately, the film contrast at the later stages of the experiment is insufficient to measure the thick front and the apparent contact angle. However, the general trend is clear.

Some undulation in the dynamic contact angle relationship is also possible from the apparent contact angle itself. The circumstance again arises because of the melt front which moves away from the substrate as the system evolves. In so doing, the reduction in contact angle due to spreading may be counteracted by the rising melt front to produce small oscillations in the observed contact angle.

From the final configurations, the static contact angle is measured to be $3.5^{\circ} \pm 0.5^{\circ}$ as derived from the final thick front diameter and apex (Eq. (9)). The region covered by the thin front is roughly twice as large in diameter as that covered by the thick front. In addition, there appears to be a very narrow ring (1-2 mm) of slightly greater luster at the transition between the thin and the thick fronts (Fig. (15)). However, metallography on samples from the preliminary trials assigned no special characterization to this region.

Our interpretation of dynamic contact results is that mechanical forces between the melt front and the substrate are coming into play. In particular, the front cannot advance faster than new molten material is produced. This is, of course, a function of the power of the rf field, the radiate and convective dissipation rates, and the sample-subtrate coupling. Close correlation between the thick front and melt front velocities is apparent in Figs. (10)-(14). Further, the surface tension of the molten material keeps the fluid profile from becoming too sharply curved (Fig. (2)). When the sample becomes fully melted, the mechanical constraints are relaxed substantially, although reminiscences of the cylindrical solid persist for most of the experiment. In this way, the first peak in the velocity plots of Figs. (10)-(14) may be understood. When the sample attains a spherical cap shape, the constraints are relaxed further which probably accounts for the second spike in these plots. The true decay to the static configuration can then proceed.

A more normal relationship between contact angle and velocity may exist during this final phase, but again, the lack of contrast prevents a direct measurement. On the other hand, in an actual combustion reaction, a melt front is apparently present for a large fraction of the time that spreading occurs. As is suggested by the experiments, the spreading rate itself is controlled by the melting rate. Consequently, the present experiments provide more insight into the mechanics of the reaction than a droplet experiment, were it possible to perform. As an aside, we note that the effect of the melt front is beyond the capabilities of the spreading simulations described below.

In Figs. (16)-(19), the spherical and trapezoidal models for the sample geometry are used to estimate the apparent contact angles from the thick and melt front positions. Comparison with the measured contact angle shows that the models consistently overestimate the contact angle. From the films, it is apparent that the fluid has a positive curvature with respect to the substrate while the spherical model requires a negative curvature. On the other hand, the trapezoidal model has no curvature and, consequently, gives a closer estimate of the contact angle than the spherical model. Toward the end of a trial, the two models begin to converge with the observed angles, although the lack of contrast at these latter stages again prevents a definitive view. We conclude that the presence of the melt front and the dominance of the cylindrical geometry prevent either of these sample models from adequately describing this type of experiment. A possible model might come from a solution of Young's equation in cylindrical coordinates with the proper mechanical constraint of the melt front imposed.

Finally, we conjecture that the speed of the thin front is too large for any surface diffusion mechanism to be significant [22, 23].

B. Wetting and spreading Simulations

The motivation behind microscopic level fluid flow simulations is a desire to observe the details of flow which are not readily available experimentally. There are a number of aspects of the SHS which may be explored through computational means. For example, parametric studies of the sensitivity of the wetting and spreading processes can be made, as can direct comparison with experiment through macroscopic simulations. One can also look at the applicability of the Poiseuille flow model, described below, and relied upon in Refs. 9 and 10. Furthermore, the actual number of variables in the problem may be controlled and arbitrarily changed to reveal the effects of each. The primary variable of interest here is, of course, gravity, although it appears in concert with a number of other variables.

The main tool in this study is the SOLAVOF code [25], which is designed to study 2-D, low speed flows with arbitrary free moving surface tracking. The code is of the eulerian, finite difference variety on a variably spaced rectangular mesh. Free surface tracking is achieved through the volume-of-fluid method [26], which permits any number of surfaces to appear at any location in the fluid. In addition, obstacles may be placed anywhere in the fluid, thereby allow-

ing a wide range of geometries to be explored. This code solves the 2-D Navier-Stokes equation, which means that no diffusive flow or heat flow is taken into account. Also the fluid density is assumed to be constant.

In the present study, the surface tension is fixed at 1400 g s^{-2}, the viscosity at 0.01 g cm^{-1} s^{-2}, the density at 4.11 g cm^{-3}, one earth gravity at 98 cm s^{-2}, and the contact angle at 10°.

As discussed in the Introduction, previous models of fluid flow in combustion synthesis reactions assume that capillary flow is the primary convective event. Characteristic length and times scales are defined which are consistent with the observed dependence of reaction velocity on metal particles size [10]. In the course of the numerical simulation for this project, fluid arrangement is found to be an equally important convective event brought on by spreading forces. In each model both the spatial scales and velocityies are comparable. Consequently, the time scales for fluid rearrangement are comparable to those for capillary flow. However, because the fraction of the system consisting of capillaries appears to be small the rearrangement event may be the important one.

A typical example of the fluid rearrangement process is shown in Figs. (20)-(24). Two things are demonstrated here. One, the initial degree of contact between the metal and the graphite is not a factor. Consequently, arguments that gravity can play a significant role in initiating contact between reagents are untenable. Two, the characteristic velocity for the rearrangement of molten Ti is 100 cm/s, which is much faster than the front progagation and diffusion rates. However, as stated above, this value is consistent with the centrifuge experiments of Kirdyashkin et al. [11]. In particular, substituting this value into Eq. (11) and solving for the g-force required to give comparable velocities yields 100 g for 1000 μm particles and 1000 g for 100 μm particles, where g is one earth gravity. As noted in other work, one expects the fluid motion to occur much more quickly than the reaction for these systems.

In order to account for this effect in terms of the OMKS model, a different length scale corresponding to the metallic particle size is required. However, this is inconsistent with the origin structure of the model. Furthermore, the OMKS model cannot account for the particle irregularity effect measured by Epishin and Pityulin [12]. Figures (25)-(27) show that the fluid rearrangement velocity is increased to the extent that the code has difficulty handling the simulation.

To take a step further, we attempted to couple the fluid rearrangement with the capillary flow. Because of the radical change in spatial scales in such a problem, we were unable to complete the simulation. The calculation is far too expensive and time consuming to justify.

There are two other phenomena noted in the calculations which we wish to report here. The first is that for certain fluid diameter to cell sizes, one sees a difference in the final configurations

in gravity and microgravity (Fig. (28)-(29)) [11]. The second is a situation where two bubbles are placed one above the other (Figs. (30)-(32)). Again the final configurations differ markedly between the gravity and microgravity situations. Both these simulations are in a high symmetry initial configuration and it is not clear how likely such an occurrence is a real system. In a real system, forces generated by natural asymmertries are generally expected to mask these effects. To the extent that such situations do occur, the product microstructure in a gravitational environment is expected to be proportionately coarser than that produced in a microgravity environment.

With respect to the wetting experiments, the SOLVAVOF code cannot, as it stands, simulate either the progress of a melt front or a dynamic contact angle. The experiments show that the dynamic contact angle and spreading rates may be substantially influenced by the behavior of the melt front and the geometry of the unmelted portion of a metal particle. Also the gravitational effects. Conceivably then, previously established points of contact between reagents can actually be broken, at least temporarily, as a result of this movement.

Finally, we wish to comment of the relative rates of diffusion and spreading. That is, the fact that only minor gravitational effects are seen in Ref. (10) suggest that the spreading-induced convection persists for times comparable to the reaction time. Otherwise, if these were relatively short lived, then it would be possible for the combustion process to occur by a step-wise, rather than a concurrent, mechanism in which gravitational forces could influence a slow diffusion process.

C. Fluid Flow Modeling

In order to understand the objectives and approach of this program, it is first necessary to understand the form of the reaction rate which we consider appropriate for this class of condensed phase reactions. Amplifying on a theme which has been sounded in previous work in more restricted forms [27, 28], we observe that in condensed phase systems, a reaction proceeds by migration of reagents across an interface. Consequently, the area of contact between reagents can control the flux of material available for reaction at a given time and, thus, the macroscopic reaction rate. To localize this notion, at any given time, we assume the existence of a specific area of contact per unit volume, S, of the reagents [28]. Initially S may be independent of location in the sample, but as the reaction proceeds, it must be allowed to vary with location. More importantly, at nay one location in the sample, S will evolve in time due to the aforementioned mixing forces. Consequently, the notion of the time evolution of the specific area of contact forms a cornerstone of our later discussion.

Within this framework then, the reaction rate at some point in the sample is given by the product of the specific area of contact and the temperature and concentration of reagents. Quantitatively, the overall reaction rate may be expressed as

$$r = k_i S. \tag{12}$$

The temperature and concentration dependence convey a spatial variation to k_1, and, thus to r, independent of the spatial dependence of S. It is important to note that we assume that k_1 is independent of morphological factors such as green density, particle size, macroscopic stoichiometry, and agglomeration state of the reagents. We take the physically sensible position that these morphological factors are isolated in S.

There are several advantages in this formulation. The most important of these is that the microstructural influences and the chemical kinetic influences are largely isolated. This is important both experimentally and theoretically because it suggests that information about the two factors may be garnered from separate experiments or from theories of model systems where some degree of control might be obtainable. Furthermore, as stated above, the notion of separating the rate constant, as in Eq. (12), provides a natural stage on which the influence of various convective forces (such as wall adhesion, surface tension, and gravity) on the combustion synthesis process might be understood. As a natural outcome, the concept suggests a possible explanation for some laser ignition phenomena [14, 28] and suggests the possibility that samples composed of the same materials with the same particle size distribution, but with different surface roughness, may have different reaction rates, r.

One further topic must be discussed before moving on to the objectives of this program, and that is to give a brief account of an earlier treatment of capillary flow rates and their role in combustion synthesis [9, 10]. In the usual treatment of capillary flow [24, 30], a reservoir of material is present to sustain some steady boundary pressure which, when coupled with a curved surface, drives the flow. The reservoir itself does not experience changes due to any number of capillary flows in any direction. The flow velocity is given approximately by a Poiseuille model [6, 9, 10, 30], namely,

$$v = \sigma\cos(\theta)R/(8H\mu), \tag{13}$$

where σ is the surface tension, θ is the contact angle, R is the capillary radius, H is the fluid height in the capillary at some instant in time and bears the relationship $dH/dt = v$ to the flow velocity, v, and μ is the coefficient of viscosity. This relationship appears valid for times greater than the viscous transient time, $R\rho/\mu$, where ρ is the fluid density, and may be solved analytically for constant physical properties [30]. In Refs. 9 and 10, two regimes of combustion propagation are identified as a consequence of Eq. (13). One regime is comprised of situations where complete spreading is much faster than either the characteristic time of reaction or the characteristic time of natural convention. In this instance, the spreading rate has a small influence on the rate of propagation of the reaction front, permitting other forces, such as diffusive or convective influences, to dominate the process. A second regime is comprised of situations where spreading times are sufficiently large that the formation of products interferes with the completion of spreading. The particle size of the melting component controls which regime dominates when the size of the nonmelting component is fixed. The first regime is called the kinetic regime and the second is called the capillary regime [9, 10].

In terms of Eq. (12), the preceding discussion is significant because the time evolution of S depends on the spreading velocity, one approximate form of which is given by Eq. (13). The precise nature of the velocity dependence of S is unknown at this time and is left unspecified. Under certain conditions, the subsequent discussion suggests ways in which this capillary velocity may be altered by forces which are small relative to the capillary force. Under other conditions, the time evolution of S is so rapid that it is relatively unimportant to the reaction rate, thereby allowing others forces to dominate the process.

The potential role of gravity in the SHS process is bound up with two underlying assumptions in the analysis of Refs. 9 and 10, namely, that microscopic molten particles behave the same as macroscopic systems in contact with reservoirs, and that the particles of reagents are initially in contact. Our reasoning is guided by two overriding features of these systems. One is that the potentially molten components of the system are comprised of microscopic grains, typically less than 200 microns in diameter. One might wonder if a microscopic molten particle subjected to several spreading forces at different locations on the grain and in different directions behaves in the same way that a macroscopic system behaves. If this rate is substantial altered in a microscopic environment, the capillary velocity, which is driving the time evolution of S, is being reduced, thereby changing the amount of time over which gravitational and diffusive forces may act.

In a previous section we argued in a dimensional fashion that gravitational effects may measurably alter the combustion rate of certain sold-state combustion reactions used in the synthesis of ceramics and alloys. Without estimating an actual value for the effect, the suggestion was made on the grounds that the diffusion rates which contribute to the reaction and natural convective motion ought to be of the same order of magnitude. The goal of the program has been to perform a set of wetting experiments to gain insight into the wetting process and to obtain quantitative information about the contact angles involved. In addition, detailed hydrodynamic simulations were to be performed to study the microscopic character of the wetting process. The primary focus of the program is on the Ti + C reaction which has been widely studied by others. In the following, quantitative estimates of the various concective mechanisms are made. In turn, a simple model of the mixing behavior of the system is used to show how spreading and wetting forces mask the proposed gravitational effects.

In the following we assume that the conversion rate for Ti + C is proportional to the flux of carbon into the molten Ti. That is

$$r = d\eta/dt = k_i S(t) \tag{14}$$

where η is the fraction of conversion to product, S(t) is the instantaneous local area of contact between reagents in the reaction zone and k_i is an intrinsic rate of reaction at a "well-established"

interface. Then we are claiming that k_1 is equal to the time rate of change of the fractional carbon concentration, C, in the molten Ti,

$$k_1 = \partial C/\partial t \tag{15}$$

By the equation of the continuity,

$$k_1 = \partial C/\partial t = -\nabla \bullet J_C, \tag{16}$$

Where D is the diffusion constant for the problem and v_{T1} is a characteristic convective velocity for the molten Ti during the reaction. Then K_1 becomes

$$k_1 = D\, d^2/dx^2 - v_{T1} dC/dx \tag{18}$$

To simplify matters further, we take a spatial average of Eq. (18) over Δx to give the reaction,

$$k_1 = 2D/\Delta x^2 + | v_{T1} | /\Delta x, \tag{19}$$

where d^2C/dx^2 has been approximated by $2/\Delta x^2$ and dC/sx by $2x/\Delta x^2$.

Again, Δx is taken as the nominal metal particle size which should be comparable to the reaction length. Recall also that in the OMKS model, Δx is taken as the carbon particle size. The absolute value of v_{T1} is assumed since the concentration gradient is always taken to be opposite the effective flow direction. Finally we note that by factoring Eq. (19), the Peclet number, Pe, [5] of the process appears naturally within the model,

$$k_1 = D(2+Pe)/\Delta x^2 \tag{20}$$

where $Pe = | v_{T1} | \Delta x/D$.

In the dimensional analysis, we estimated that Pe would fall between 1 and 10 if gravity were the main source of convection in the system. Obviously this is not the case, given the mechanisms discussed above. For simplicity, we divide v_{Ti} into two parts, one due to wall-contact spreading and surface-tension driven shape rearrangement and another due to gravity,

$$v_{T1} = v_s \pm (g\Delta x)^{1/2}, \tag{21}$$

where the sign depends on the direction of the mass force. Then the intrinsic reaction rate becomes,

$$k_i = D(2+[v_s \pm (g\Delta x)^{1/2}]\Delta x/D)/\Delta x^2. \tag{22}$$

Within this framework, we see that diffusion provides only one mechanism of reagent transport, while gravity, wall-contact, and surface tension provide others of the convective type. Furthermore, the competition between gravity and the other convective modes (hereafter referred to as spreading) is clearly brought out. In particular, we see that if $v_s >> (g\Delta x)^{1/2}$, as is expected for small g, highly irregular metal particles, and/or small metal particles, gravitational effects will be masked. With respect to the Peclet number, one obtains contributions from both sources, but that from the spreading will be shown to be one to two orders of magnitude larger than the one due to gravity. On the other hand, if v_s were zero as assumed in the proposal, then Eq. (22) in conjuction with Eq. (5) predicts a 20% difference in the combustion velocity between earth gravity and a microgravity environment. The discrepancy in this model versus the one based on Eq. (6) comes from the direct change in the effective reaction length resulting from natural convection. In either case, the prediction is too large relative to those found in the experiments. The convective model of Eq. (22) with spreading velocities on the order of 100 cm/s give much more the correct order of magnitude.

In another vein, gravitational effects can effect the area of contact between reagents through the fractional surface term, S(t). In a qualitative sense, S(t) may be expressed in terms of the initial area of contact per unit volume, A_0, the total area of nonmelting reagent per unit area, A_C, and the characteristic velocity of Eq. (21):

$$S(t) = [A_0+\pi(|v_{T_1}|t)^2]/A_C. \tag{23}$$

Strictly speaking, the time evolution of v_{T_1} is required here, otherwise S(t) would grow beyond its limiting value of 1. The details of the evolution of the convective velocity are far too complicated to follow and so we limit the time to that required to give a unit value for S(t). For longer times, S(t) would just be unity. An additional significance to the contact area factor arises from the fact that A_C also characterizes the carbon particle size. Rate effects associated with variation in the carbon particle size would appear here.

The gravitational effect appears in a manner similar to that found in the intrinsic rate constant. The dependence is embodied in Eq. (21). Consequently, the same arguments about when gravitational effects are important to the process hold. Again, in the proposal, the spreading velocity is assumed to be zero so that potentially large gravitational effects might occur due to buoyancy. Of course, we now know through the simulations that even with very little initial contact, the spreading process is quite rapid. We will also see that particle irregularity substantially enhances the spreading rate. We refer to this situation as a masking effect.

Finally, we note that similar arguments about the influence of convective motion on the time evolution of the thermal conductivity of the sample. However, we will not pursue this topic here.

D. Burn-up, Burn-Down Experiments

Titanium and carbon readily ignite and combust to form the ceramic titanium carbide, TiC. If this condensed phase reaction occurs adiabatically, the temperature in the combustion wave front is calculated to be 3290 K. This temperature is considerably greater than the melting temperature of titanium metal (T_m = 1933 K) and also happens to be the melting temperature of TiC. Accordingly, sufficient heat is released in the combustion of Ti + C to not only raise the temperature of TiC to its melting point, but also to melt approximately 30% of the TiC formed in the process. Indirect confirmation that partial melting of TiC occurs has been obtained by us as well as other researchers. Metallographic observations indicate that a eutectic-like structure is present throughout the TiC product. In addition, evidence exists to suggest that molten titanium in the combustion wave front readily wets and spreads around the graphite flakes during progagation of the combustion wave.

During this report period we attempted simple combustion experiments which were designed to ascertain whether gravitational effects on the combustion rate and on the product TiC microstructure could be observed and which could be attributed to the presence of molten titanium and/or partially molten TiC in the combustion wave front.

These experiments were performed in an inert atmosphere glovebox to prevent oxidation and/or nitridation of the materials during the high-temperature combustion. Cold-pressed cylinders of -325 mesh titanium power and flake, spectroscopic grade graphite were formed at 25,000 psi using a Carver press and steel dies and punches. The pellets had approximate green densities of 60% of theoretical.

The pellets were situated in a vertical position for ignition on either the "top" or "bottom" surface. Pellets were also ignited and combusted in a horizontal configuration. We took care to ensure that heat sinking at the end of the pellet opposite to the ignition end was similar in all configurations.

Ignition was achieved using a resistively heated tungsten wire spiral filament. The pellets were approximately 0.6 in. high and 0.25 in. in diameter. The pellets grew to about 0.7 in. in height as a result of the combustion process.

Propagation of the combustion wave was photographed at 1000 frames/sec using the NAC high-speed camera. Figure 33 shows the results of a series of the high-speed photography experiments. This figure shows a plot of wave front position along the pellet (as projected on the viewing screen) as a function of frame number (time). Pellet 7-3-84-1 was ignited on the "bottom", which combustion wave propagation "upward". Pellet 7-3-84-2 was ignited on "top", with

combustion wave propagation "downward". Pellet 7-3-84-3 was ignited and combusted in a horizontal position.

As indicated in Figure 33, there are no noticeable differences in the measured combustion wave propagation velocities for all three pellets. The decrease in combustion wave velocity with time is due to the slow achievement of steady-state combustion during the course of the experiment. For all practical purposes, steady-state combustion has been achieved for times greater than 1 second.

Combustion of Intermetallic Alloy Systems.

Combustion experiments, similar to hose performed for the Ti-C system, were performed for several alloy compostitions in the Ni-Al and Fe-Al systems. These binary metal systems, particularly the Ni-Al system, are of interest to this work for reasons stated in the previous section of this report.

The Ni-Al and Fe-Al systems contain several intermediate alloy phases which are sufficiently stable (i.e. have high negative enthalpies of formation) to support combustion wave propagation. Also, many of these intermediate phases exhibit wide homogeneity ranges. Figures 34 and 35 present the phase diagrams for the Ni-Al and Fe-Al systems respectively [31]. Tables 2 and 3 summarize pertinent thermodynamic data for the Ni-Al and Fe-Al systems respectively. As can be seen from the tables, adiabatic combustion temperatures are high; in several cases they are greater than the melting temperature of the alloy phase. The adiabatic combustion temperatures are also greater than the melting temperature of aluminum (T_m = 933 K), and in several cases, greater than the melting temperature of nickel (T_m = 1726 K), but never reach the melting temperature of iron (T_m = 1809 K) in the Fe-Al system.

Cylinderical pellets containing 5 micron diameter nickel and 6 micron aluminum spherical powder were prepared according to the following stoichiometries: AlNi, $AlNi_3$, Al_3Ni_2, and pressed at 30,000 psi into green bodies 0.500 in. in diameter x 0.500 in. high. Pellets 0.650 in. in length were also prepared. These pellets were then combusted "top" to "bottom" or "bottom" to "top" in the inert atmosphere glovebox (to prevent oxidation) and the combustion wave propagation photographed with the high-speed camera. Similarly, cylindrical pellets containing 5 micron diameter nickel powder and iron powder (unknown particle size) were prepared according to the following compositions: Al_6Fe, Al_2Fe, Al_3, Al_5Fe_2, and AlFe. These pellets were also combusted "top" to "bottom" to "bottom" to "top" in the glovebox and the combustion event photographed.

Each combusted pellet was sliced in half and sent to Janet Hurst, Lewis Research Center, for metallographic examination to determine if any differences in morphology are present due to the direction of combustion wave propagation.

Analysis of the high-speed photography showed that combustion wave propagation in these metallic systems was not smooth as was observed in the Ti + C combustions. The combustion waves appeared to move partially through the sample pellet, stop, and then reignite. This process occurred in a step-wise fashion throughout the pellet. Also, hot-streaks were observed to travel radially around the pellets as the combustion wave moved along the pellet axis. These phenomena did not appear to be related to the direction of combustion wave propagation. Also, we did not observe any differences in axial combustion rates as a function of burn direction.

As a result of one of us (R. G. Behrens) attending the dedication ceremonies for the Microgravity Materials Science Laboratory (MMSL) at Lewis Research Center, we proposed ancillary experiments on the Ni-Al and Fe-Al systems to be performed in the MMSL electromagnetic levitator/drop tube apparatus. The initial idea was to use this facility in a novel way by studying combustion during a 1 second free fall drop. It appeared from first-hand observation of the apparatus that the combusting pellets could not (unfortunately) be photographed using high-speed photography during the drop. To do this would require a more costly experiment in one of the Lewis drop towers. However, we believed we could gain information about possible differences in product morphology and microstructure for times immediately before the drop and during the 1 second drop. A 1 second drop time should be sufficient for the combustion wave to travel the length of a 0.5 cm long Ni + Al pellet.

Table 2. Thermodynamics of the Nickel-Aluminum System

Alloy Composition	ΔH^o_f (298.15 K) (kcal mol^{-1})	$T_{adiabatic}$ (K)	$T_{melting}$ (K)
Ni_3Al (alpha prime)	-37.6	1543	1660
NiAl (beta prime)	-28.0	2153	1910
Ni_2Al_3 (delta)	-67.5	1988	1830
$NiAl_3$ (epsilon)	-36.0	1393	1390

Table 3. Thermodynamics of the Iron-Aluminum Systems

Alloy Composition	ΔH^o_f (298.15 K) (kcal mol^{-1})	$T_{adiabatic}$ (K)	$T_{melting}$ (K)
Al_3Fe (theta)	-26.7	1437	1423
Al_5Fe_2 (eta)	-35.0	1150	1430
AlFe (beta prime)	-12.0	1316	1600
Al_2Fe (psi)	-18.7	1358	1426

Consequently, we sent a number of green body Ni + Al and Fe + Al pellets of various sizes to Janet Hurst to see if they could be electromagnetically levitated without achieving combustion. If this is shown to be feasible, then we can ramp the temperature of the levitated unreacted pellet to achieve ignition, and then drop the combusting pellet in free fall.

E. Thermochemical Modeling

Introduction

The purpose of this research was to gain an understanding of the high-temperature chemistry associated with the synthesis of ceramic carbide/oxide composites by self-propagating high-temperature synthesis (SHS). In particular, we were interested in studying the synthesis chemistry of the Y_2O_3/SiC and ZrO_2/SiC composite systems.

Preliminary work in our laboratory at the Los Alamos National Laboratory showed that an appropriate stoichiometric mixture of yttrium, silicon idoxide, and graphite will react exothermically. However, the product which was formed was not the desired Y_2O_3 + SiC mixture, but rather was a complex eutectic-like material.

Preliminary attempts to ignite an exothermic reaction with an appropriate stoichiometric mixture of zirconium, silicon dioxide, and graphite (which was predicted to react and to form a ZrO_2 + SiC mixture) were not successful.

The approach used in the present work to further study the high-temperature synthesis chemistry of these two complex chemical systems involved using equiplibrium thermochemical modeling techniques. Parametric studies were performed to evaluate the effect of temperature and pressure on the gas and solid equilibrium phase relationships. (32) While system temperature and pressure were varied in a systematic manner, stoichiometry of the reacting materials was held constant according to the equations

$$4Y + 3SiO_2 + 3C = 2Y_2O_3 + 3SiC \tag{24}$$

$$Zr + SiO_2 + C = ZrO_2 + SiC \tag{25}$$

System pressures were varied between 10^{-4} atm and 10 atm, while temperatures were varied in the vicinity of the estimated adiabatic reaction temperature, 3150 K and 2326 K for reactions (24) and (25) respectively.

Thermodynamic calculations

The computer code SOLGASMIX-PV (32) computes the equilibrium composition of a multicomponent chemical system by the direct minimization of the total free energy of the system. This program also operates under the constraints of conservation of mass and either

constant pressure or constant volume. The Gibbs phase rule is also satisfied. Equilibrium thermodynamic calculations are possible for systems containing a gas phase, condensed phase solutions, k and condensed phases of either invariant or variable stoichiometries.

Input thermodynamic data used in the present calculations consisted of the standard enthalpies of formation at 298.15 K, $\Delta H^o_f(298.15K)$, and Gibbs free energies of formation, $-\Delta[G^o(T) - H^o(298.15K)]/T$, for all vapor and condensed phase species. Most of the thermodynamic data used here was abstracted from the JANAF Thermochemical Tables (23). Exceptions were data for various yttrium-containing compounds. Data for these compounds were obtained using standard schemes for estimating high-temperature thermodynamic functions [34]. Table 4 shows representative data for the Y-Si-C-O system at 2400 K. The table also summarizes the vapor phase and condensed phase species considered in the calculations. Table 5 presents similar information for the Zr-Si-C-O system at 2000 K.

In the present work the number of moles of elemental reactants was held constant while the system pressure and temperature were varied. As such, condensed phase stability diagrams were calculated for the Y-Si-C-O system at a stoichiometry of Y:Si:C:O = 2:1.5:1.5:3 (which corresponds to the stoichiometry of Eq. (24)) while the system pressure was varied between 10^{-4} atm and 10 atm and the temperature was varied between 2000 K and 3200 K.

Similarly, the system pressure for the Zr-Si-C-O system was varied between 10^{-4} atm and 10 atm, the temperature was varied between 1400 K and 2800 K, and the stoichiometry was fixed at Zr:Si:O:C = 1:1:2:1 (which corresponds to the stoichiometry of Eq. (25)).

Table 4. Thermodynamic Data for the Y-Si-C-O System at 2400 K.

SPECIES	$\Delta H^o_f(298.15\ K)$ (kcal mol^{-1})	$-\Delta[G^o(T) - H^o(298.15\ K]/T$ (cal K^{-1} mol^{-1})
C(g)	170.890	37.493
$C_2(g)$	200.200	45.965
$C_3(g)$	196.000	49.965
$C_4(g)$	232.000	49.010
$C_5(g)$	234.000	51.181
CO(g)	-26.420	20.778
$CO_2(g)$	-94.054	0.280
$C_2O(g)$	68.500	28.975

Table 4. (continued)

$C_3O_2(g)$	-22.380	13.787
O(g)	59.559	15.368
$O_2(g)$	00.000	00.000
$O_3(g)$	34.200	-16.224
Si(g)	107.700	32.632
$Si_2(g)$	141.000	39.099
$Si_3(g)$	152.000	40.293
SiO(g)	-24.000	17.360
$SiO_2(g)$	-73.000	-1.966
SiC(g)	172.000	43.159
$SiC_2(g)$	147.000	45.820
$Si_2C(g)$	128.000	40.128
Y(g)	101.500	29.820
$YC_2(g)$	141.000	42.842
YO(g)	-11.000	16.902
$Y_2O(g)$	1.000	15.523
$Y_2O_2(g)$	-127.400	-3.295
Si(1)	11.585	4.827
$SiO_2(1)$	-215.740	-42.583
YC(1)	-19.9	-4.201
$YC_{1.067}(1)$	-20.9	-3.682
$YC_{1\ 2}(1)$	-23.4	-3.478
$YC_{1.333}(1)$	-28.9	-4.154
$Y_2C(1)$	-19.0	-6.486
$Y_3C(1)$	-21.2	-7.611
$YSi_{0\ 6}(1)$	-27.6	-4.523
$YSi_{0\ 8}(1)$	-23.6	-5.235
YSi(1)	-30.0	-5.928
$YSi_{1.667}(1)$	-38.3	-7.952
$YSi_2(1)$	-40.5	-9.431
$Y_2Si(1)$	-34.7	-8.073
Y(1)	2.732	-1.138
SiC(alpha)	-17.100	-3.964
SiC(beta	-17.500	-3.925

Table 4. (continued)

$YC_2(s)$	-46.000	-7.074
$Y_2O_3(s)$	-455.400	-68.723
C(s)	0.0	0.0

Table 5. Thermodynamic Data for the Zr-Si-C-O System at 2000 K.

SPECIES	ΔH^o_f(298.15 K) (kcal mol^{-1})	$-\Delta[G^o(T) - H^o(298.15\ K)]/T$ (cal K^{-1} mol^{-1})
C(g)	170.890	37.505
$C_2(g)$	200.200	46.330
$C_3(g)$	196.000	50.485
$C_4(g)$	232.000	49.315
$C_5(g)$	234.000	51.488
CO(g)	-26.420	20.968
$CO_2(g)$	-94.054	0.348
$C_2O(g)$	68.500	29.054
$C_3O_2(g)$	-22.380	13.822
O(g)	59.559	15.238
$O_2(g)$	00.000	00.000
Si(g)	107.700	33.817
$Si_2(g)$	141.000	41.493
$Si_3(g)$	152.000	43.951
SiC(g)	172.000	44.404
$SiC_2(g)$	147.000	47.230
$Si_2C(g)$	128.000	42.700
SiO(g)	-24.000	18.671
$SiO_2(g)$	-73.000	-0.830
Zr(g)	148.300	33.128
ZrO(g)	14.000	18.057
$ZrO_2(g)$	-68.400	4.555
Si(1)	11.585	5.792
$SiO_2(1)$	-215.740	-42.031
Zr(1)	6.351	3.028

Table 5. (continued)

C(s)	00.000	00.000
SiC(alpha)	-17.100	-2.992
SiC(beta)	-17.500	-2.951
Zr(beta)	1.706	0.852
ZrC(s)	-47.000	-2.333
ZrO_2(s)	-261.000	-44.423
ZrSi(s)	-37.000	-2.126
Zr_2Si(s)	-49.800	-2.056
Zr_5Si_3(s)	-137.600	-5.443
$ZrSiO_4$(s)	-483.700	-90.160
$ZrSi_2$(s)	-38.100	-4.319

Discussion of results

The Y-Si-C-O System

Calculations were performed at 10^{-4} atm, 10^{-3} atm, 10^{-2} atm, and 1 atm and in 2 atm increments between 2 and 10 atm. The system temperature was varied in 200 K increments between 2000 K and 3200 K. Only the chemical elements and binary compounds were considered in the calculations due to a paucity of phase diagram and thermodynamic information on complex multicomponent phases.

Figure 36 shows the calculated condensed phase stability diagram for the Y-Si-C-O system. Figures 37 and 38 show the computed equilibrium vapor composition for this system as a function of temperature and at system pressures of 1 atm and 10 atm respectively. Figures 39 and 40 show the calculated condensed phase product yield as a function of temperature for P = 1 atm and 10 atm respectively.

Figures 37 and 38 show that at low system pressures and high temperatures, reaction products are calculated to be entirely vapor species. The major vapor species are shown to be CO(g), SiO(g), Y(g), and Si(g).

It should be noted from Figure 36 that at the calculated adiabatic temperature for reaction (1), T_{ad} = 3150 K, the only condensed phase material shown to be thermodynamically stable is $YSi_{0.6}$. Significant amounts of Y_2O_3 + SiC are predicted not to form above 2400 K. Thus reaction (24) will not occur at T_{ad} = 3150 K, but rather the following endothermic process is predicted to take palace

$$4Y(c) + 3SiO_2(c) + 3C(c) = 0.1YSi_{0.6}(c) + 3CO(g) + 2.4SiO(g) + 3.3Y(g) + 0.6YO(g). \quad (26)$$

From Figure 39, reaction (24) is seen to be the predominant reaction at about 2200 K for P = 1 atm. For P = 10 atm, reaction (24) is the predominant reaction between 2200 K and 2600 K (Figure 40).

It appears from the microprobe studies that the reaction occurring in our combustion synthesis is that associated with the formation of the four phases $YSi_{1.667}$, YC_2, SiC, and Y_2O_3 between approximately 2200 K and 2400 K. Since these individual phases were not observed, however, ternary and quaternary alloy formation among the four components probably occurs. The condensed phase stability diagram may not be entirely correct since these complex phases have not been taken into account in the calculations. Virtually nothing is known about the phase equilibria associated with the quaternary Y-Si-C-O system or the various ternary systems of which it is comprised.

Results of the present calculations suggest that it may be difficult to produce the appropriate Y_2O_3 + SiC composite mixture by combustion synthesis. It might be advisable, however, to try to maintain a reaction temperature in the range of 2000 K to 2400 K (P = 1 atm) by adding an inert oxide material to the reacting mixture. This addition may also stabilize the Y_2O_3 + SiC product in a manner similar to that occurring during hot pressing.

The present calculations also suggest that the combustion synthesis reaction should not be carried out under vacuum because of excessive volatilization. There may also be no inherent chemistry advantage in performing the combustion reaction under pressure. High pressure synthesis may, however, increase product yields somewhat in the $YSi_{1.667}$ + YC_2 + SiC + Y_2O_3 four phase region.

The Zr-Si-C-O System

The calculated condensed phase stability diagram for the Zr-Si-C-O system is presented in Figure 41 for temperatures between 1400 K and 3000 K and for a stoichiometry corresponding to reaction (25). Figures 42 and 43 show the condensed phase product yield as a function of temperature for system pressures of 1 atm and 10 atm respectively.

Figure 41 shows several regions where three and four phases are calculated to coexist. Regions where oxides, carbides, and silicides coexist may imply the formation of multicomponent phases such as $ZrO_2 \cdot SiO_2$, $ZrC \cdot ZrO_2$, $ZrO_2 \cdot Zr_2Si$, etc.

Figure 41 shows that there is a region composed of entirely vapor species. This region is found at system pressures below 10^{-3} atm and temperatures greater than 2600 K.

Beta silicon carbide forms in only two regions of the stability diagram shown in Figure 41, and those regions are at relatively low temperatures. The other regions of the stability diagram

are dominated by formation of the stable SiO(g) vapor species and by the formation of ZrC, zirconium silicides, and ZrO_2. As noted above, SiC and ZrO_2 coexist in two separate regions of the stability diagram. In both regions, some condensed phase impurities are also present. However, between 1200 K and 1500 K and over the pressure range of 10^{-4} atm to 10 atm, a relatively pure SiC + ZrO_2 region exists. The amount of ZrC impurity is minimal at 1200 K, ranging from 10^{-3} moles at 10^{-4} atm pressure to 10^{-8} moles at 10 atm pressure. At the temperature increases, formation of SiC(s) and ZrO_2(s) completes with formation of the vapor species CO(g) and SiO(g). For a pressure of 10^{-4} atm and a temperature of 1400 K, the amount of ZrC impurity is 0.273 moles while 0.134 moles of CO(g) and 0.409 moles of SiO(g) are formed. At 1 atm and 1400 K, SiC and ZrO_2 form quantitatively, with only 10^{-5} moles of ZrC impurity presnet. The amount of CO(g) and SiO(g) in the vapor also drops to 10^{-5} moles at this temperature and pressure.

There is also a region where ZrO_2(s) and SiC(g) coexist at approximately 1600 K to 1900 K. At lower pressures, the vapor species CO(g) and SiO(g) are present in significant amounts, with 0.33 moles of CO(g) and 1.0 moles of SiO(g) forming at 10^{-4} atm and 1600 K. The impurity ZrC is also calculated to be stable at these temperatures and pressures and is present at levels of 65 wt%. As the system pressure increases, the equilibrium amounts of ZrC, CO(g), and SiO(g) drop dramatically to 0.09 wt% ZrC, 8×10^{-4} moles of CO(g), and 2.5×10^{-3} moles of SiO(g). At the other end of this region, ZrO_2 and SiC form stoichiometrically as shown in the yield diagrams of Figures 42 and 43.

The results of these calculations suggest that the optimal combustion temperature for synthesis of a ZrO_2 + SiC composite material may be lower than the calculated adiabatic temperature. The calculations also suggest that performing the synthesis at pressures greater than 1 atm may not be advantageous other than to provide densifiction.

F. Ti + C Potential Energy Surfaces

For completeness, a brief account of our effort to devise a potential energy surface (PES) for the Ti + C system is given here. The effort was not successful in producing a PES for each individual component which was stable, in a crystallographic sense, in the proper temperature range for any reasonable length of time. The high degree of anisotropy in graphite makes pairwise interactions totally inadequate even at 1000 K for 10 ps. One should note that "reasonable" phonon spectra are produced using pairwise harmonic interactions in the basal plane, but different radial force constants are required at each neighbor distance involved [35]. Also, better numerical results require a bending force constant to be added. In any case, harmonic approximations are not adequate for our purposes because of the very poor description of bond breaking given by such models.

We also attempted to model the dynamic behavior of molten Ti. It was found that the usual Lennard-Jones 6-12 potential fit to the heat of formation and the bcc lattice constant gives a melting point which is about a factor of three too high (6500 K rather than 1933 K). As a remedy, a more general form of the pair potential was fit to the isothermal compressiblity in addition to the other properties. The isothermal compressibility gives the products of the exponents, n and m, in the functional form,

$$v(r) = \varepsilon/ (m-n) (n(r_0/r)^m - m(r_0/r)^n). \qquad (27)$$

Given the values of the lattice constant, 3.2708 Angstroms [36], the heat of formation, 112.4 kcal/mol [27], one obtains values of 2811.5 K, 3.2703 Angstroms, and 42.4 for ε, r_0, and nm, respectively, at 0 K. The individual values of n and m are taken at 4 and 10, respectively, as a matter of convenience. The resulting mean square displacements as functions of time and a pair distribution function generated by molecular dynamics simulations are shown in Figures 44 and 45 for 2000 K.

The molecular dynamics calculations consist of 96 trajectories, each consisting of 2000 time steps of 100 au duration. A fourth order, Runge-Kutta-Gill integrator is used to propagate the system [38]. The initial conditions are selected by means of the "smart" Monte Carlo method of Rossky, Doll, and Friedman [39]. The "smart" Monte Carlo trajectories for the initial consitions are each composed of 100 time steps of 100 au each. The radial distribution functions are derived from the configuration of the system recorded every 100th time step in each trajectory. A subaverage over blocks of 16 trajectories provides an estimate of the statistical variance in the calculations. Prior to selecting the initial conditions, a perfect crystal is established and annealed numerically using ten, 100 step "smart" Monte Carlo trajectories with time steps varying from 10 to 100 au. Subsequently, simulations at 1800 K and 1700 K failed to maintain solid-like pair distribution functions after having begun in a perfect crystalline state. (The criterion is that the ratio of the first peak height to the first minimum beyond that peak is greater than 0.2. This is an empirical standard generally accepted within the statistical mechanics community [40].)

III. CONCLUSION

The main results of the project are the following. The static contact angle for molten Ti on Poco graphite is $3.5^\circ \pm 0.5^\circ$ at the melting point of Ti. The dynamic contact angle oscillates with front velocity in the experimental configurations examined here due to the presence of the melt front during the spreading process. Remnants of the original cylindrical geometry of the metal pellet persist for most of a trial. As a pellet becomes completely melted, mechanical constraints are relaxed which cause undulations in the contact angle-velocity relation, a variant from earlier observations made in the wetting literature [15, 16, 18-23]. In spite of the macroscopic dimensions of the experiments, the qualitative features of this progression are expected to hold in the microscopic setting of a combustion synthesis reaction.

As for microgravity effects, the numerical simulations show two particularly important features. One is that wetting process of molten metal on an unmelted component entails a complete rearrangement of the fluid from its initial solid configuration. Consequently, much of the void region changes location during the combustion process. This gives rise to the second feature which is that gravity can act to collapse some void regions while expanding others leading to a change of pore distribution sizes in a microgravity environment. In particular, the numerical simulations would predict a finer pore structure in a microgravity environment. In the burn-up, burn-down experiments, particularly in the Ni + Al system, one may find a coarser pore structure in the burn-up specimens where the combination of the reaction front and gravity act as a partial "zone-refinement" mechanism. Janet Hurst of NASA-LeRC is in the process of investigating this possibility.

In the study of gravitational effects on the combustion rate, a unified framework for understanding the masking of the expected gravitational effect is presented by modeling the diffusive and convective contributions to the reaction rate explicitly. The convective contribution is further split into spreading and gravitational contributions. The spreading rates (100 cm/s for 20 μm diameter particles, 10° contact angle) calculated from numerical simulations of wetting process give the correct order of magnitude for the gravitational. effect [11]. The present model has the added virture that particle irregularity [13] and magnetic field effects experiments [41] may also be understood within the same framework.

The numerical simulations show other important features as well. Namely, the solid metal completely rearranges configuration once melted. The characteristic time for the rearrangement is comparable to the capillary rise time predicted in other models [9, 10]. However, since the rearrangement process involves a much larger fraction of the system, it is expected to control the reaction rate more strongly than the capillary action. In terms of reaction models, the point of the simulations is that the proper characteristic reaction length should be metal component size rather than the nonmetal (carbon) component size [9, 10]. The effects of nonmetal size may be understood in terms of surface area of reactivity, which is also discussed.

In the thermochemical modeling of ceramic composites, calculations suggest that combustion synthesis of Y_2O_3 + SiC composite may be difficult, although some control is possible by restricting the reaction temperature to the 200-2400 K range with inert additives. A similar conclusion holds for the $Zr\ O_2$ + SiC composite where it is also found that pressurizing the system has no synthetic advantage.

In the molecular dynamics studies of the Ti + C system, an adequate potential energy surface could not be devised. A substantially different approach is required for such a study.

REFERENCES

[1] A. G. Merzhanov, "Problems of Technological Combustion", *Protessy Goreiia v. Khim. Technol. i Metall., Chemical Physics,* Inst. Akad. Nauk, Chernogolovka, 1975, pp. 5-28.

[2] A. G. Merzhanov, "Problems of Combustion in Chemical Technology and Metallurgy", *Russ. Chem. Rev.* **45** (5), 827-848 (1976).

[3] A. G. Merzhanov, *Russ. Chem. Rev.* **45**, 409-420 (1976).

[4] K. T. Faber and A. G. Evans, "Intergranular Crack-Deflection Toughening in Silicon Carbide", *Comm. Amer. Ceramic. Soc.* p. C-94, June 1983.

[5] L. E. Scriven, "Liquid Materials and Flow Processes in Reduced Gravity," in *Materials Processing in the Reduced Gravity Environment of Space,* G. E. Rindone, ed., (North-Holland, New York, 1982).

[6] R. B. Bird, W. E. Stewart and E. N. Lightfoot, *Transport Phenomena* (Wiley and Sons, New York, 1960).

[7] S. Ostrach, "Convection Phenomena of Importance for Material Processing in Space," in *Progress in Astronautics and Aeronautics* **52**, L. Steg, ed., (American Institute of Aeronautics and Astronautics, New York, 1977.)

[8] A. P. Aldushin, T. M. Martem'yanova, A. G. Merzhanov, B. I. Khaikan, and K. G. Shkadinskii, *Fiz. Goren. Vzr.* **8**(2), 202 (1972).

[9] E. V. Okolovich, A. G. Merzhanov, B. I. Khaikin, and K. G. Shkadinskii, *Fiz. Goren. Vzr.* **13**(3), 326 (1978).

[10] E. A. Nekrason, Yu. M. Maksimov, M. Kh. Ziatdinov, and A. S. Shteinberg, *Fiz. Goren. Vzr.* **14**(5), 26 (1978).

[11] A. I. Kirdyashkin, Yu. M. Maksimov, and E. A. Nekrasov, *Fiz. Goren. Vzr.* **22**(1), 23 (1986).

[12] S. M. Valone and R. G. Behrens, *Materials Processing in the Reduced Gravity Environment of Space,* Materials Researcch Society Symposia Proceedings, vol. 87, ed. R. H. Doremus and P. C. Nordine, (Publishers, Mars, PA, 1987), pp. 113-120.

[13] K. L. Epsishin and A. N. Pityulin, *Fiz. Goren. Vzr.* **22**(1), 29 (1985).

[14] L. Fredin, G. P. Hansen, J. L. Margrave, and R. G. Behrens, "Laser Ignition Studies," *Proceedings of the DARPA/Army Symposium on Self-Propagating, High-Temperature (SHS),* K. Gabriel, ed., 1986, (in press).

[15] E. B. Dussan V., Ann. Rev. *Fluid Mech.* **11,** 371 (1979).

[16] E. B. Dussan V. and S. H. Davis, *J. Fluid Mech.* **65**, 71 (1974);
L. M. Hocking, *J. Fluid Mech.* **76**, 801 (1976);
E. B. Dussan V., *AIChE J.* **23**, 131 (1977);
R. G. Cox, *J. Fluid Mech.* **168**, 169, 195 (1986).

[17] Poco graphite is a locally manufactured, high-density crystalline carbon material which also couples well to rf fields. The high density reduces the penetration of molten metal into the substrate.

[18] R. Hoffman, *J. Colloid Interface Sci.* **60**, 11 (1977).

[19] T. D. Blake and J. M. Haynes, *J. Colloid Interface Sce.* **30**, 421 (1969).

[20] G. Inverarity, *Br. Polym. J.* **1**, 245 (1969).

[21] A. M. Schwartz and S. B. Tejada, *J. Colloid Interface Sce.* **38**, 359 (1972).

[22] W. B. Hardy, *Philos.* mag. **38**, 49 (1919).

[23] W. D. Bascom, R. L. Cottington, C. R. Singleterry, *Contact Angle, Wettability, and Adhesion,* Adv. in Chem. No. 43, (American Chemical Society, Washington, D. C., 1964), pp. 355-79.

[24] J. Buckmaster, *J. Fluid Mech.* **81**, 735 (1977).

[25] B. D. Nichols, C. W. Hirt, and R. S. Hotchkiss, "SOLAVOF: A Solution Algorithm for Transient Fluid Flow with Multiple Free Boundaries, "University of California, Los Alamos National Laboratory Report, LA-8255, issued August, 1980.

[26] C. W. Hirt and B. D. Nichols, *J. Comp. Phys.* **39**, 201 (1981).

[27] A. P. Aldushin and B. I. Khaikin, *Fiz. Goren. Vzryva* **10**(3), 313 (1974); e. A. Nekrasov, V. K. Smolyakov, and Yu. M. Maksimov, *Fiz. Goren. Vzryva* **17**(5), 39 (1981);
V. K. Smolyakov, E. A. Nekrasov, and Yu. M. Maksimov, *Fiz. Goren. Vzryva* **18**(3), 59 (1982).

[28] S. M. Valone, "Reactive Transport at Ti-C Interfaces," *Proceedings of the DARPA/Army Symposium on Self-Propagating, High-Temperature Synthesis (SHS)*, K. Gabriel (Ed.), 1986, (in press).

[29] F. M. White, *Fluid Mechanics*, (McGraw-Hill, New York, 1979).

[30] M. M. Kasakow and D. N. Nekrasov, *Doklady Akademii Nauk SSSR* **119**, 107 (1058); V. G. Levich, *Physiochemical Hydrodynamics*, (Prentice-Hall, Englewood Cliffs, N. J., 1962), ch. VII.

[31] R. Hultgren, P. D. Desai, D. T. Hawkins, M. Gleiser, and K. K. Kelley, *Selected Values of the Thermodynamic Properties of Binary Alloys*, (American society for Metals, Metals park, OH, 1973).

[32] T. M. Besmann, "SOLGASMIX-PV, A Computer Program to Calculate Equilibrium Relationships in Complex Chemical Systems," Oak Ridge National Laboratory report ORNL/TM-5775 (April 1977).

[33] D. R. Stull and H. Prophet, *JANAF Thermochemical Tables*, 2nd ed., Nat. Stand. Ref. Data Ser., Nat. Bur. Stand. (U.S.), publication NSRDS-NBS-37 (June 1971).

[34] O. Kubaschewski and C. B. Alcock, *Metallurgical Thermochemistry*, 5th Ed., Pergamon Press, Oxford (1979).

[35] J. A. Young and J. U. Koppel, J. *Chem. Phys.* **42**, 357 (1965);
T. Nicklow, N. Wakabayashi, and H. G. Smith, *Phys. Rev.* **B5**, 4951 (1972);
K. K. Mani and R. Ramani, *Phys. Stat. Sol.* **B61**, 659 (1974);
H. A. Rafizadeh, *Physica* **74**, 135 (1974);
A. P. P. Nicholson and D. J. Bacon, *J. Phys.* **C10**, 2295 (1977).

[36] N. W. Ashcroft and N. D. Mermin, *Solid State Physics*, (Holt, Rhinehart, and Winston, New York, 1976). The value given is derived from this room temperature value and extrapolated to 0 K using a linear thermal expansion coefficient of 8.3×10^{-6}/K from Ref. 37.

[37] K. A. Gschneidner, *Solid State Physics*, **16**, 275 (1964).

[38] B. Carnahan, H. A. Luthers, and J. O. Wilkes, *Applied Numerical Methods*, (Wiley, New York, 1969), p. 363.

[39] P. J. Rossky, J. D. Doll, and H. L. Friedman, *J. Chem. Phys.* **69**, 4628 (1978).

[40] H. J. Raveche, R. D. Mountain, and W. B. Streett, *J. Chem, Phys.* **61**, 1970 (1974).

[41] A. I. Kirdyashkin, Yu. M. Maksimov, and A. G. Merzhanov, *Fiz. Goren. Vzr.* **22**(6), 65 (1986).

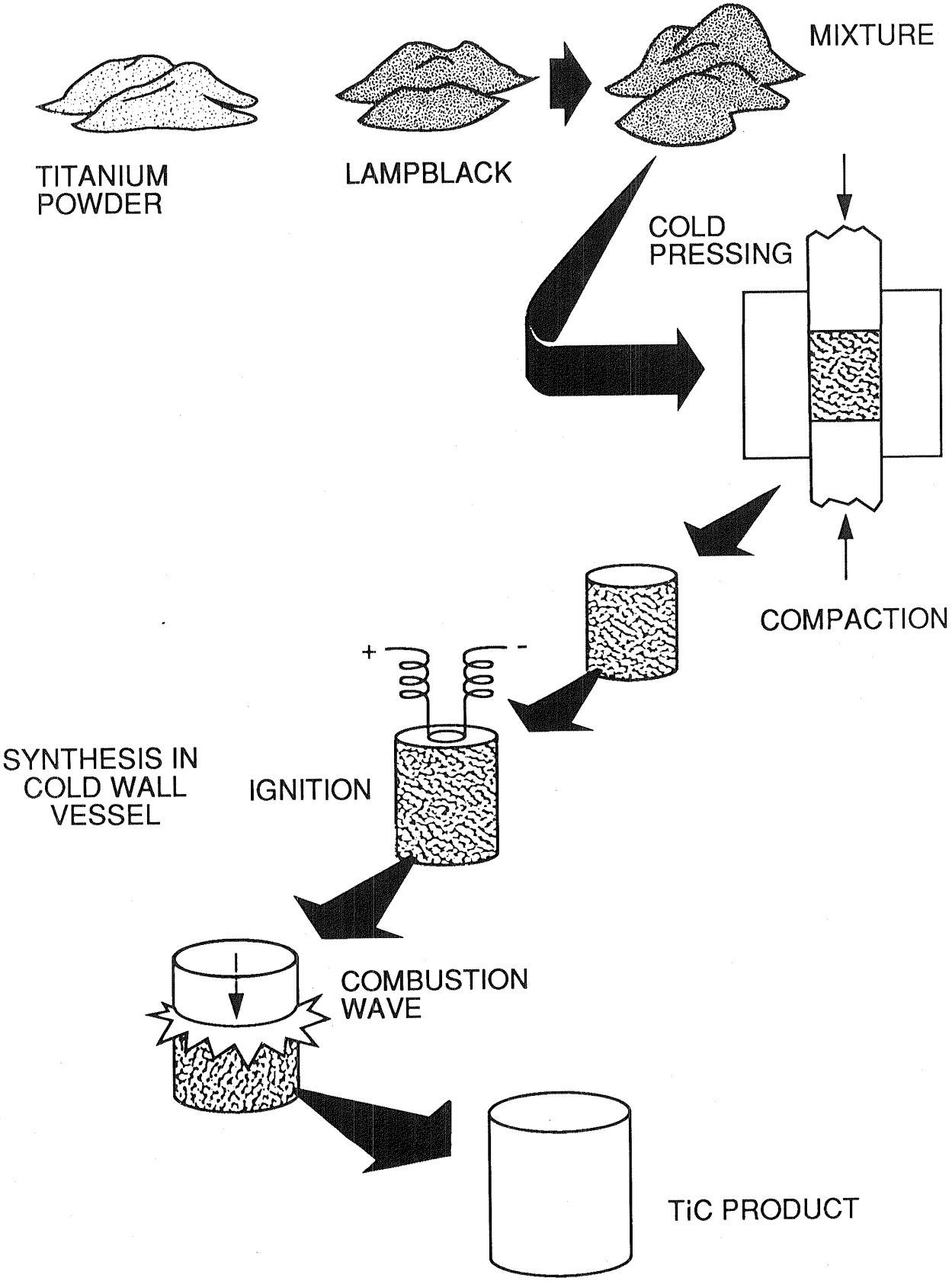

Figure 1. The Combustion Synthesis of Titanium Carbide

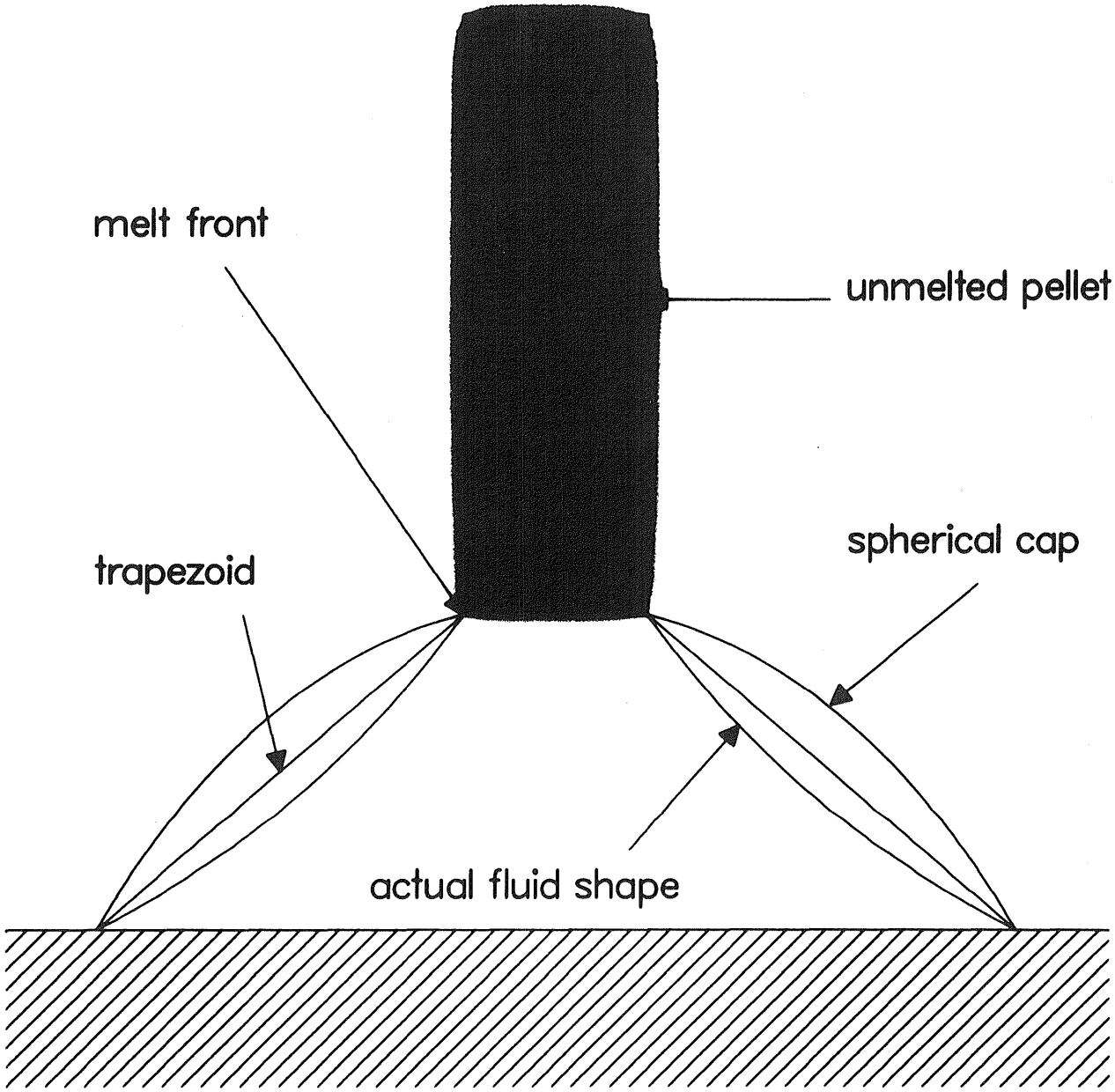

Figure 2. Schematic of a partially melted pellet and the spherical cap and trapezoidal approximations.

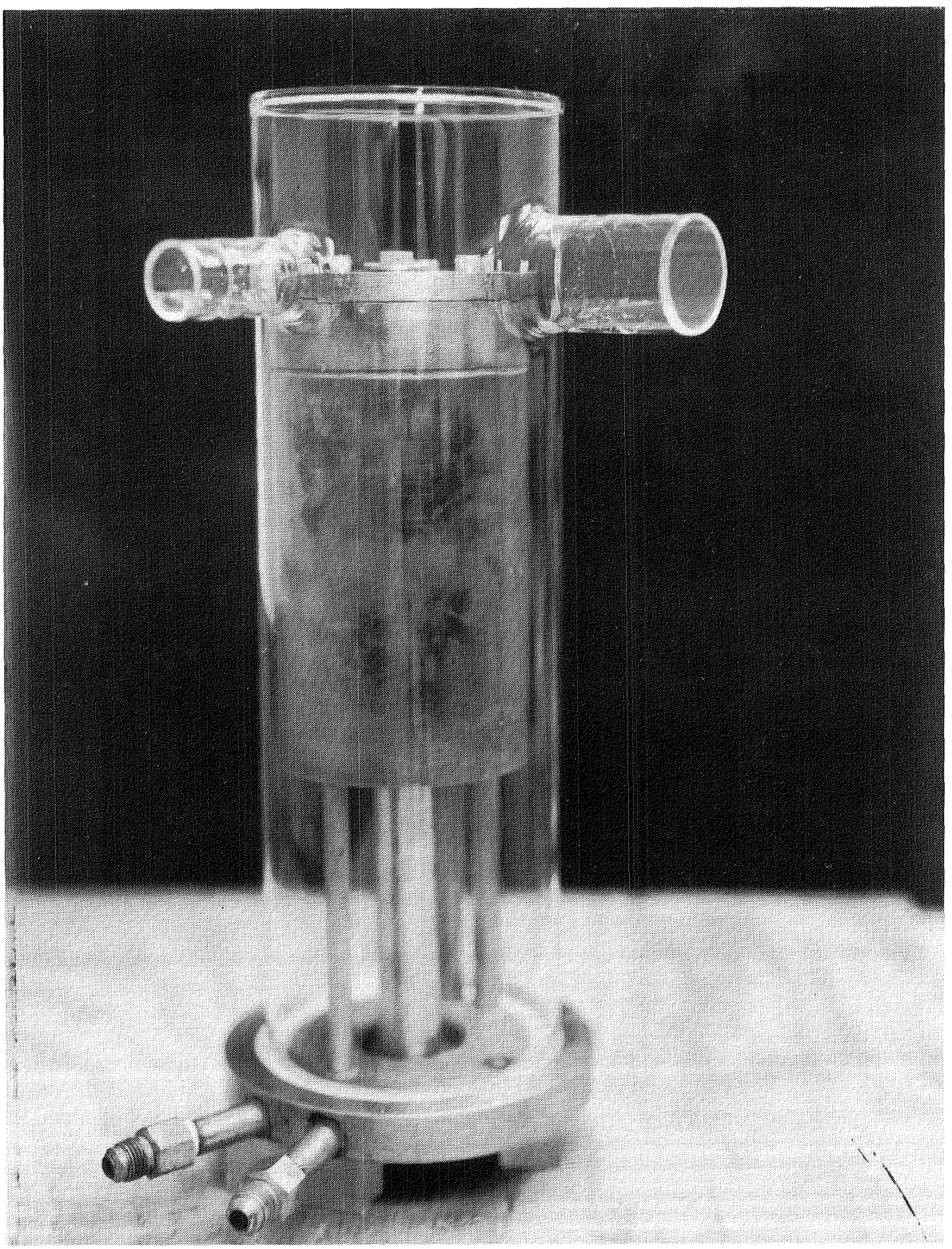

Figure 3. Mandrel for wetting experiments in rf generator.

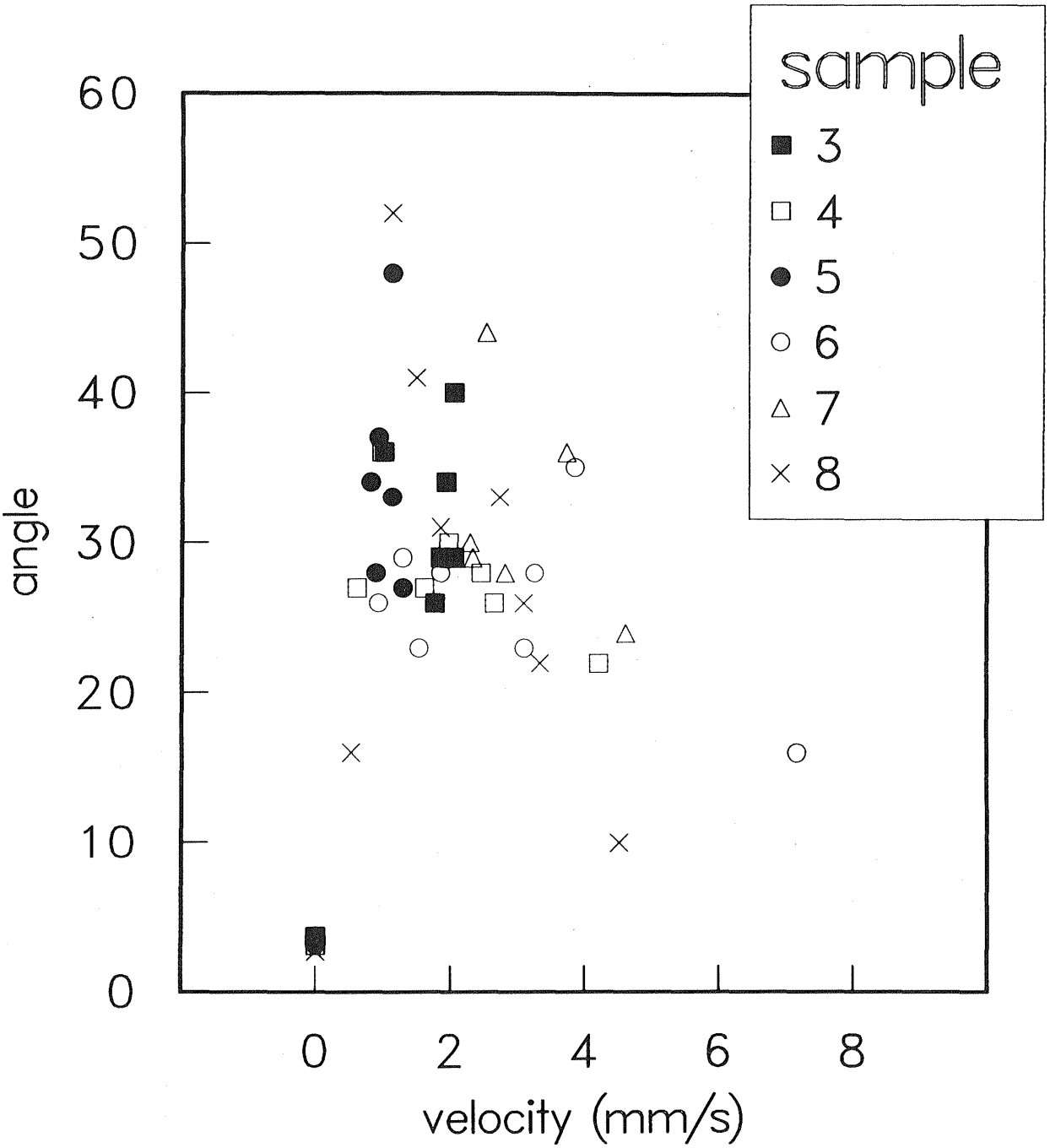

Figure 4. Contact angle velocity dependence for molten Ti on Poco graphite. Non-monotonic behavior apparent for most of each trial.

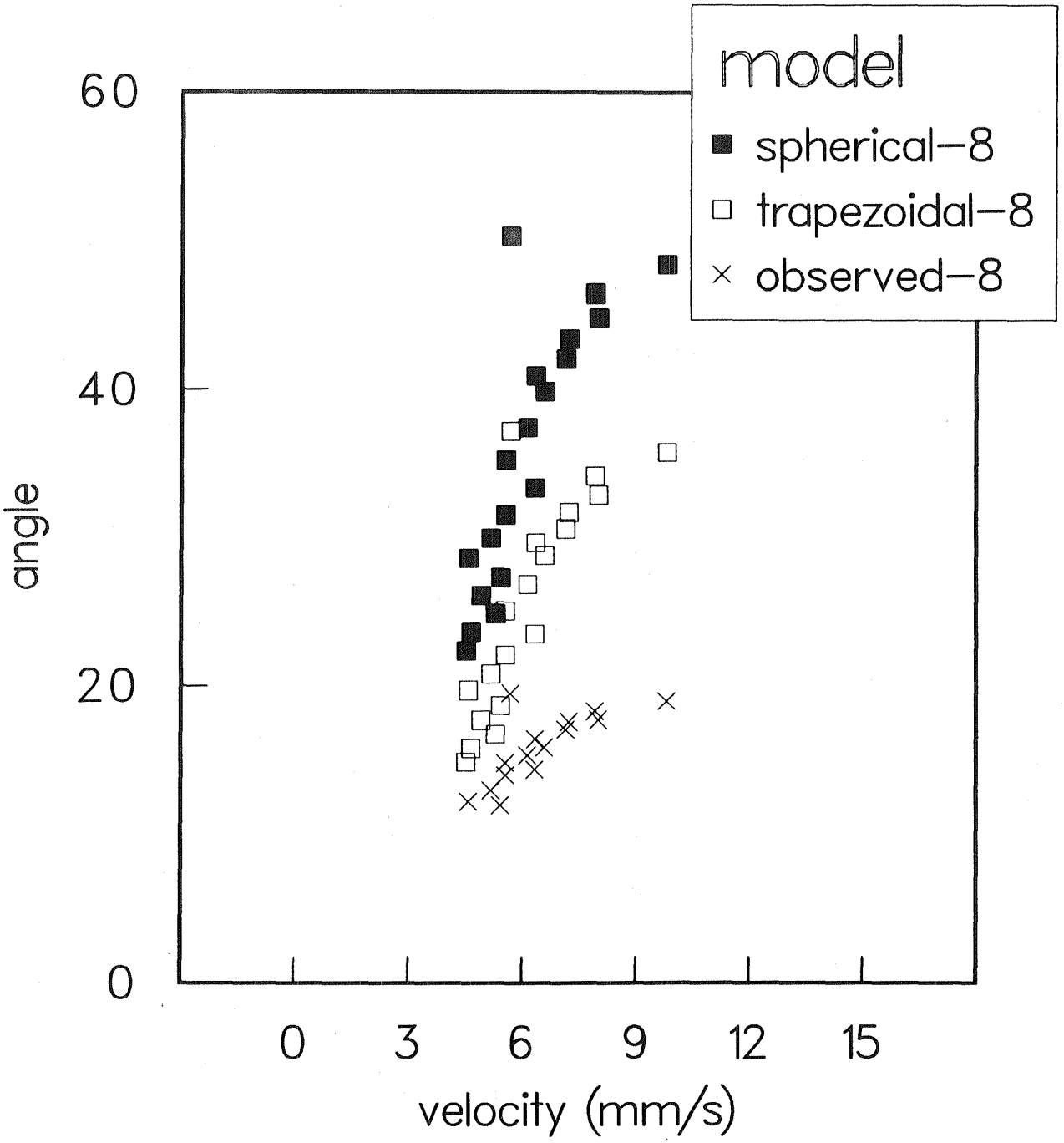

Figure 5. Contact angle velocity dependence for molten Ti on Poco graphite after melting (sample 3).

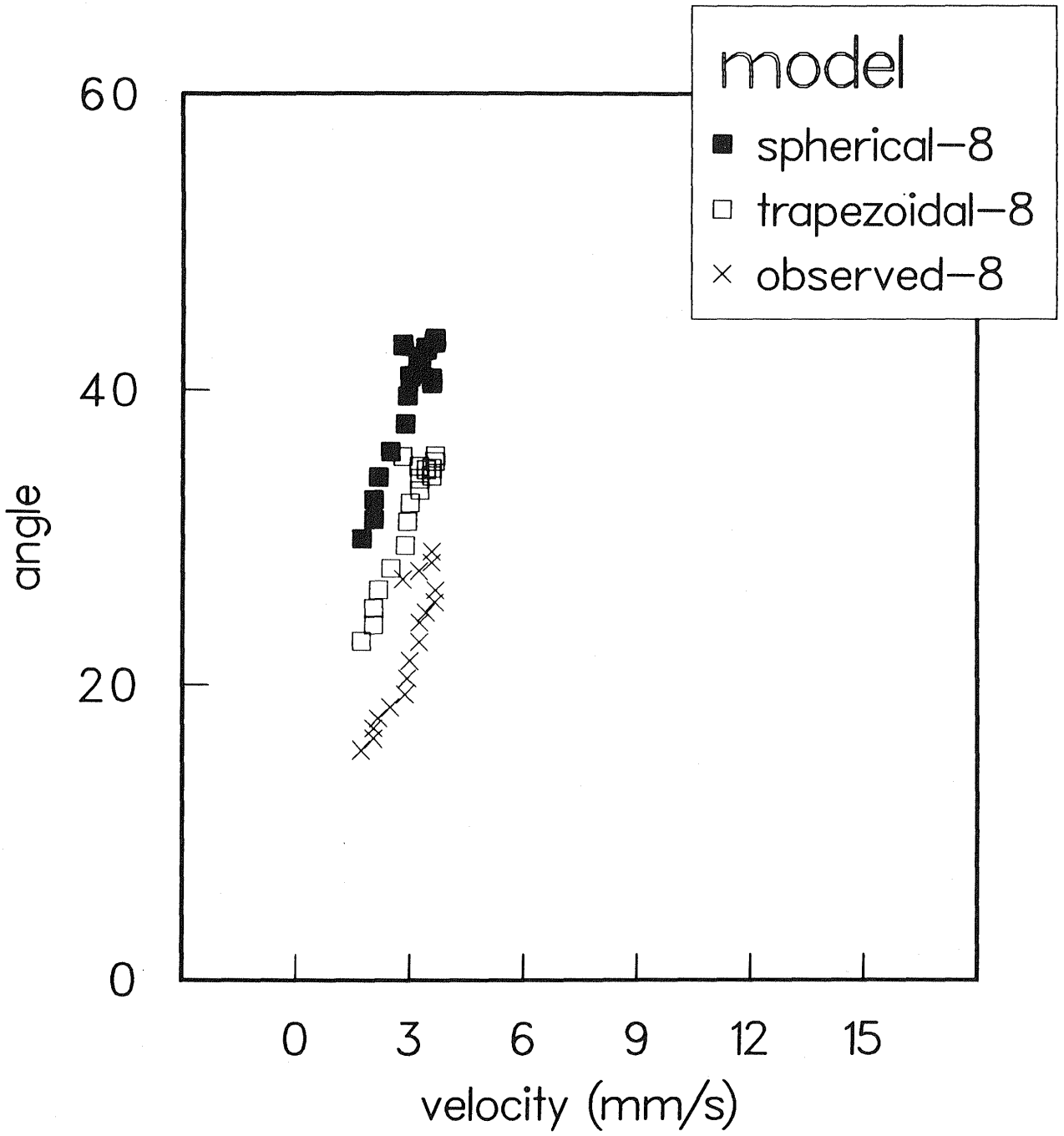

Figure 6. Contact angle velocity dependence (sample 4).

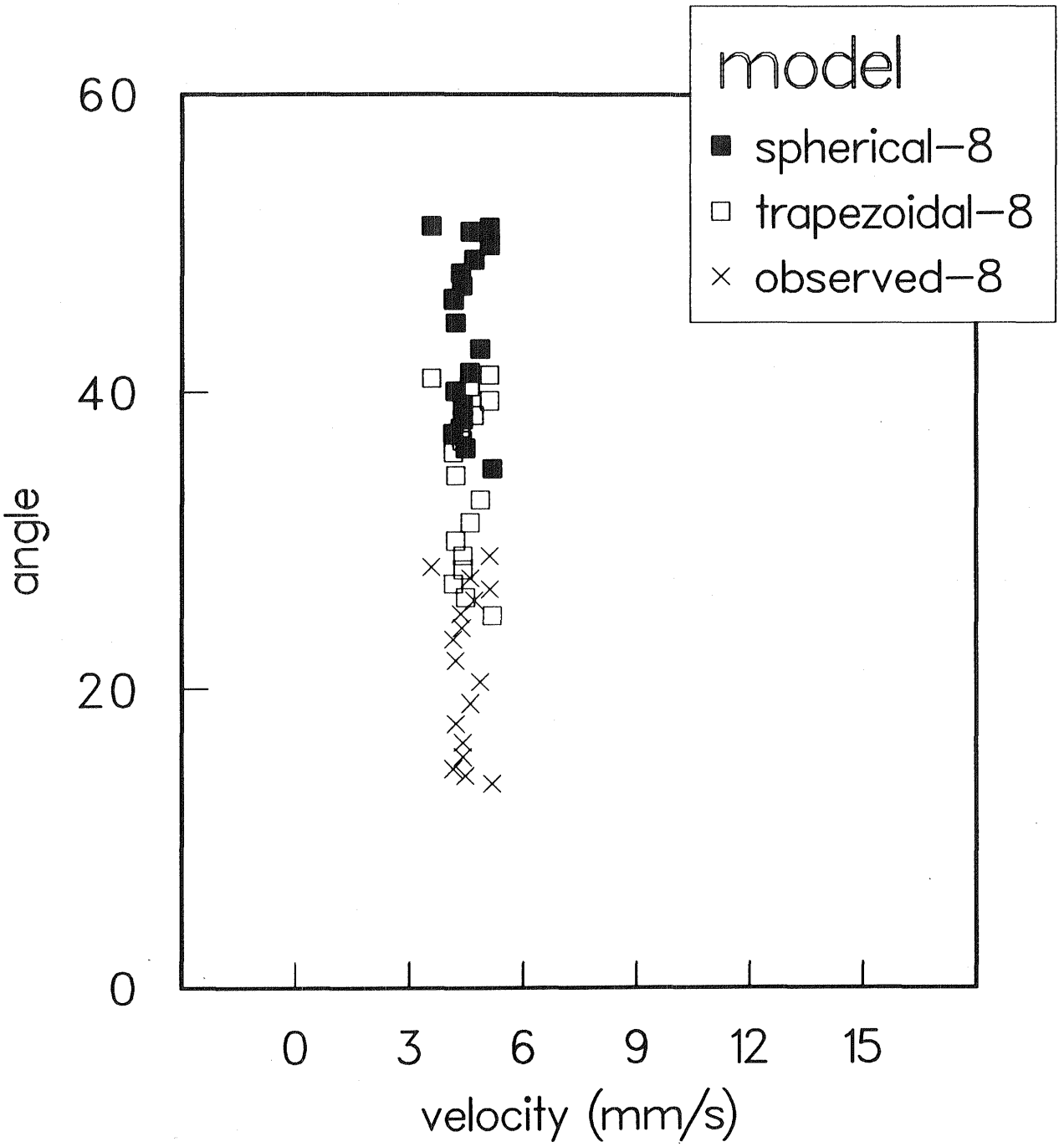

Figure 7. Contact angle velocity dependence (sample 6).

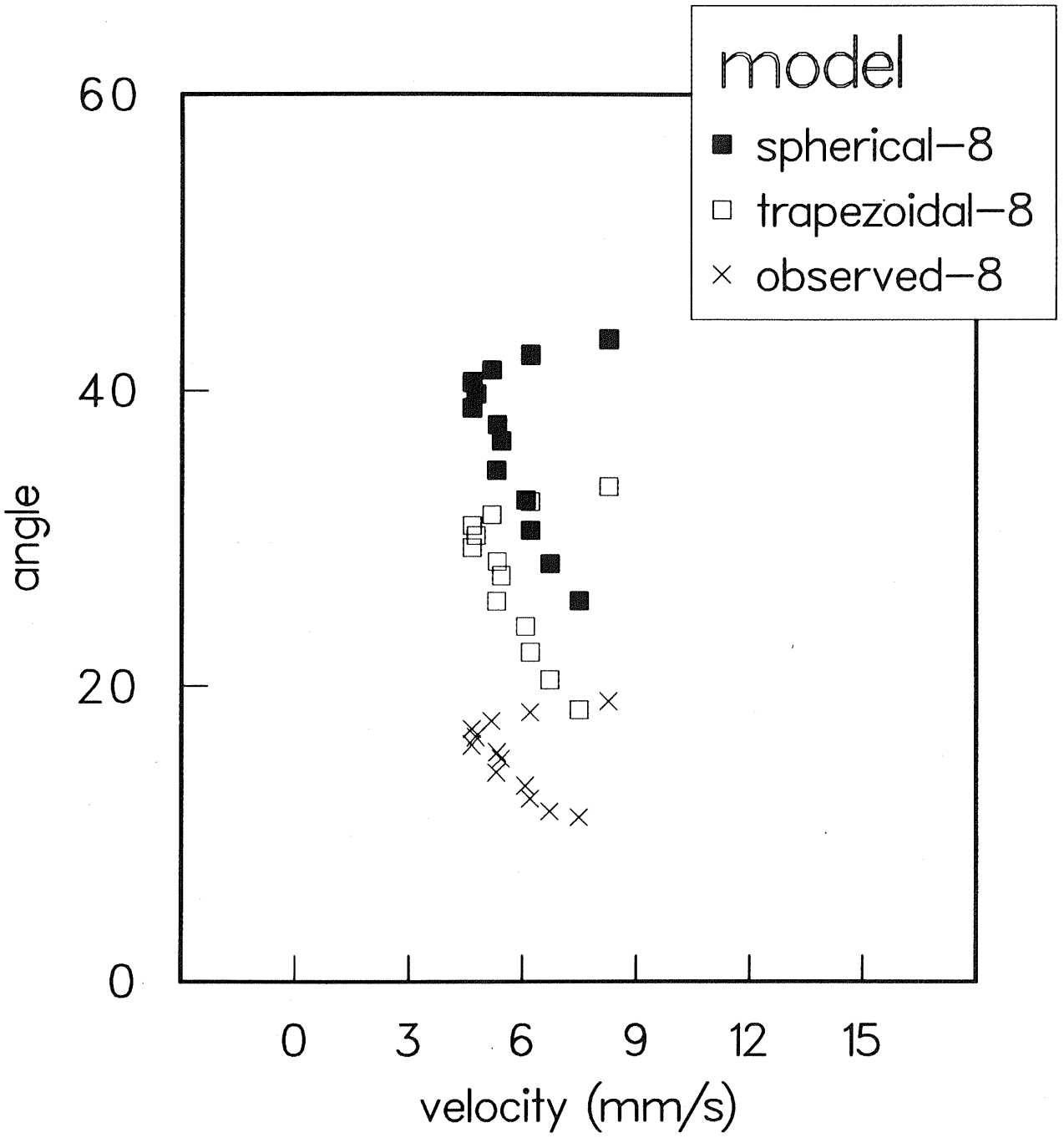

Figure 8. Contact angle velocity dependence (sample 7).

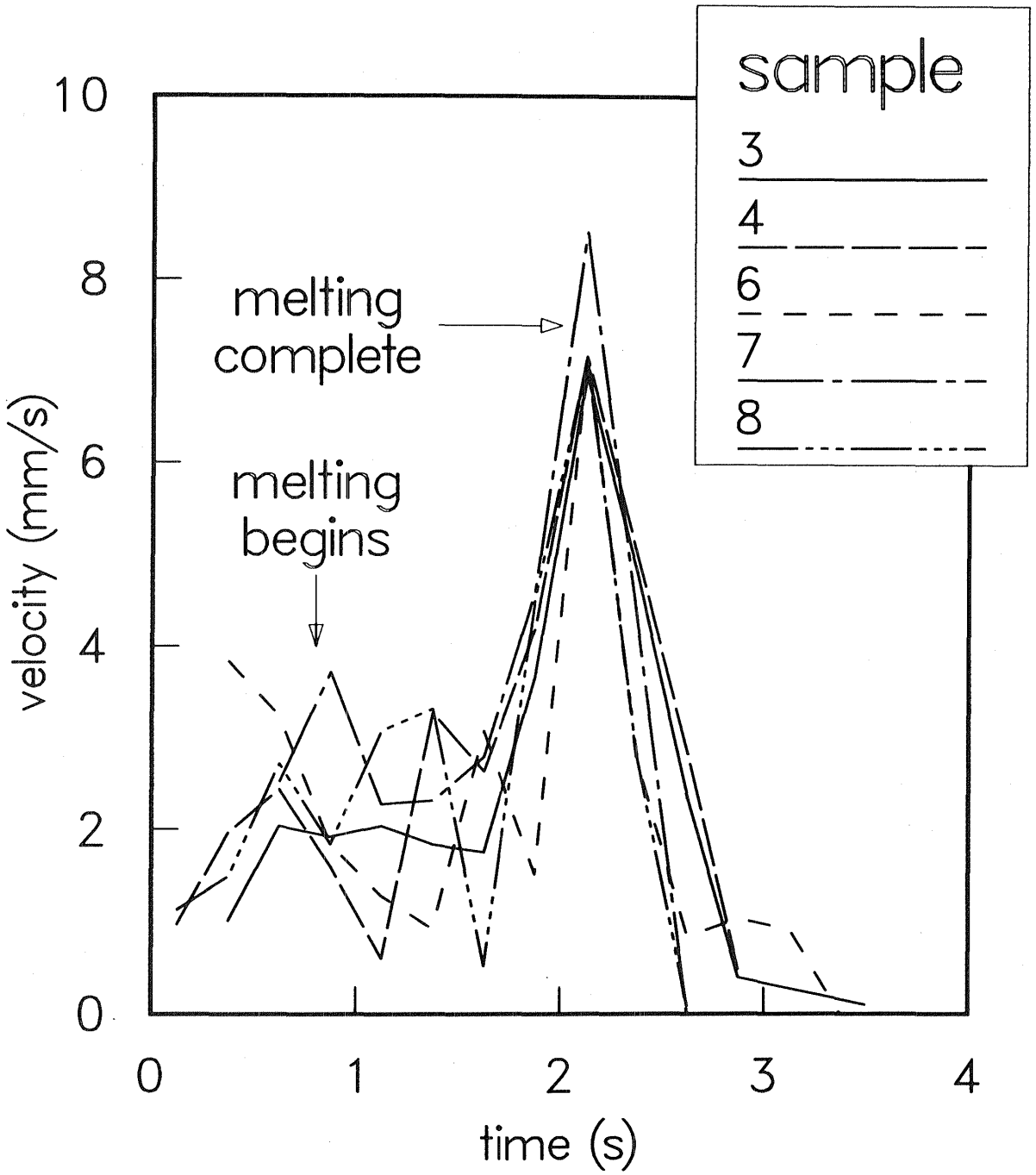

Figure 9. Front spreading velocities for molten Ti on Poco graphite. Spikes in the distribution relect relaxation of mechanical constraints. Time origin for each curve is shifted so that maxima coincide.

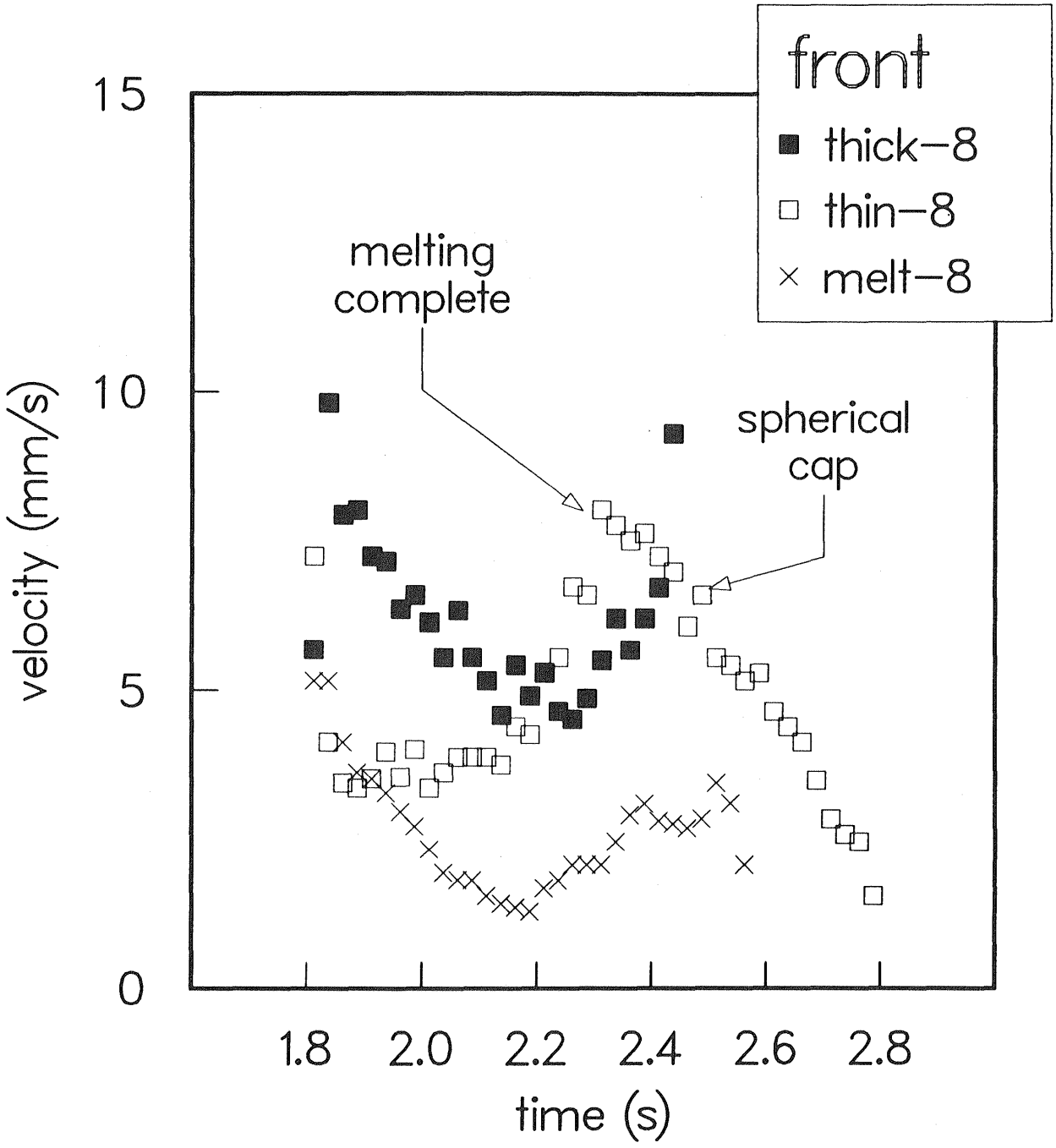

Figure 10. Front spreading velocities for molten Ti on Poco graphite after melting (sample 3). Major peaks labeled by constraint thought to be relaxing at the time. Time origin for each curve arbitrarily shifted to 1.8 s for comparison with Figure 9.

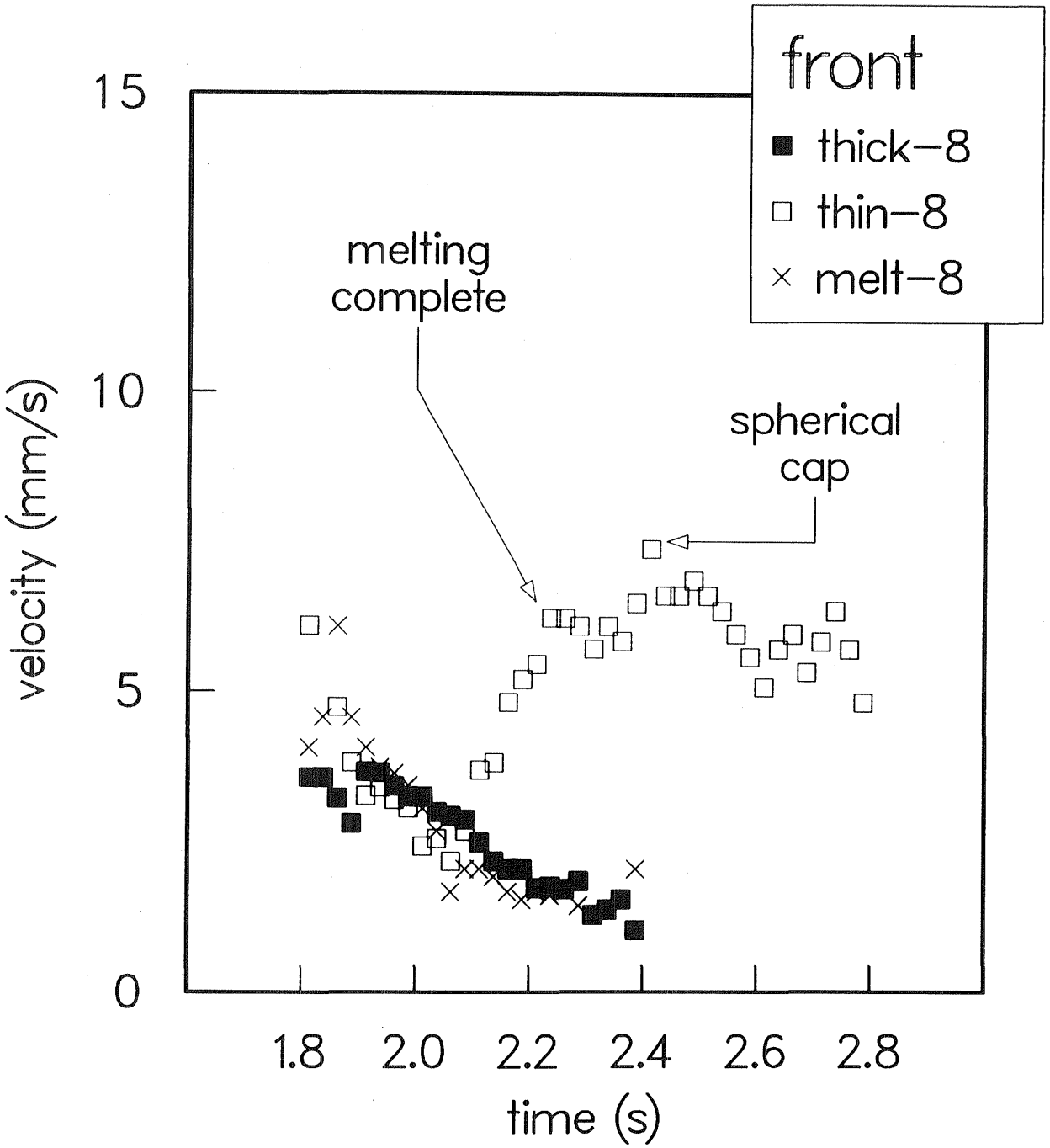

Figure 11. Front spreading velocities for sample 4. Time origin for each curve arbitrarily shifted to 1.8 s for comparison with Figure 9.

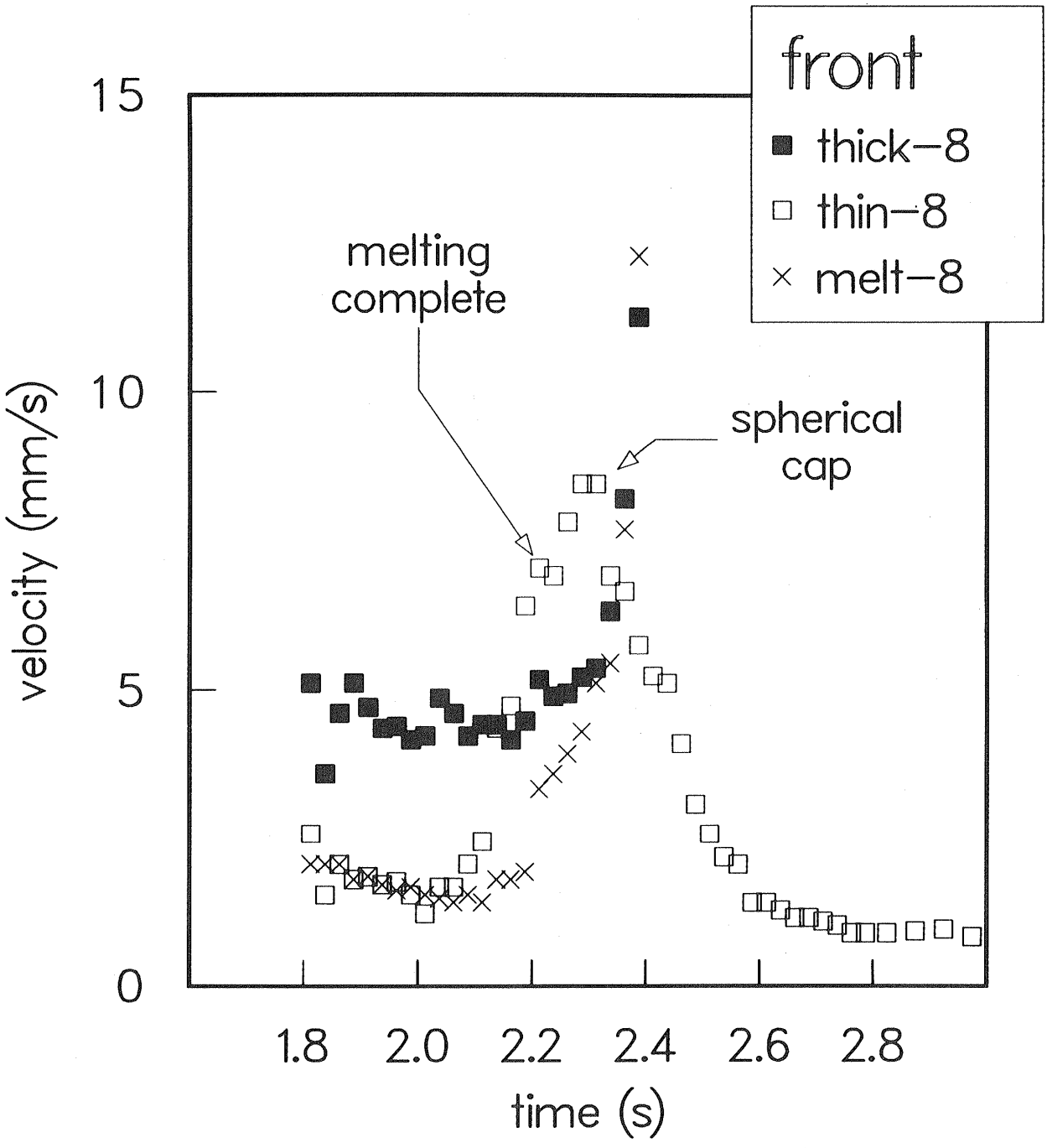

Figure 12. Front spreading velocities for sample 6. Time origin for each curve arbitrarily shifted to 1.8 s for comparison with Figure 9.

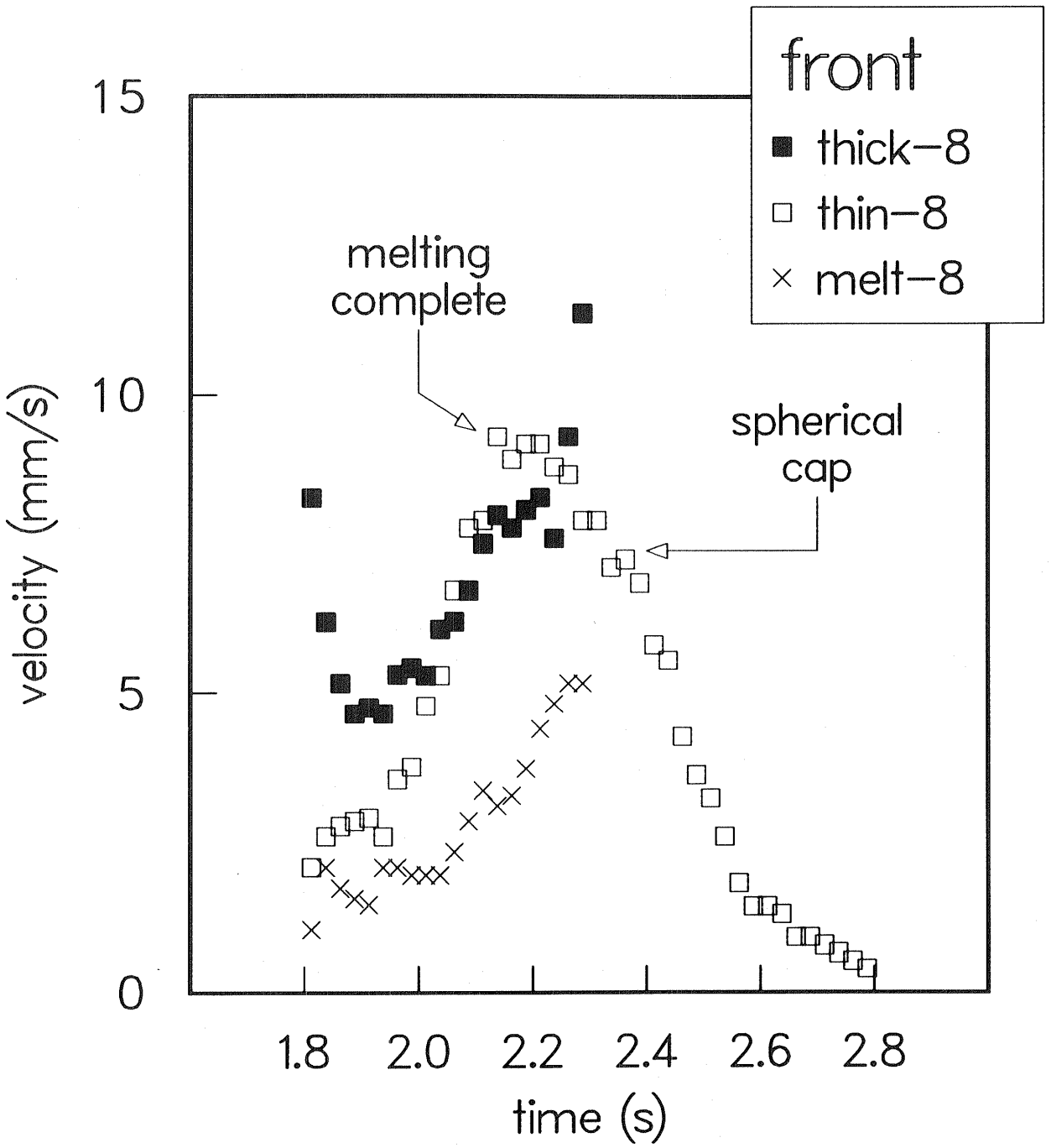

Figure 13. Front spreading velocities for sample 7. Time origin for each curve arbitrarily shifted to 1.8 s for comparison with Figure 9.

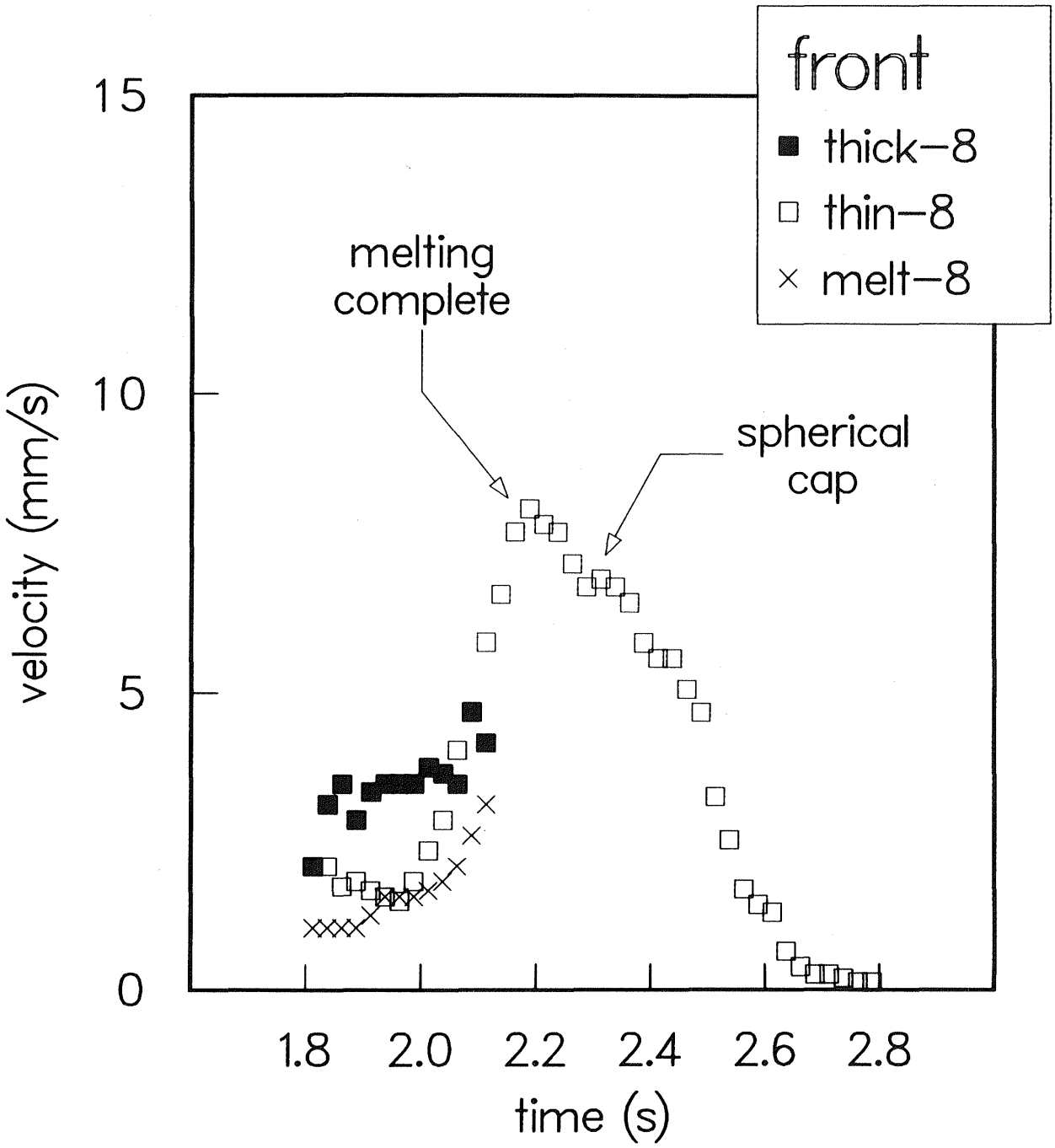

Figure 14. Front spreading velocities for sample 8. Time origin for each curve arbitrarily shifted to 1.8 s for comparison with Figure 9.

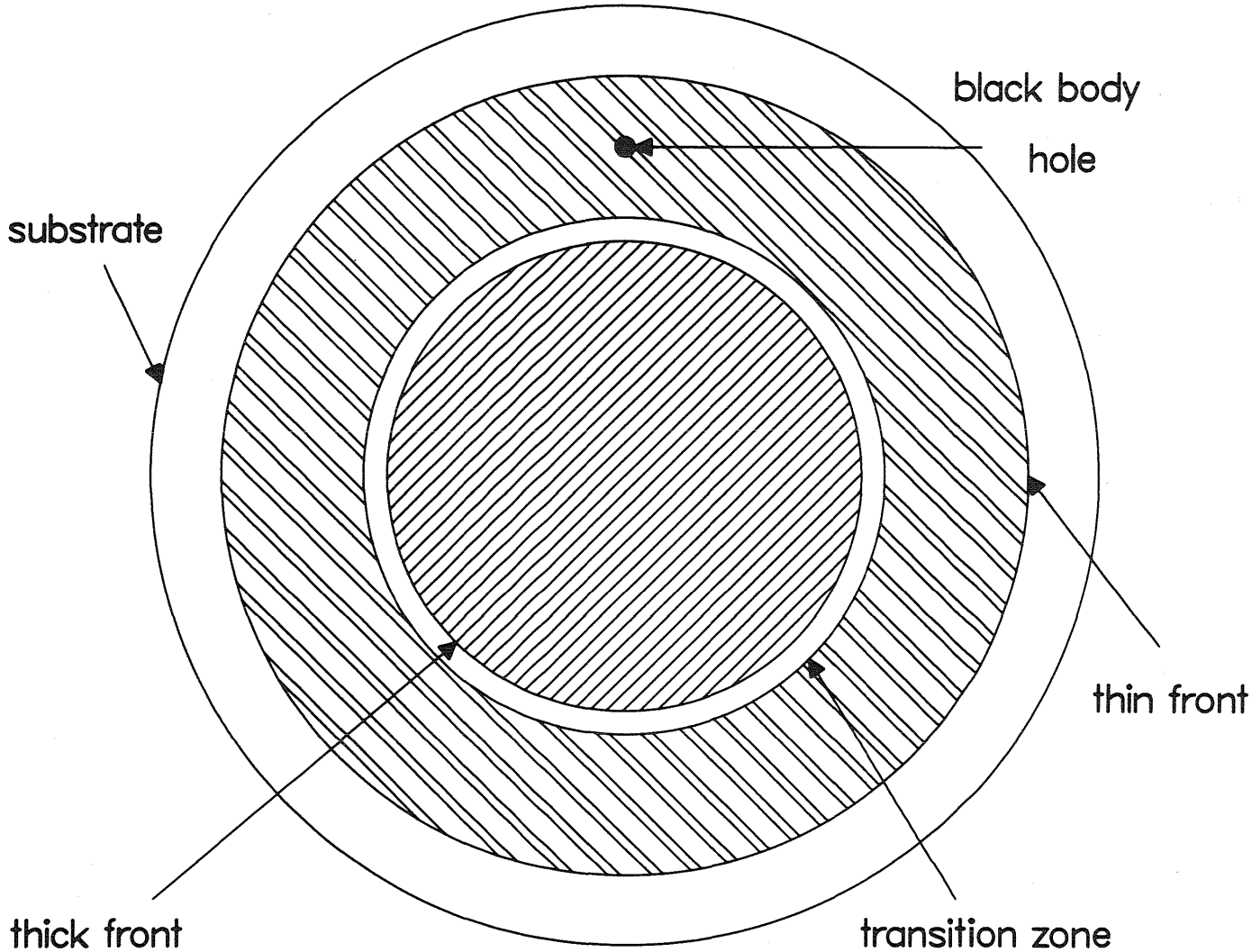

Figure 15. Schematic top view of final melt configuration in wetting experiment.

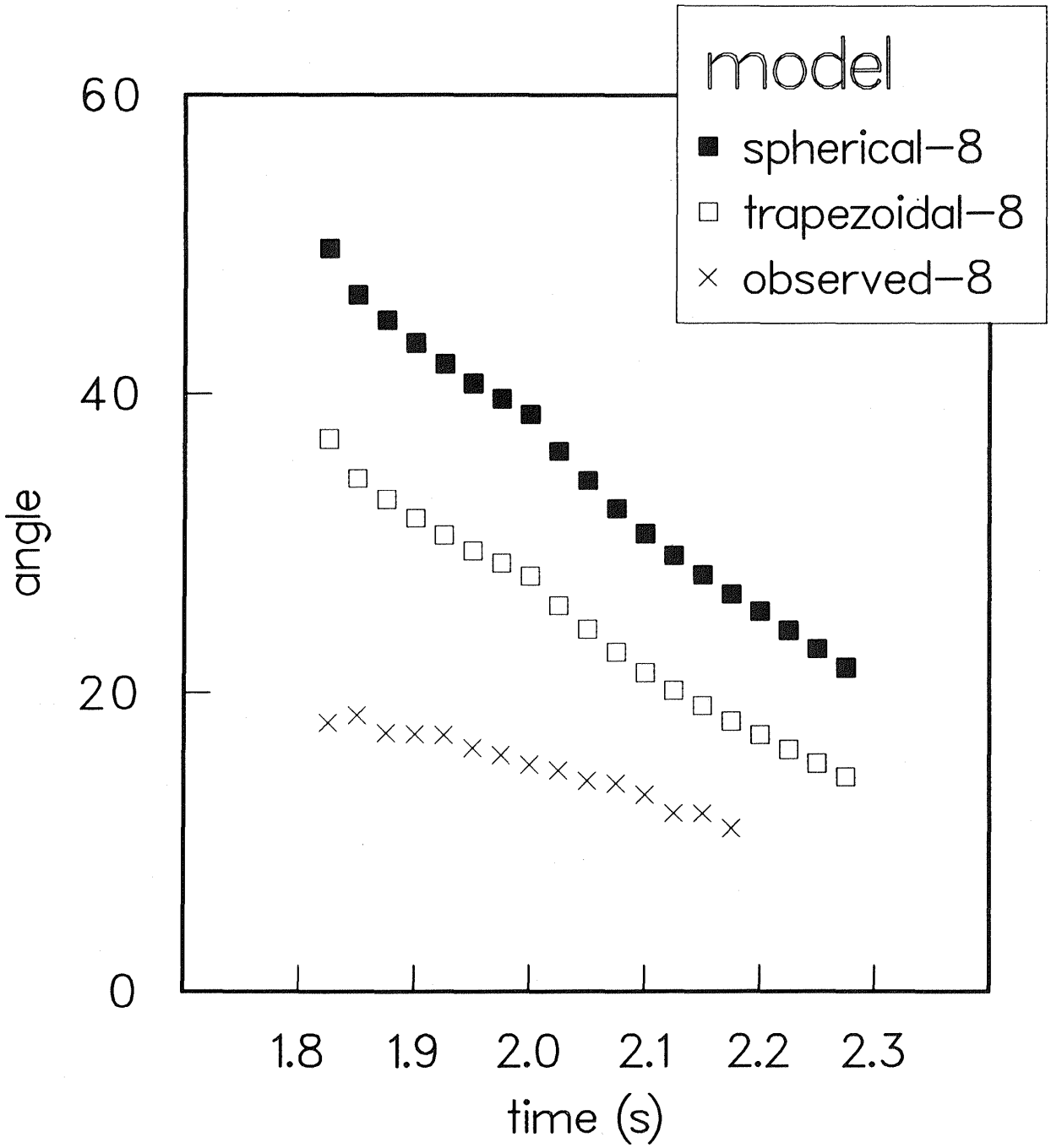

Figure 16. Apparent contact angle for molten Ti on Poco graphite (sample 3). Time origin for each curve arbitrarily shifted to 1.8 s for comparison with Figure 9.

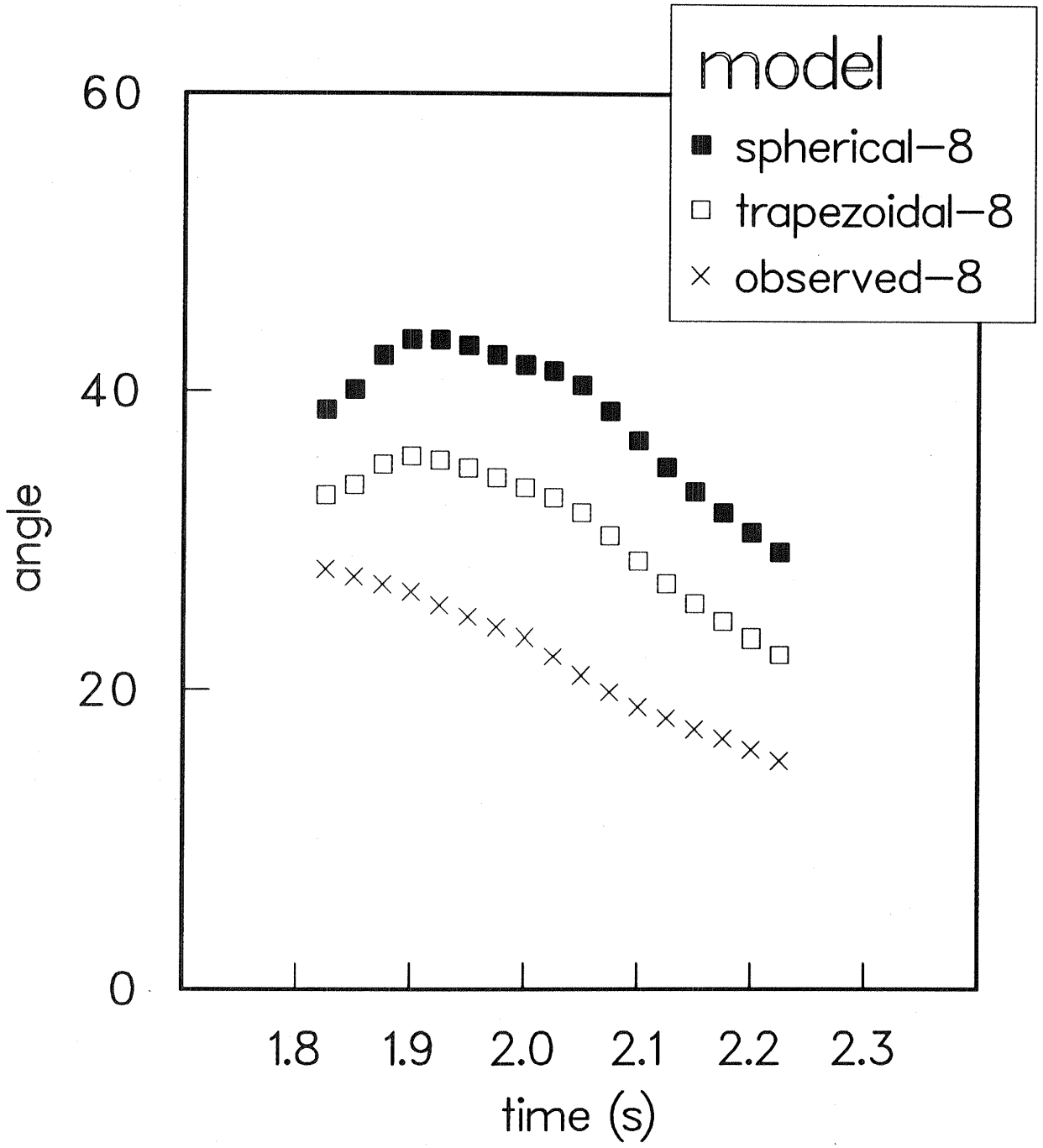

Figure 17. Apparent contact angle for sample 4. Time origin for each curve arbitrarily shifted to 1.8 s for comparison with Figure 9.

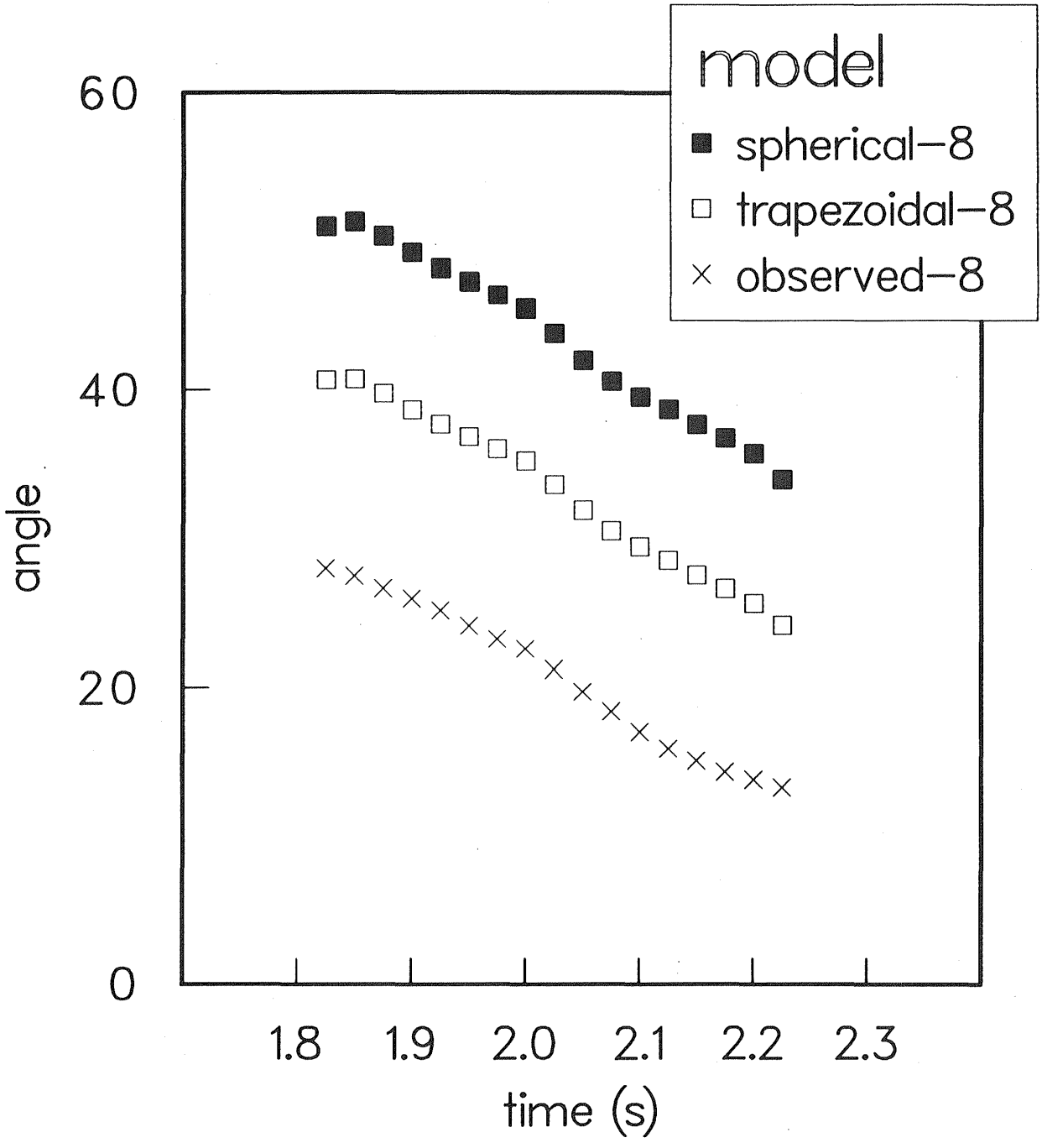

Figure 18. Apparent contact angle for sample 6. Time origin for each curve arbitrarily shifted to 1.8 s for comparison with Figure 9.

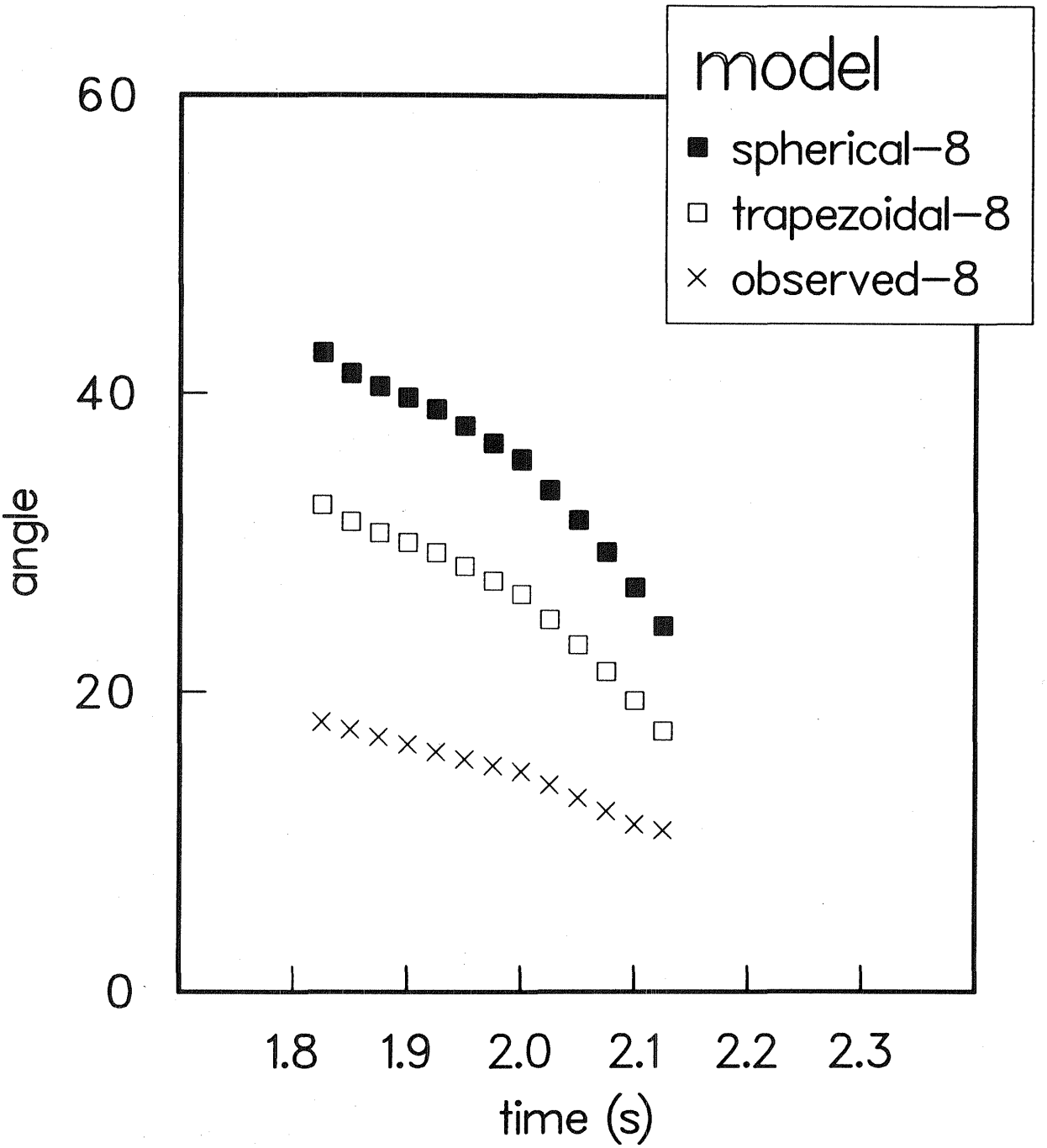

Figure 19. Apparent contact angle for sample 7. Time origin for each curve arbitrarily shifted to 1.8 s for comparison with Figure 9.

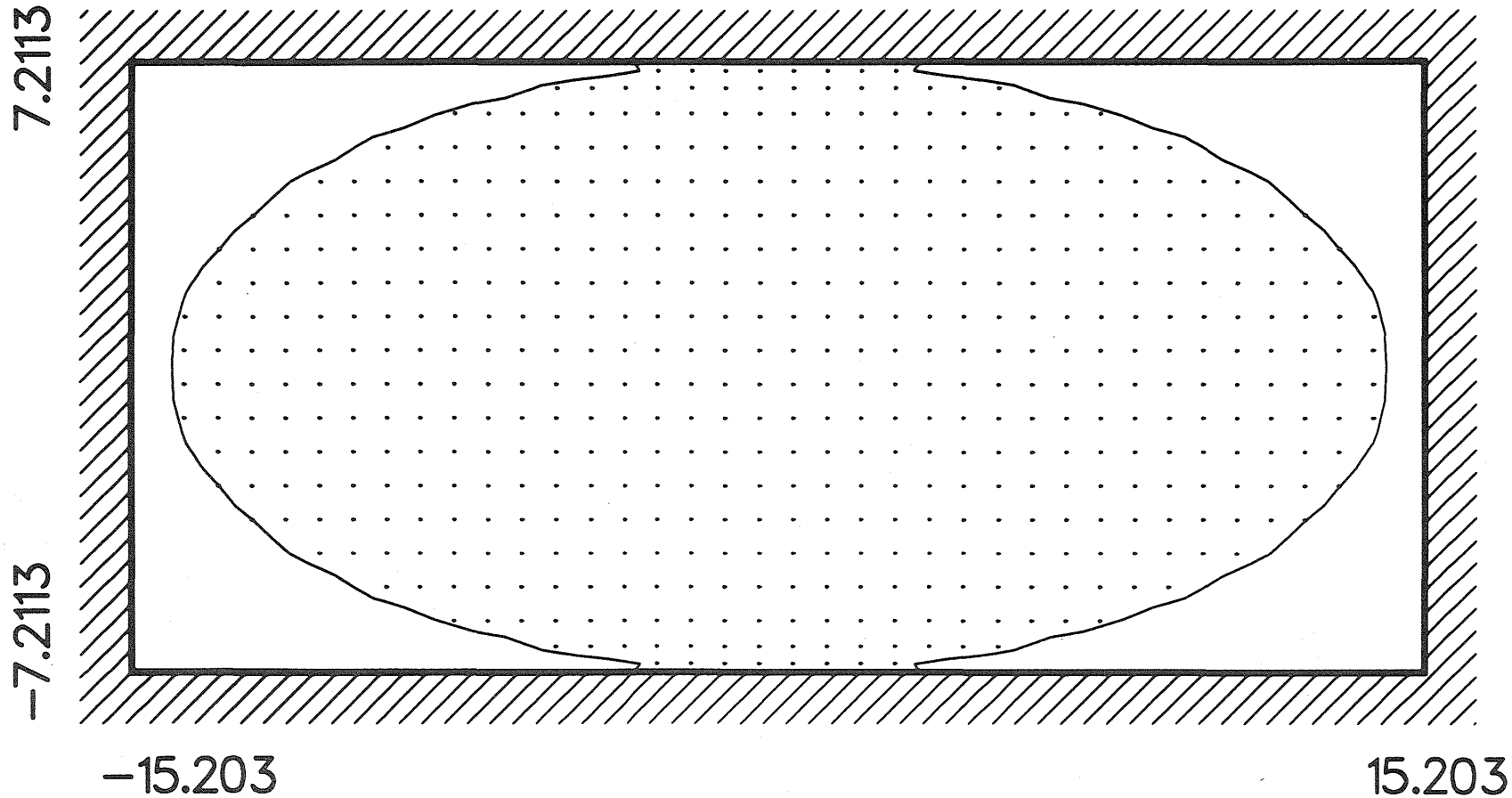

Figure 20. Initial elliptical configuration with major axis 28.8 μm and minor axis 14.4 μm. Approximate void fraction is 20%.

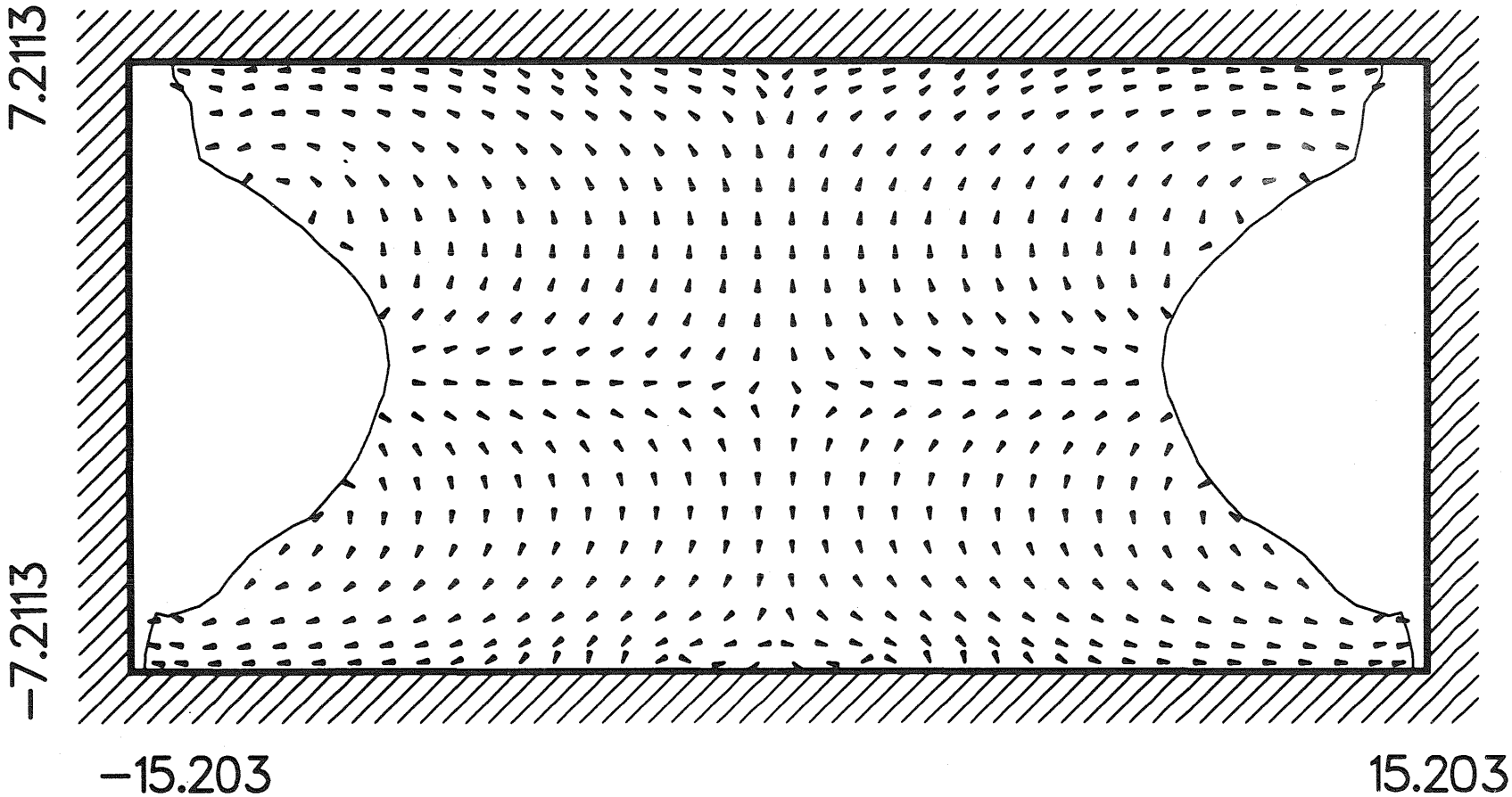

Figure 21. Configuration after 1.2 μs.

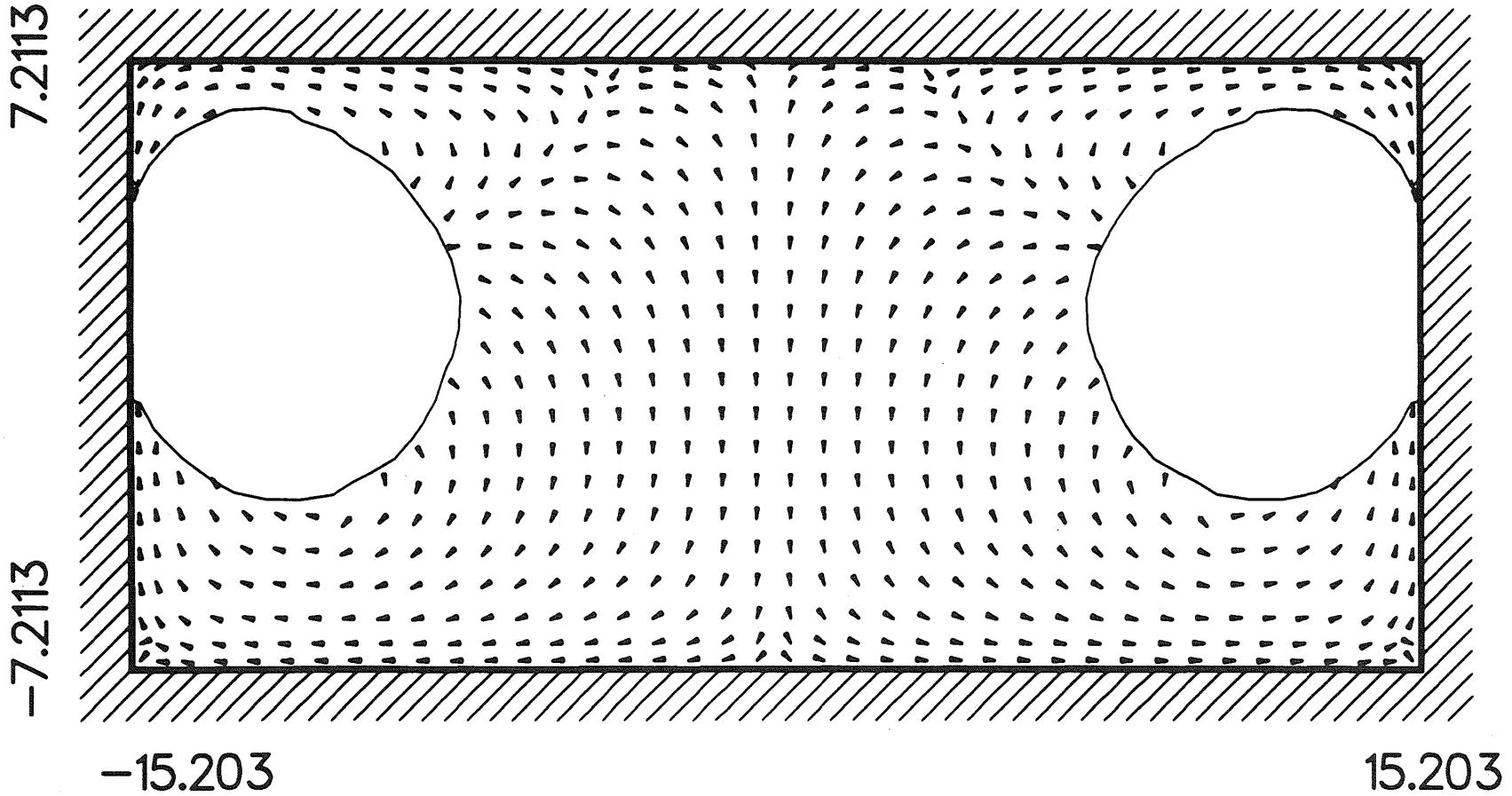

Figure 22. Configuration after 2.9 μs.

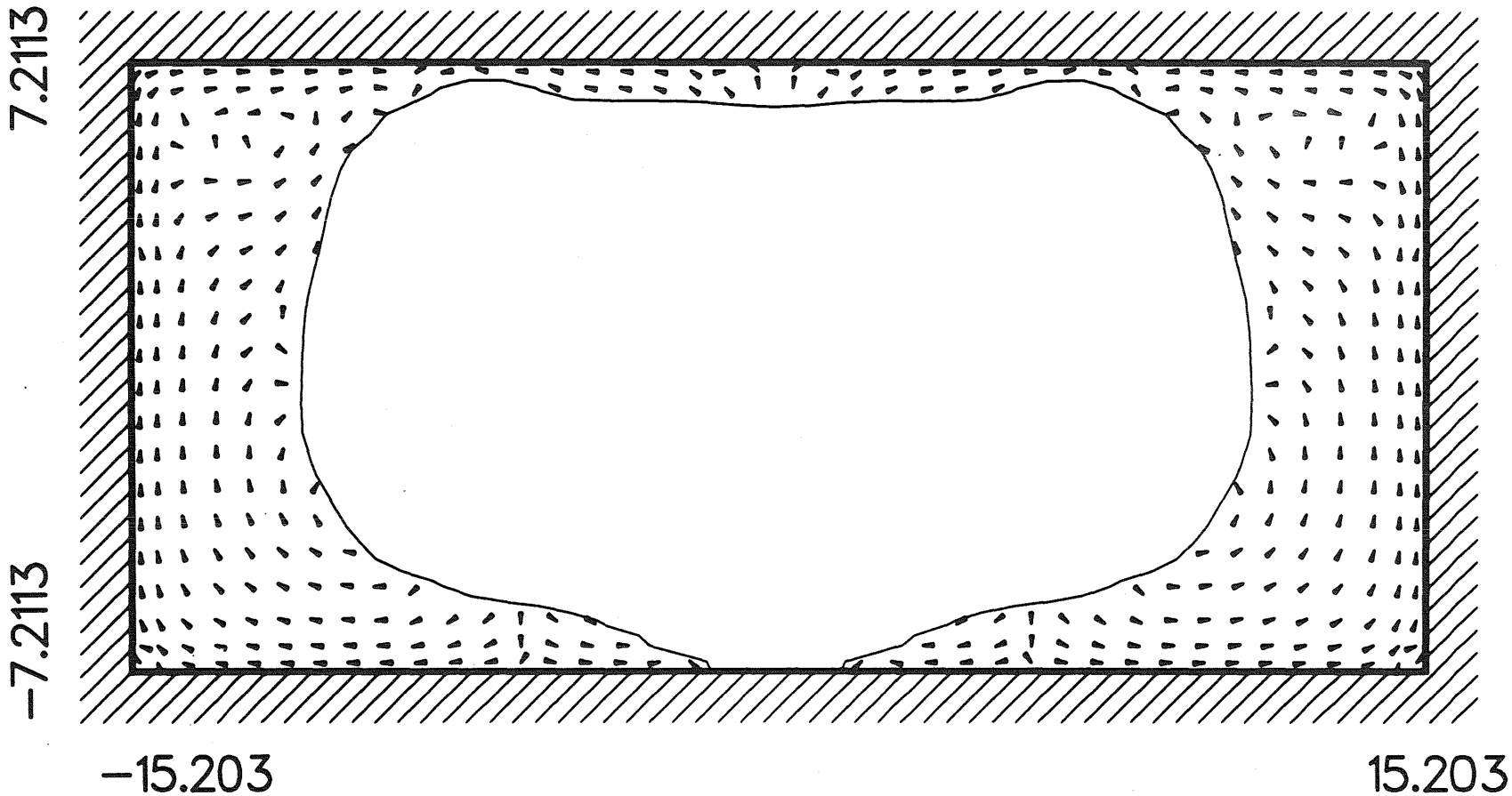

Figure 23. Configuration after 5.9 μs.

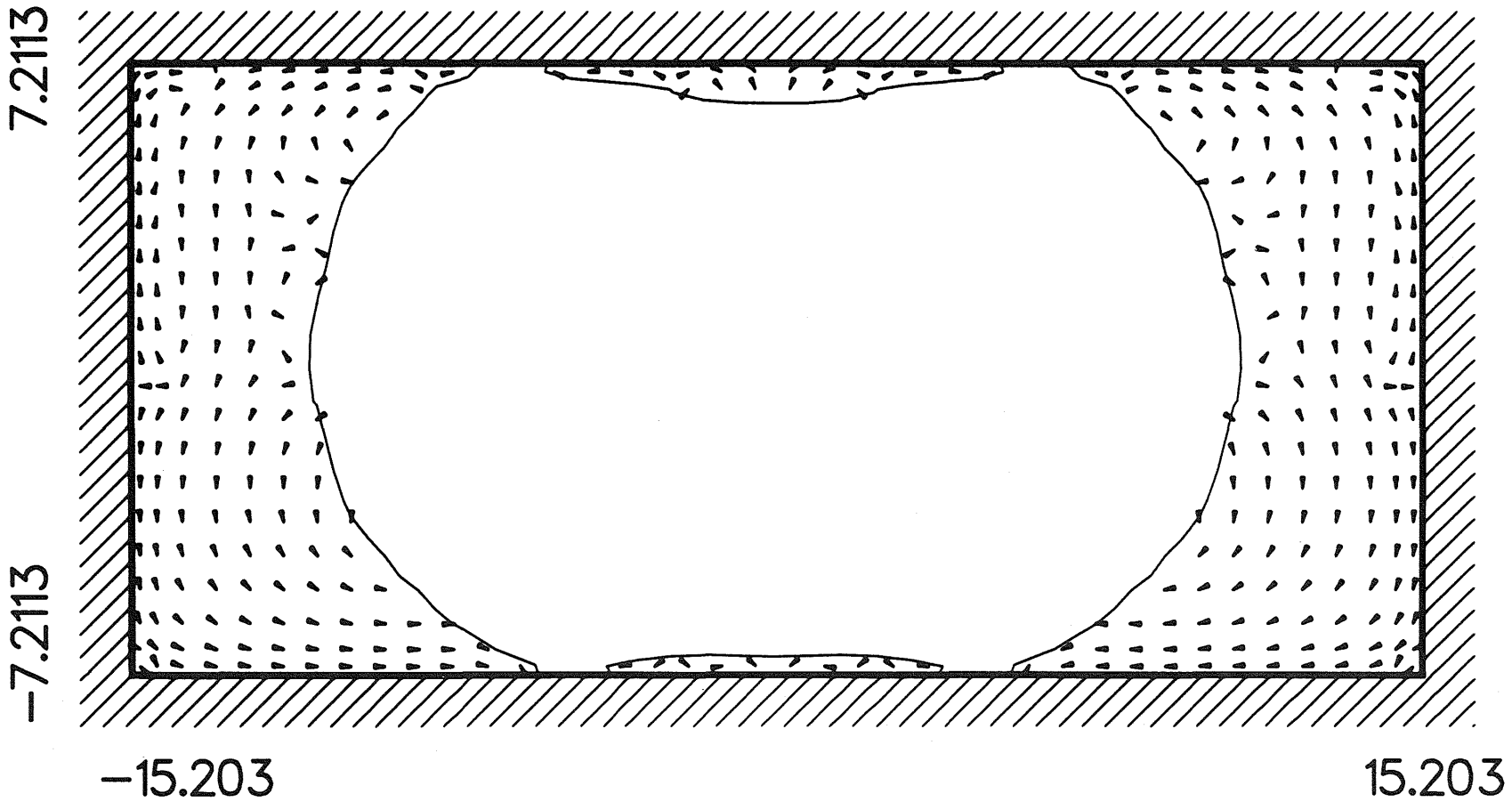

Figure 24. Configuration after 8.8 μs.

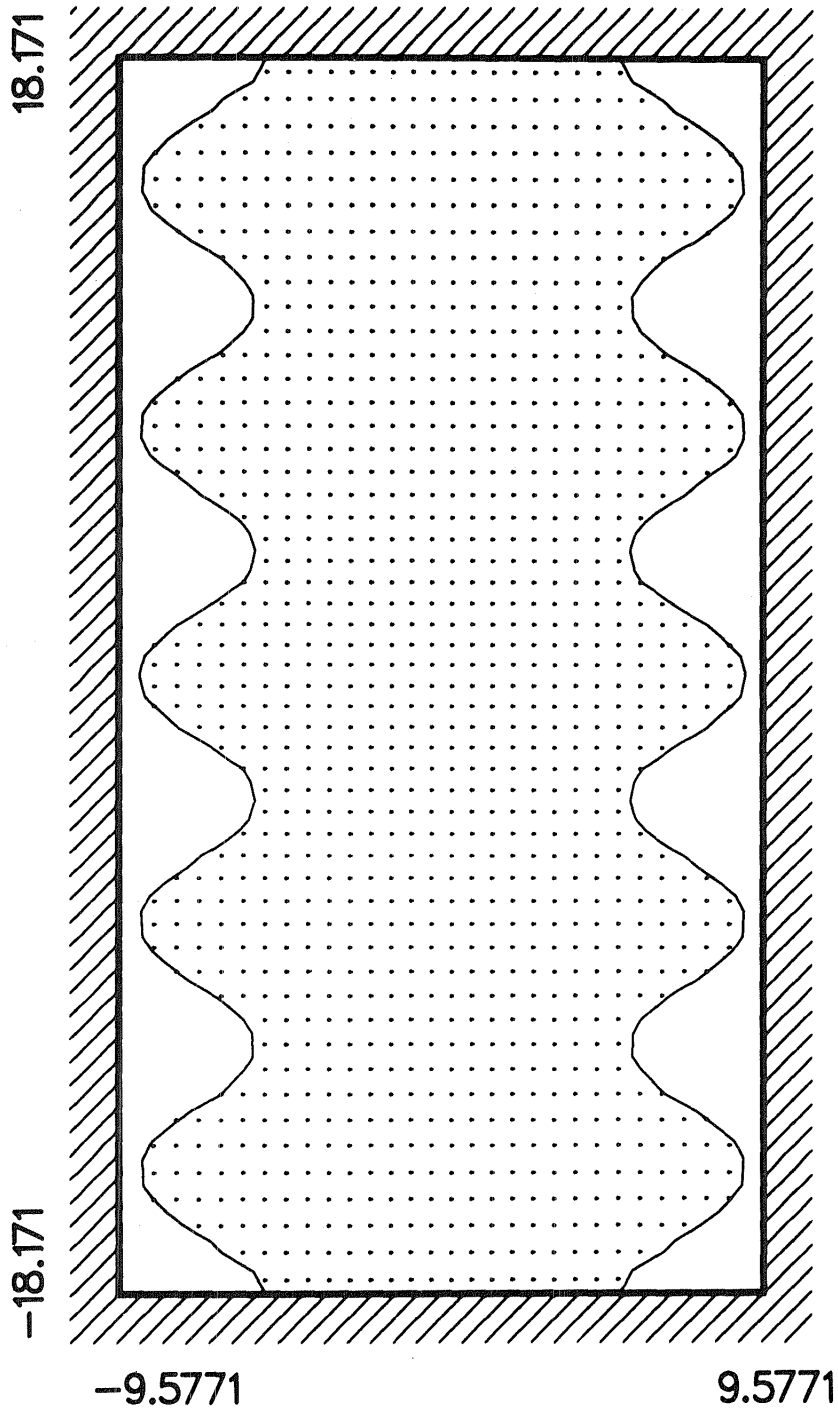

Figure 25. Initial irregular configuration with major axis 36.3 μm and minor axis 19.1 μm. Approximate void fraction is 20%.

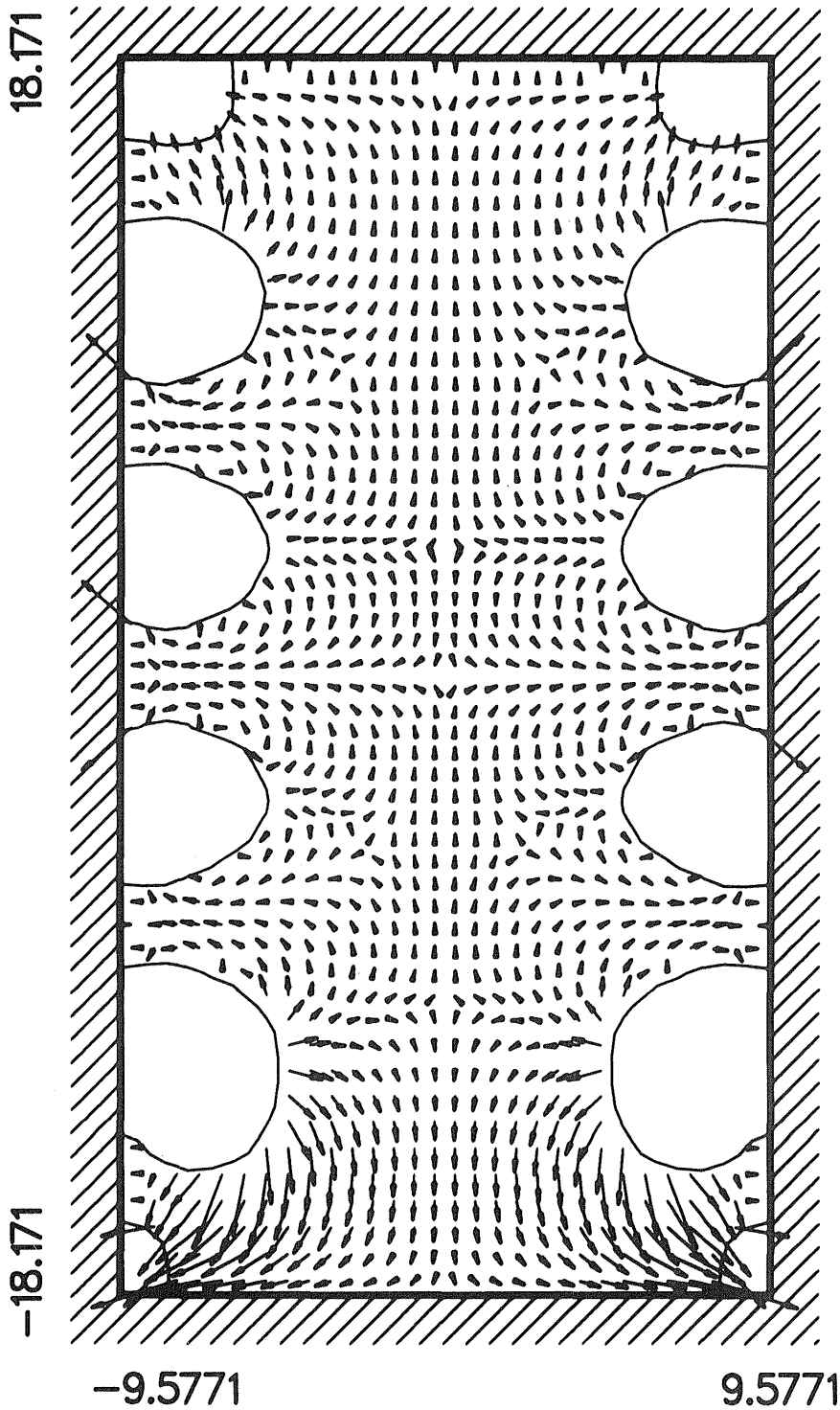

Figure 26. Configuration after 0.5 μs.

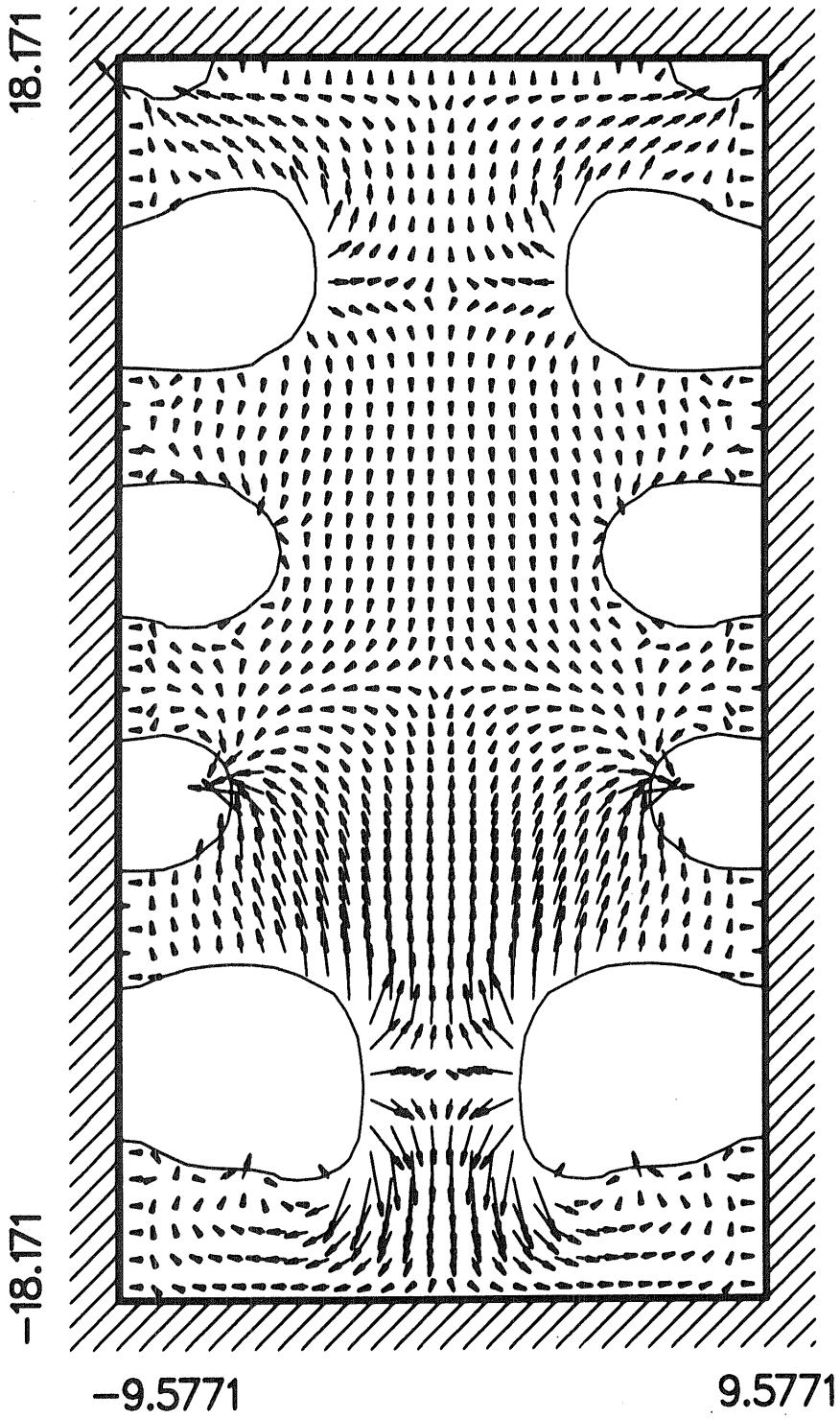

Figure 27. Configuration after 0.9 μs.

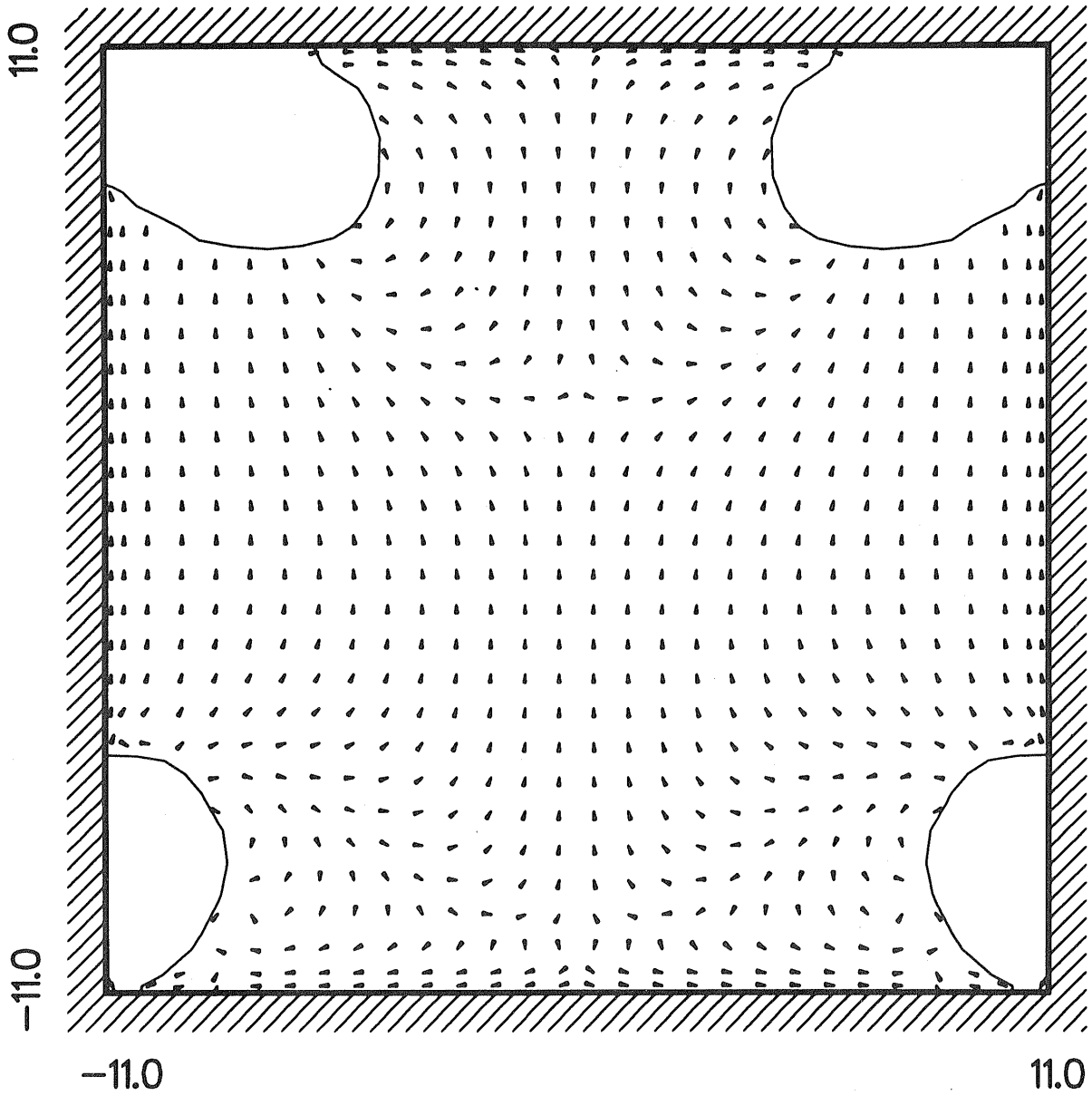

Figure 28. After 8.8 μs starting initially from a cylindrical configuration with r=10 μm and h=20 μm, four void regions remain with no gravity. Density is 86% of theoretical.

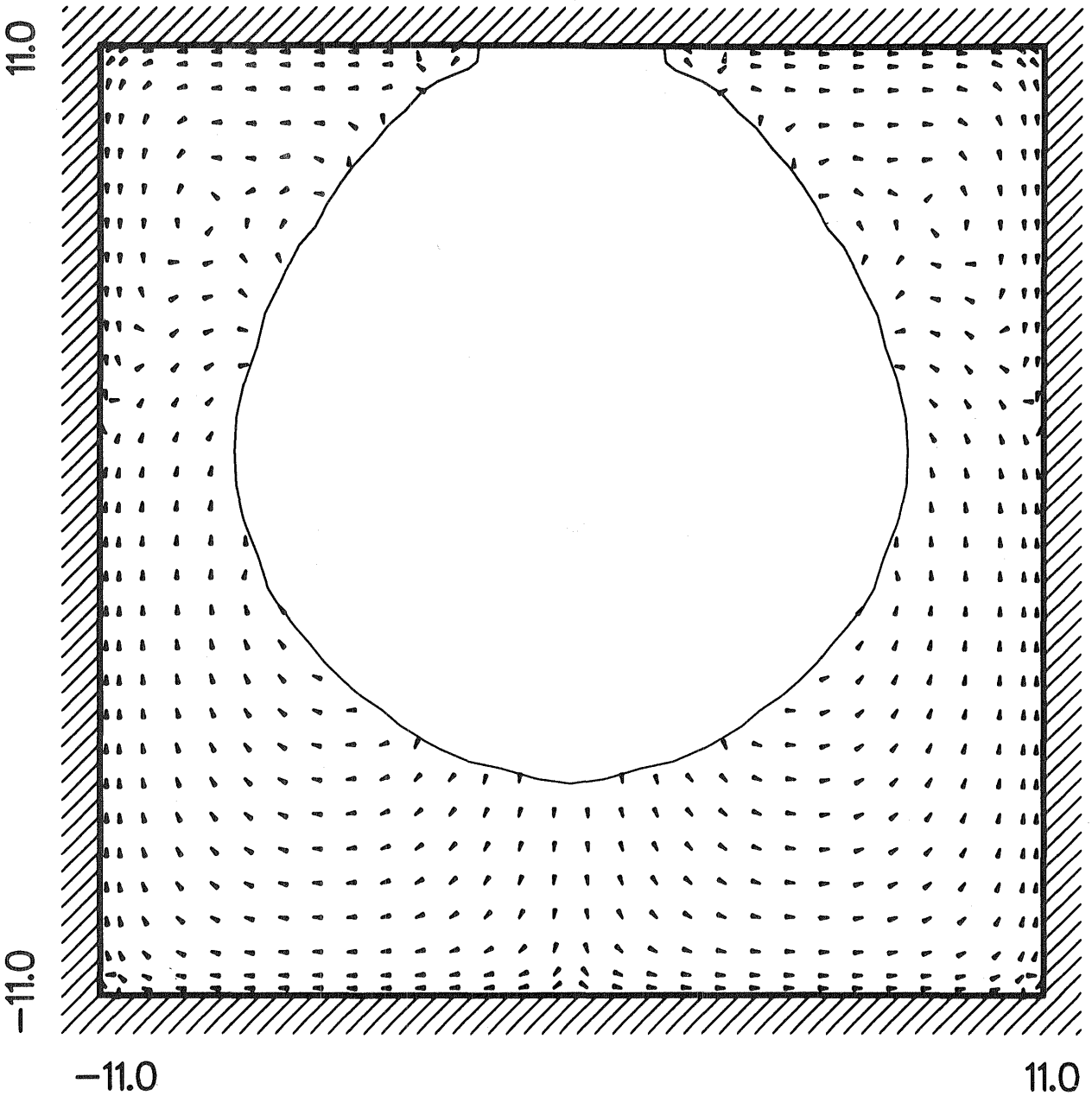

Figure 29. Same situation as in Figure 27 except with gravitational force applied. Rings have coalesced into a single spherical void.

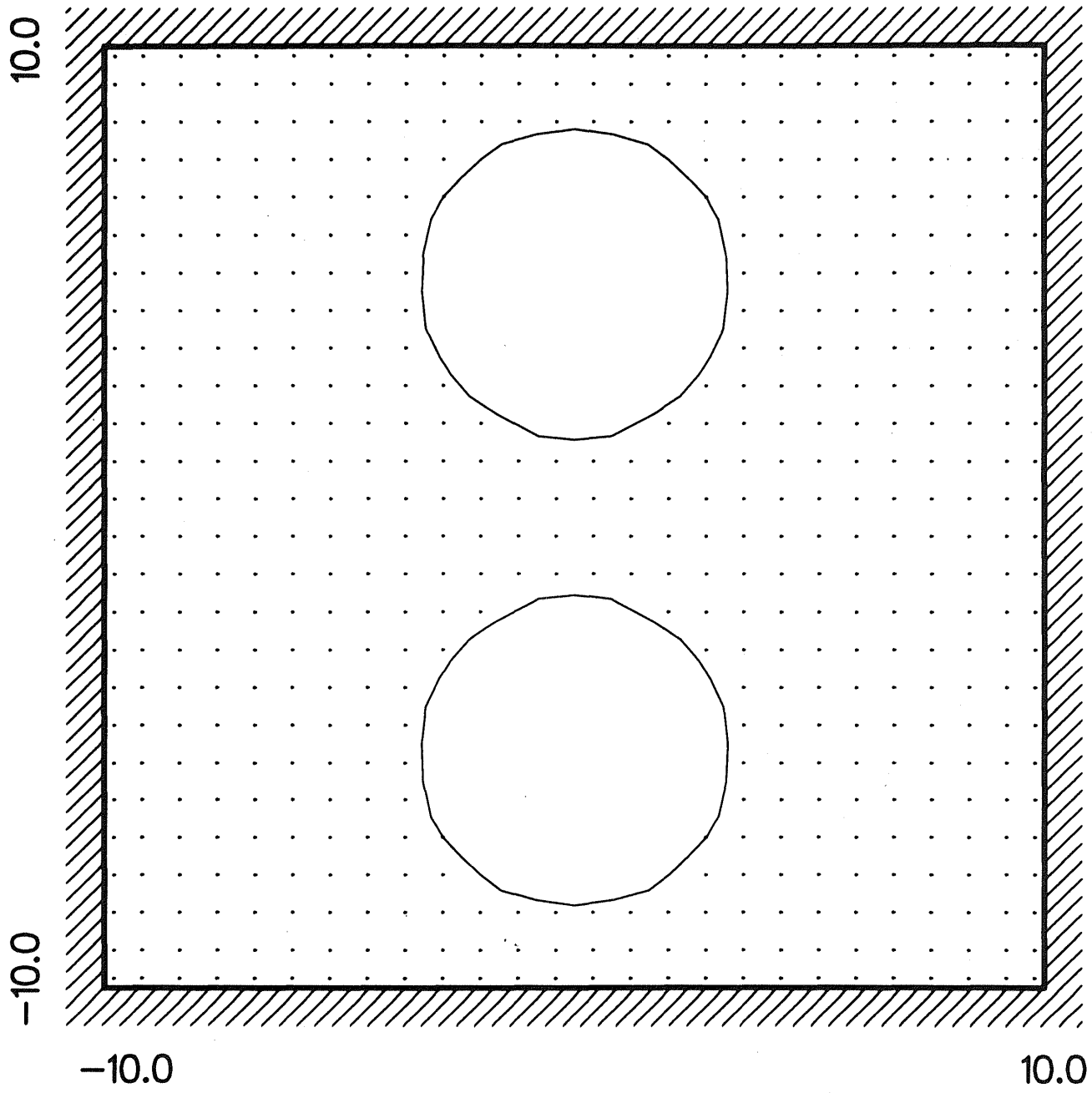

Figure 30. Initial metstable two bubble configuration. Each bubble is 6 μm in diameter and the fluid is quiescent.

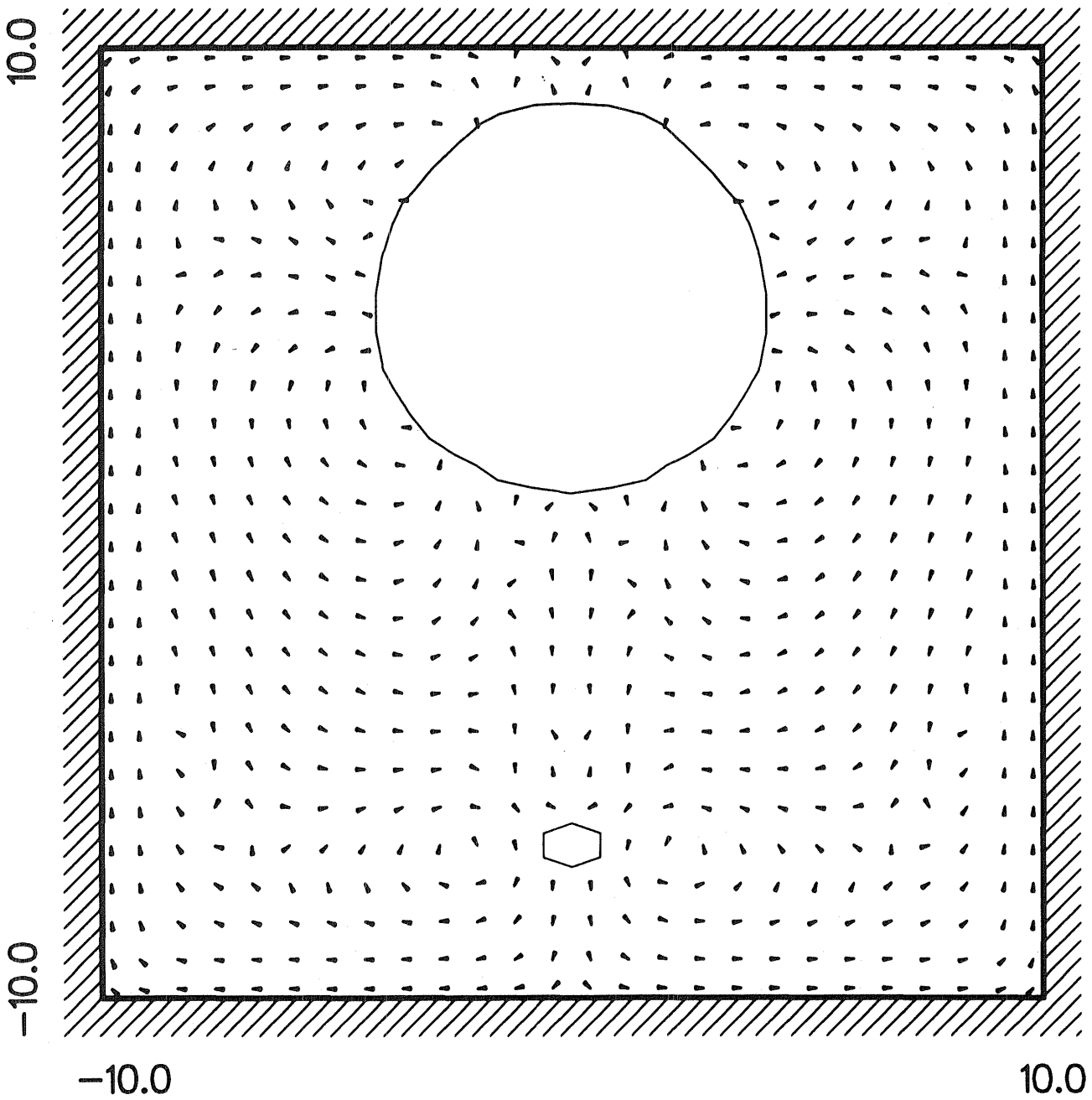

Figure 31. Flow field after 5.9 μs with gravity shows the upper bubble expanding and the lower bubble contracting.

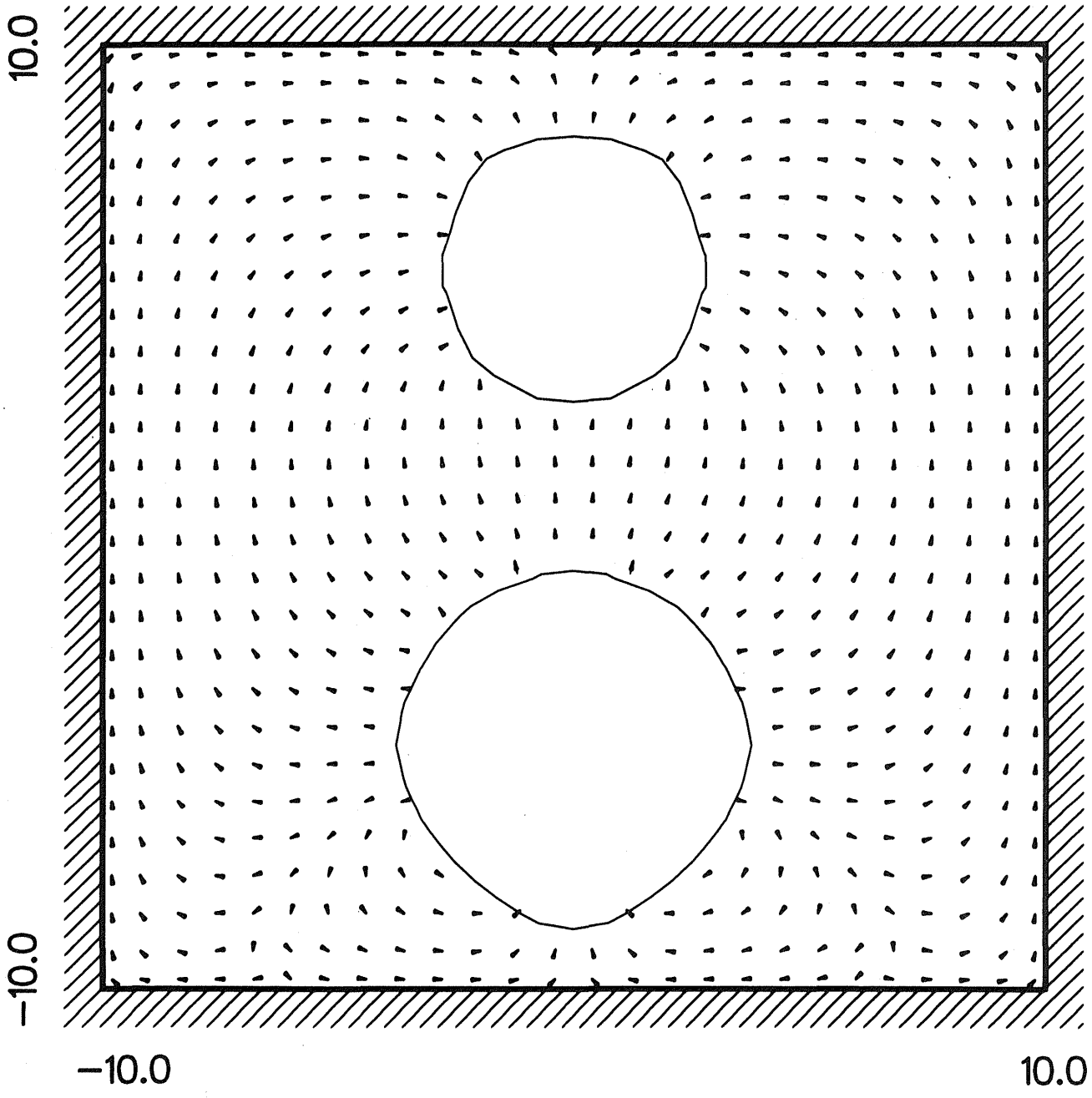

Figure 32. Flow field after 5.9 μs with no gravity shows opposite process, upper bubble contracting and lower bubble expanding.

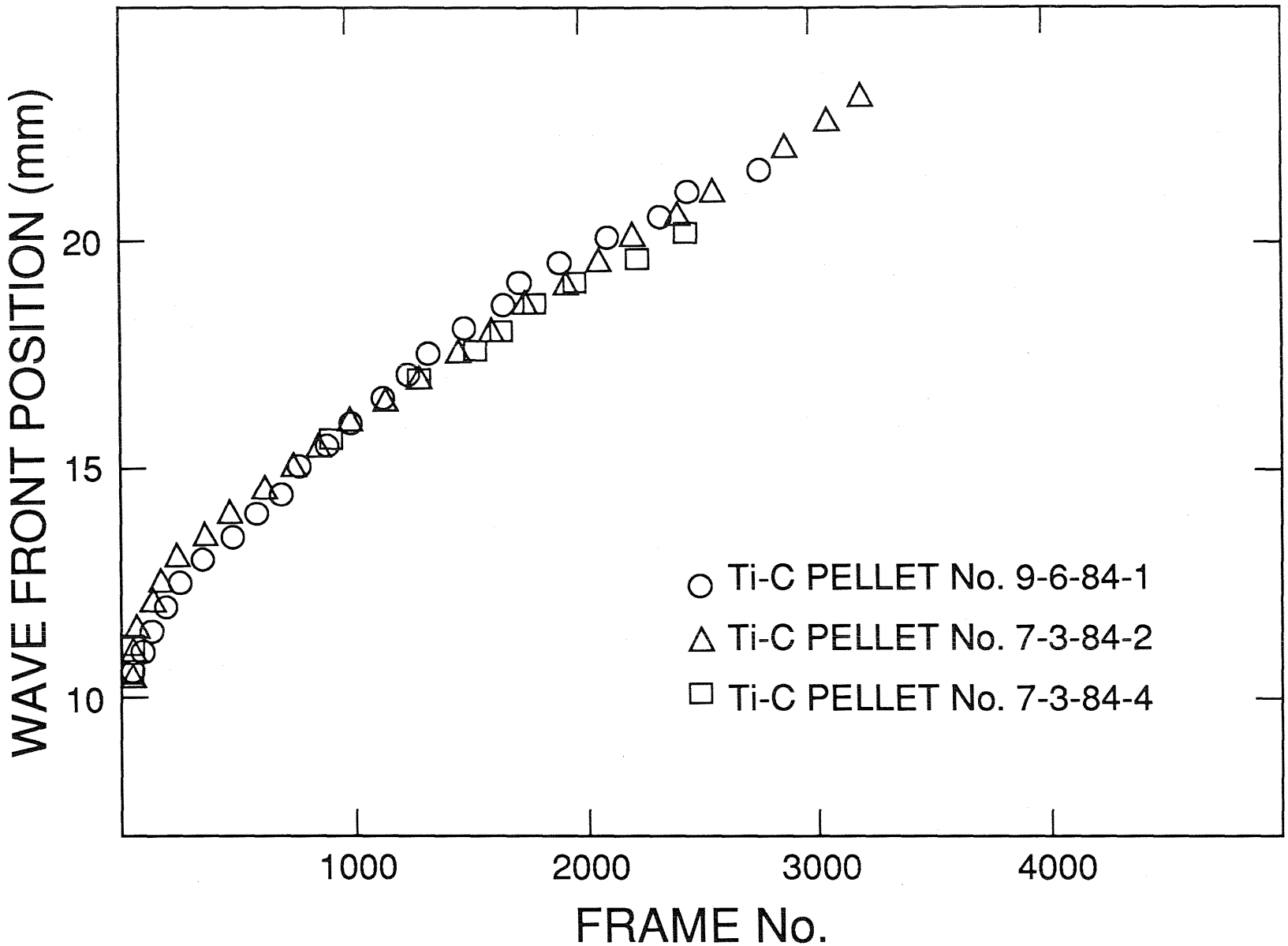

Figure 33. Coumbustion wave propagation in Ti + C pellets.

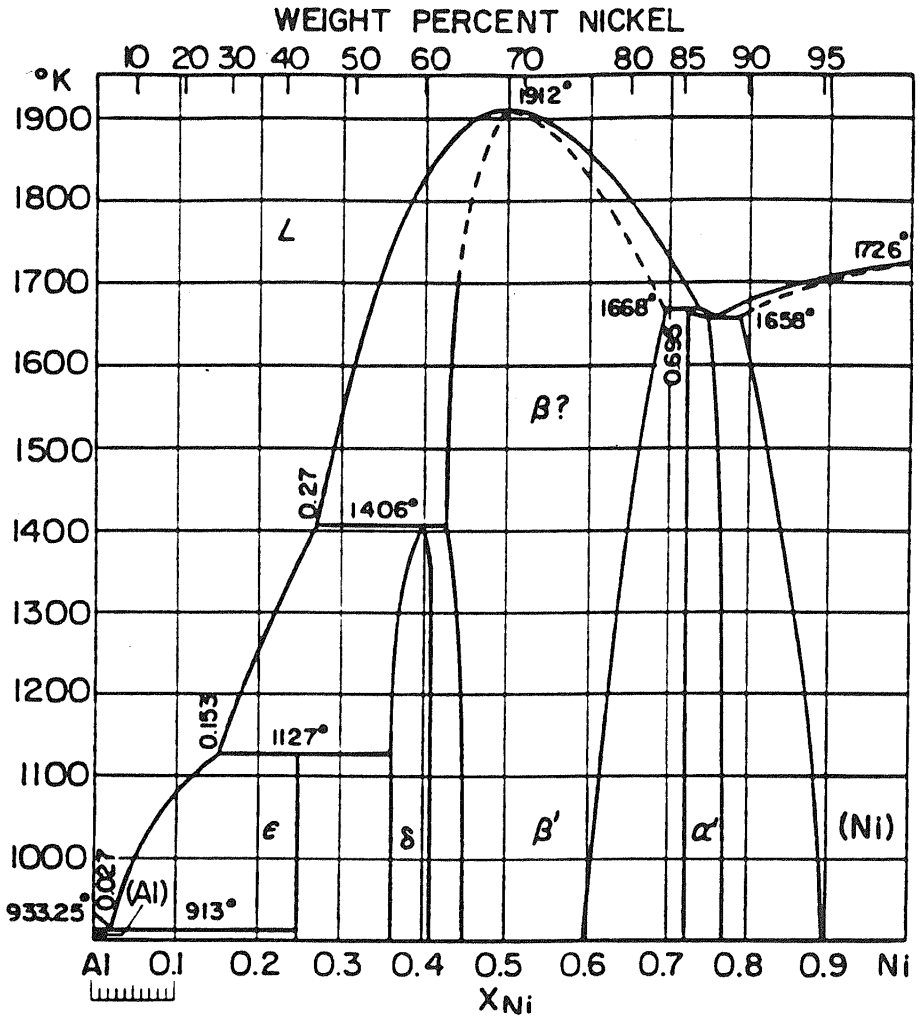

Figure 34. Phase diagram for the Al-Ni system.

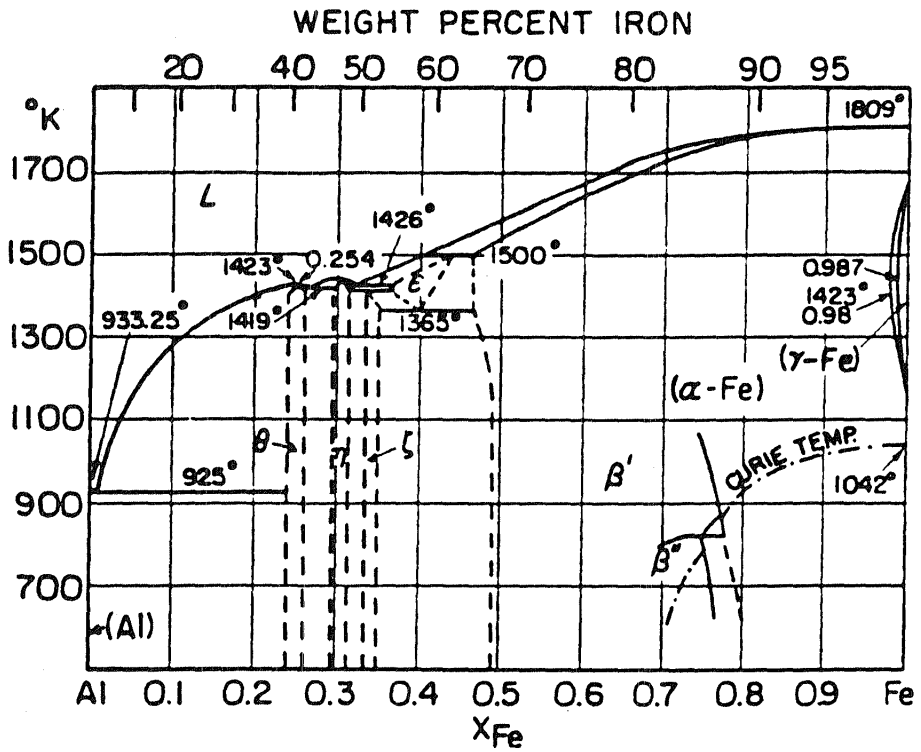

Figure 35. Phase diagram for the Al-Fe system.

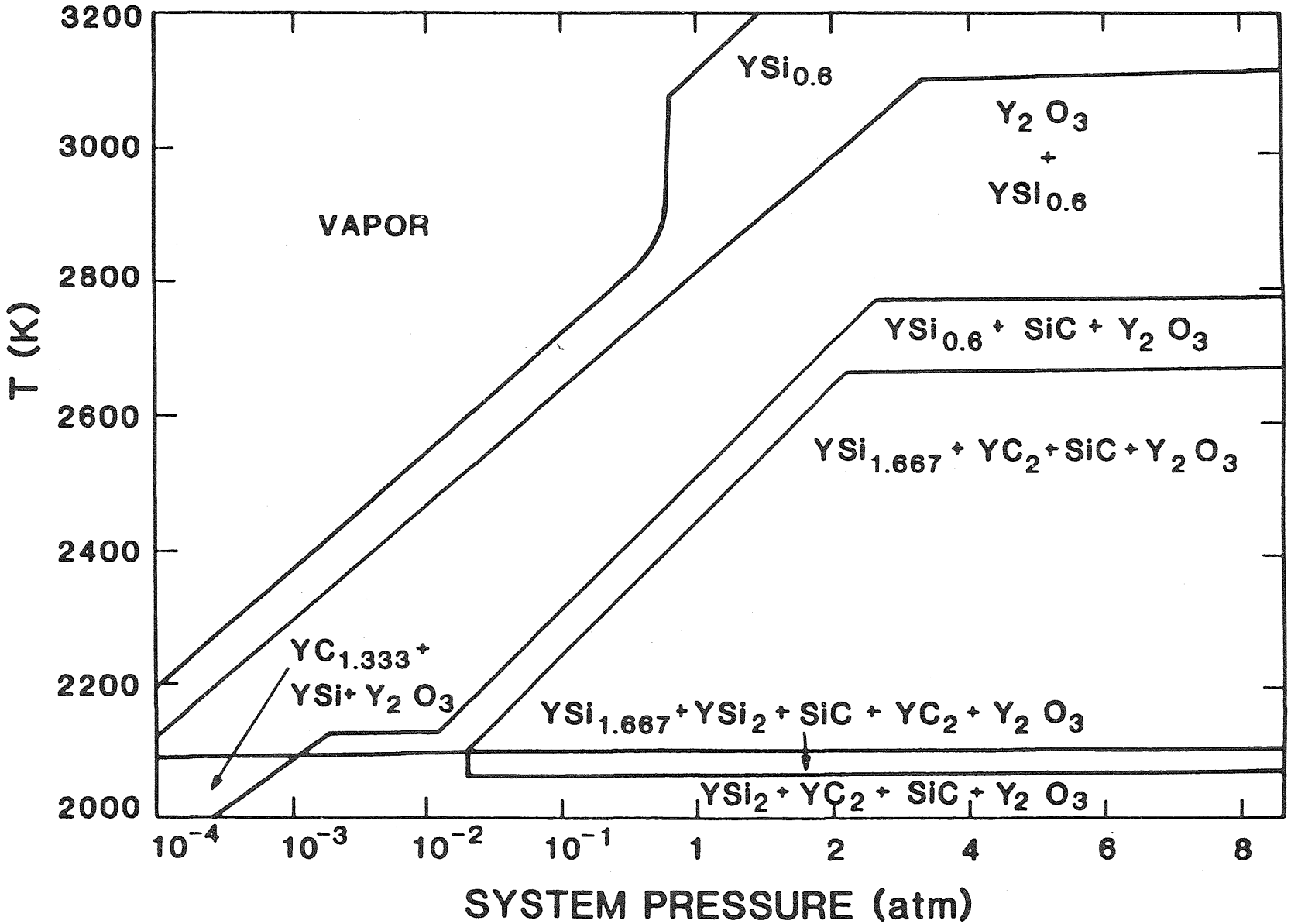

Figure 36. Calculated equilibrium condensed phase stability diagram for the Y-Si-C-O system.

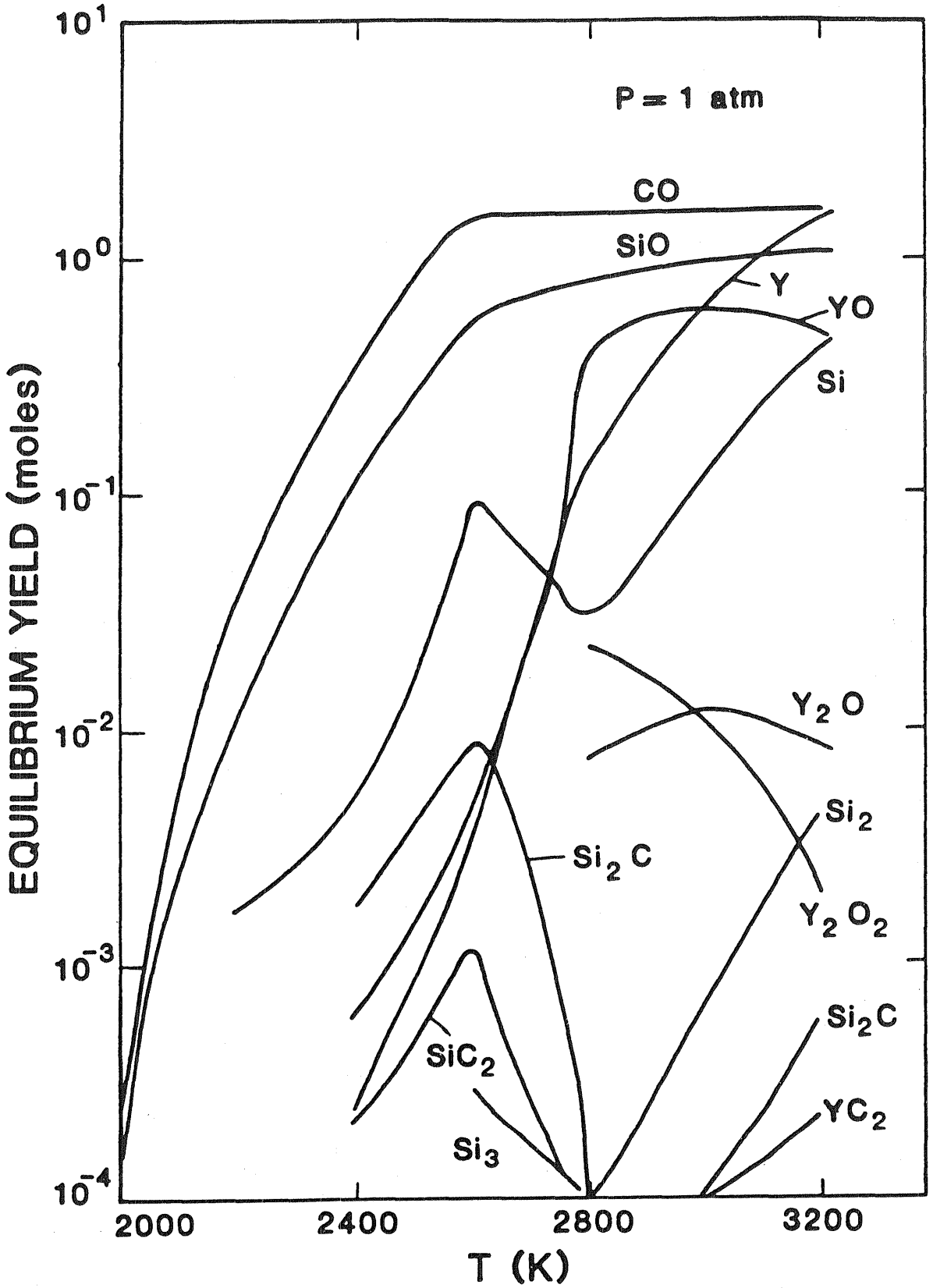

Figure 37. Calculated vapor phase equilibrium composition for the Y-Si-C-O system at 1 atmosphere of pressure.

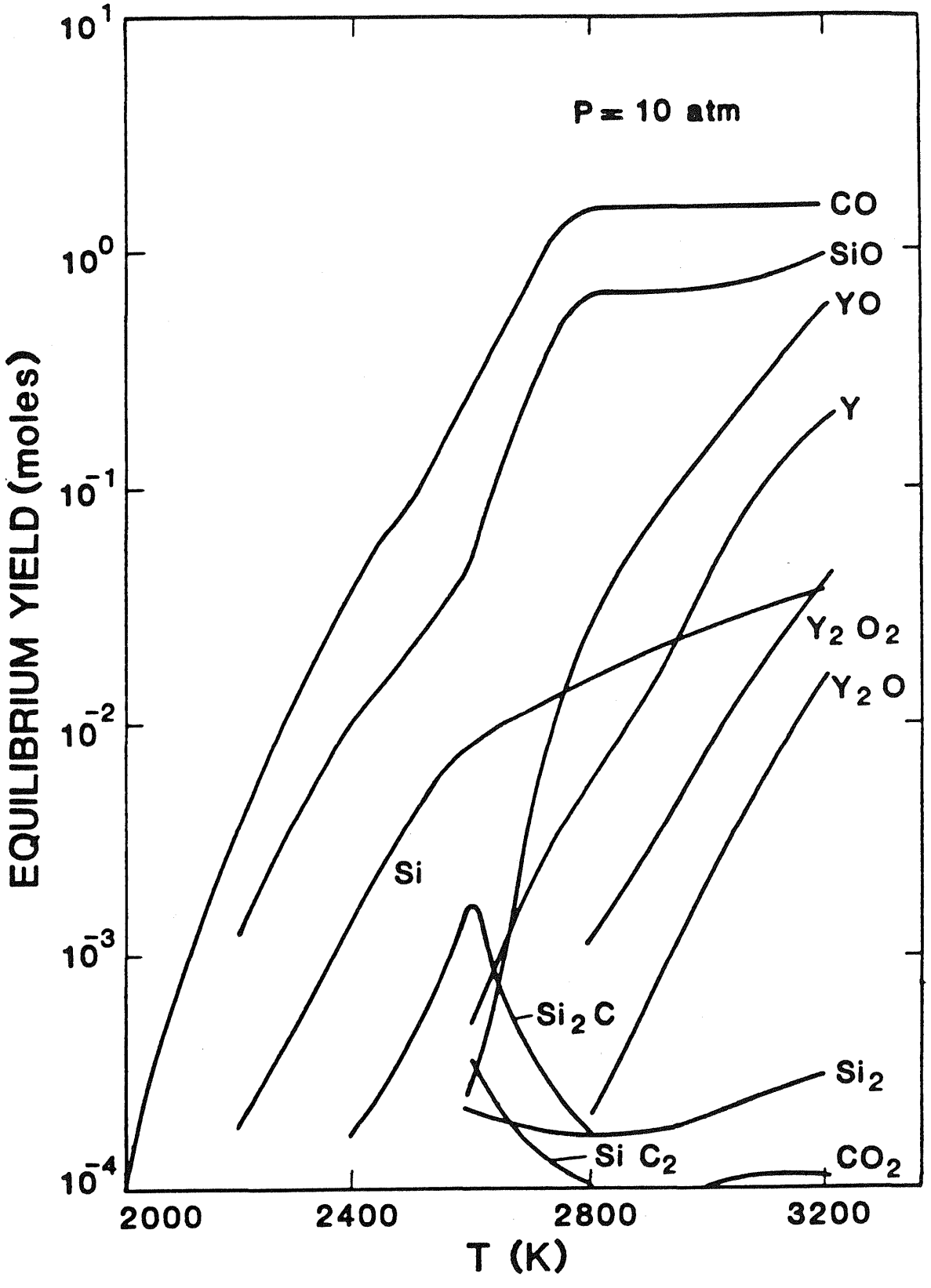

Figure 38. Calculated vapor phase equilibrium composition for the Y-Si-C-O system at 1 atmosphere of pressure.

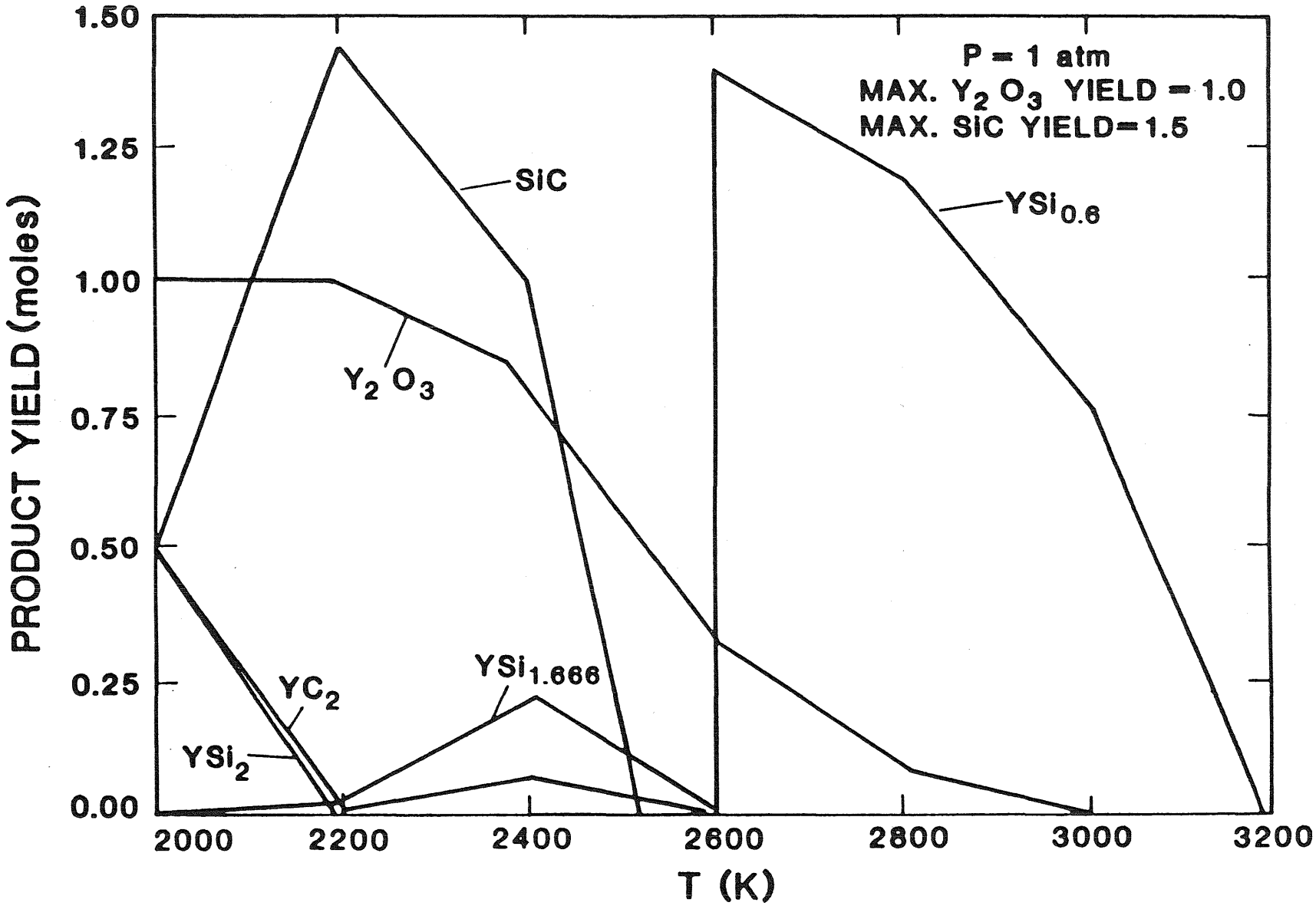

Figure 39. Condensed phase product yields for the Y-Si-C-O system at 1 atmosphere.

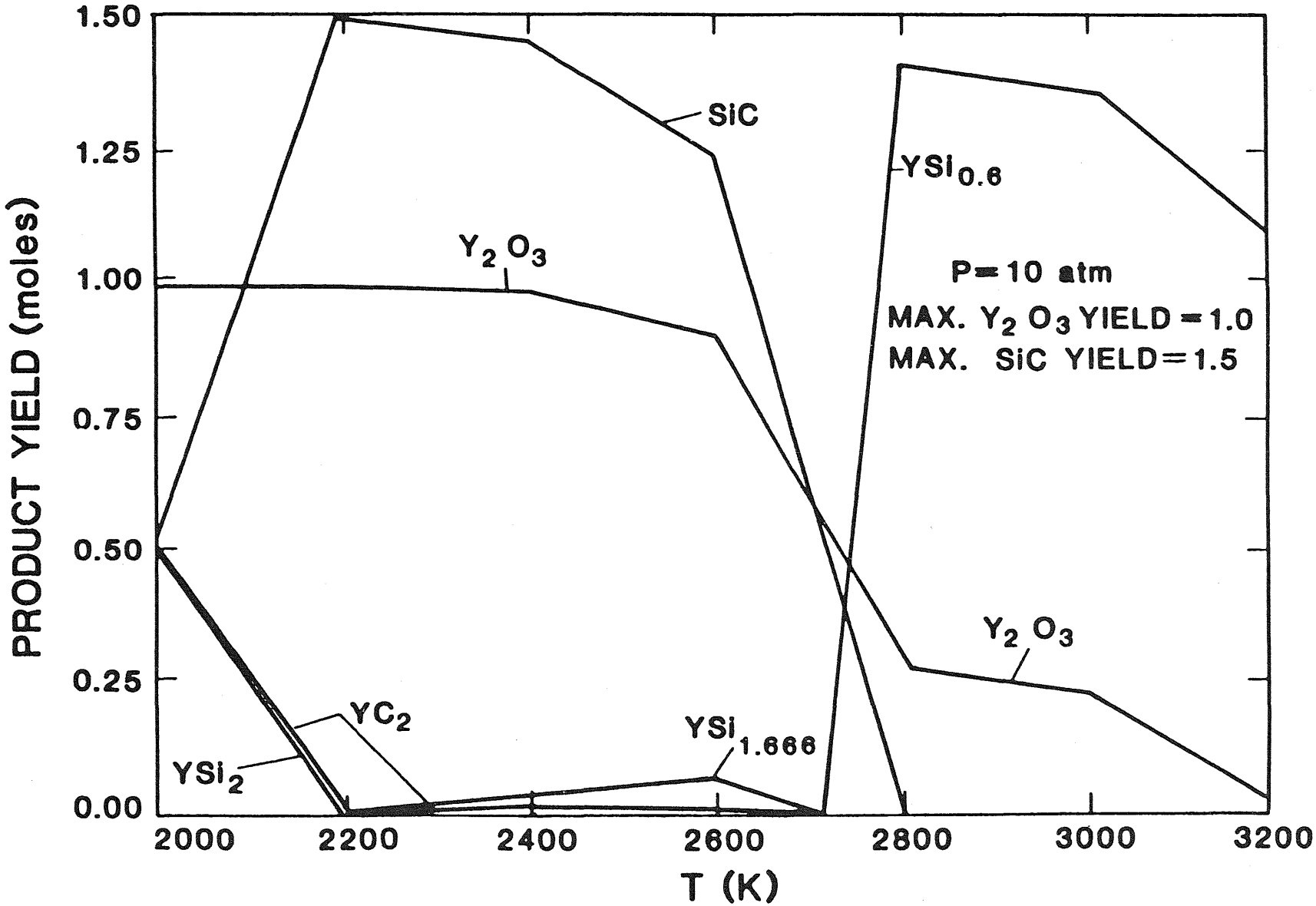

Figure 40. Condensed phase product yields for the Y-Si-C-O system at 1 atmosphere.

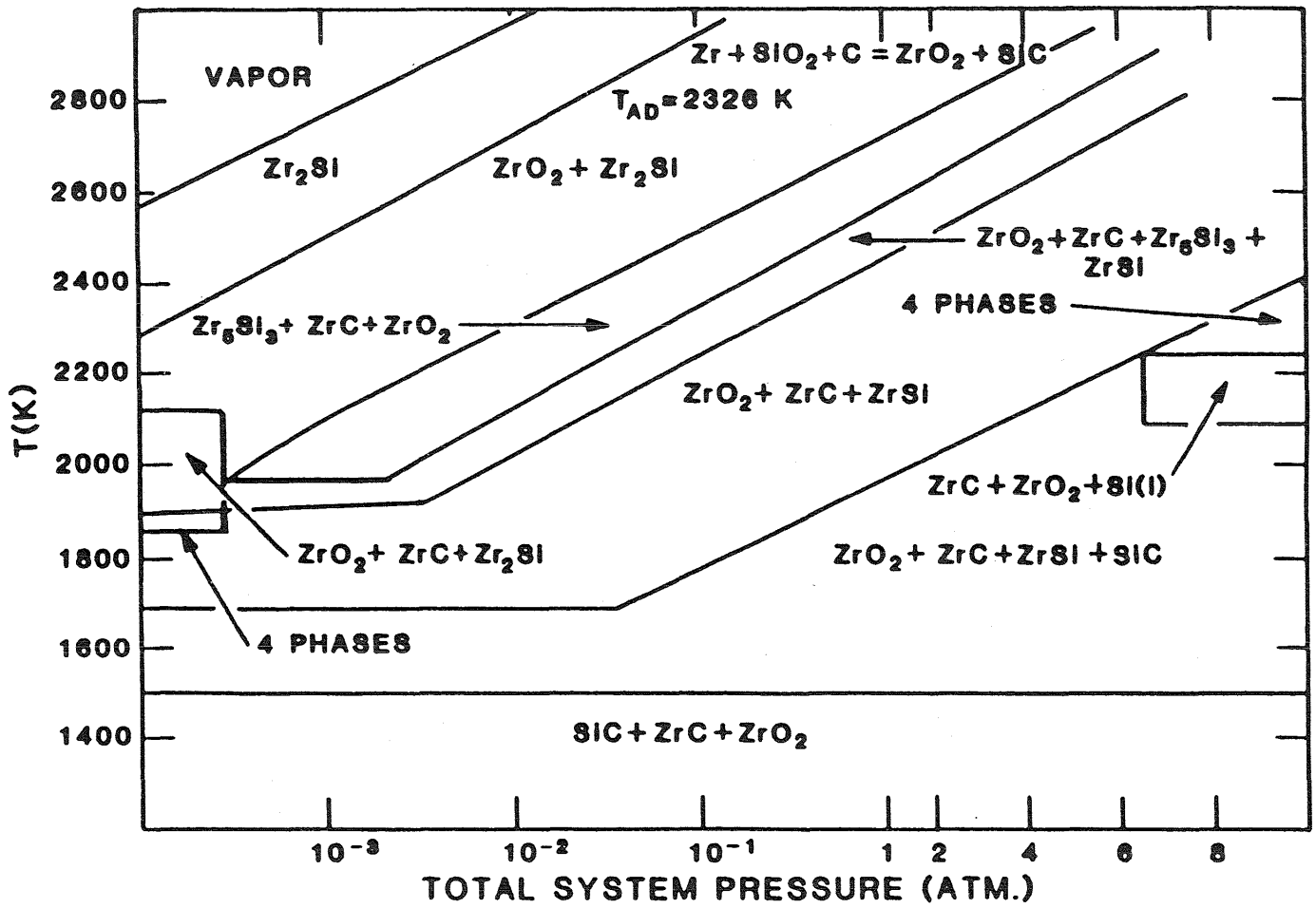

Figure 41 Calculated equilibrium condensed phase stability diagram for the Zr-Si-C-O system.

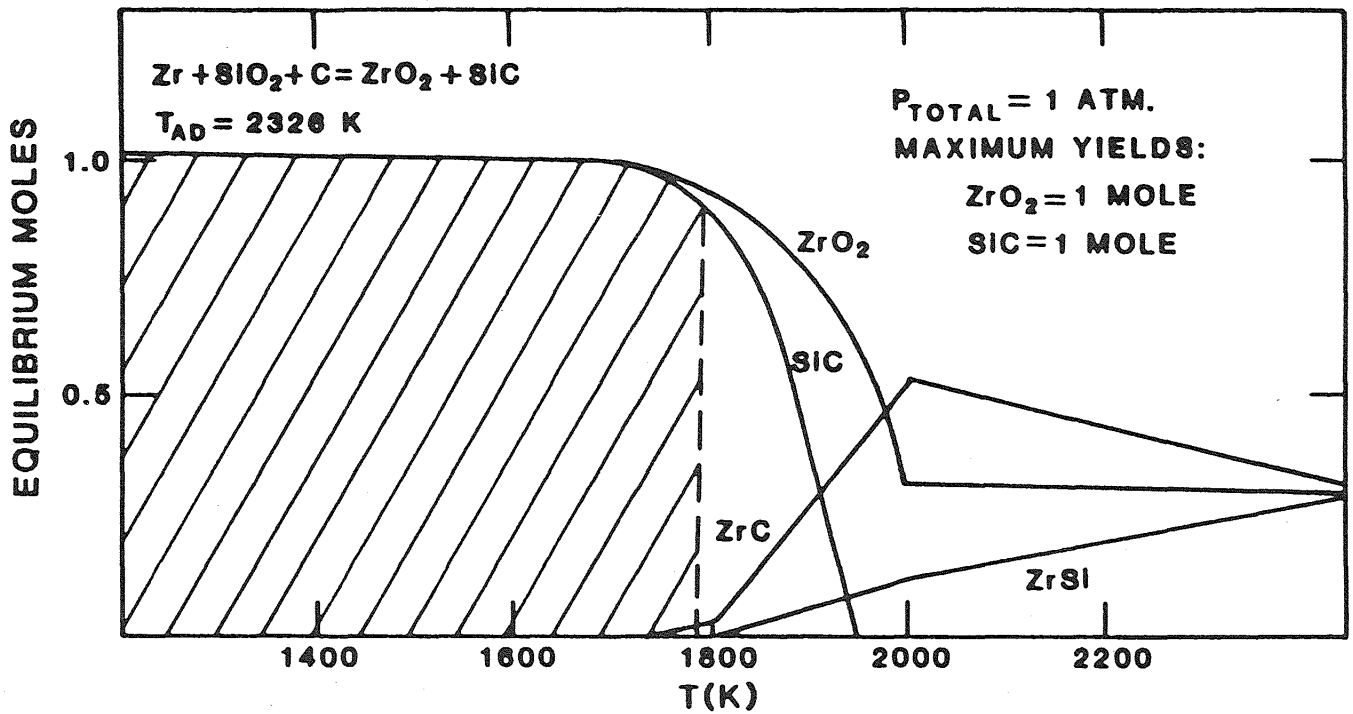

Figure 42. Condensed phase product yields for the Zr-Si-C-O system at 1 atmosphere.

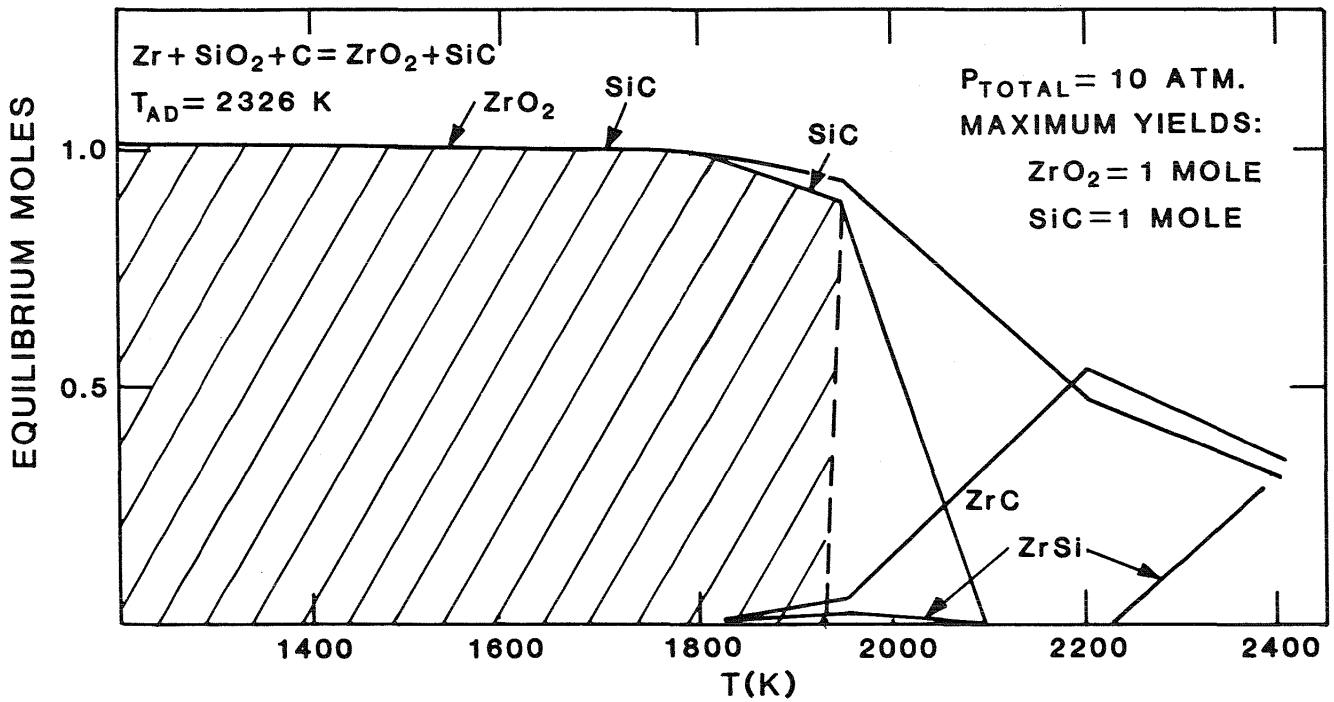

Figure 43. Condensed phase product yields for the Zr-Si-C-O system at 10 atmospheres.

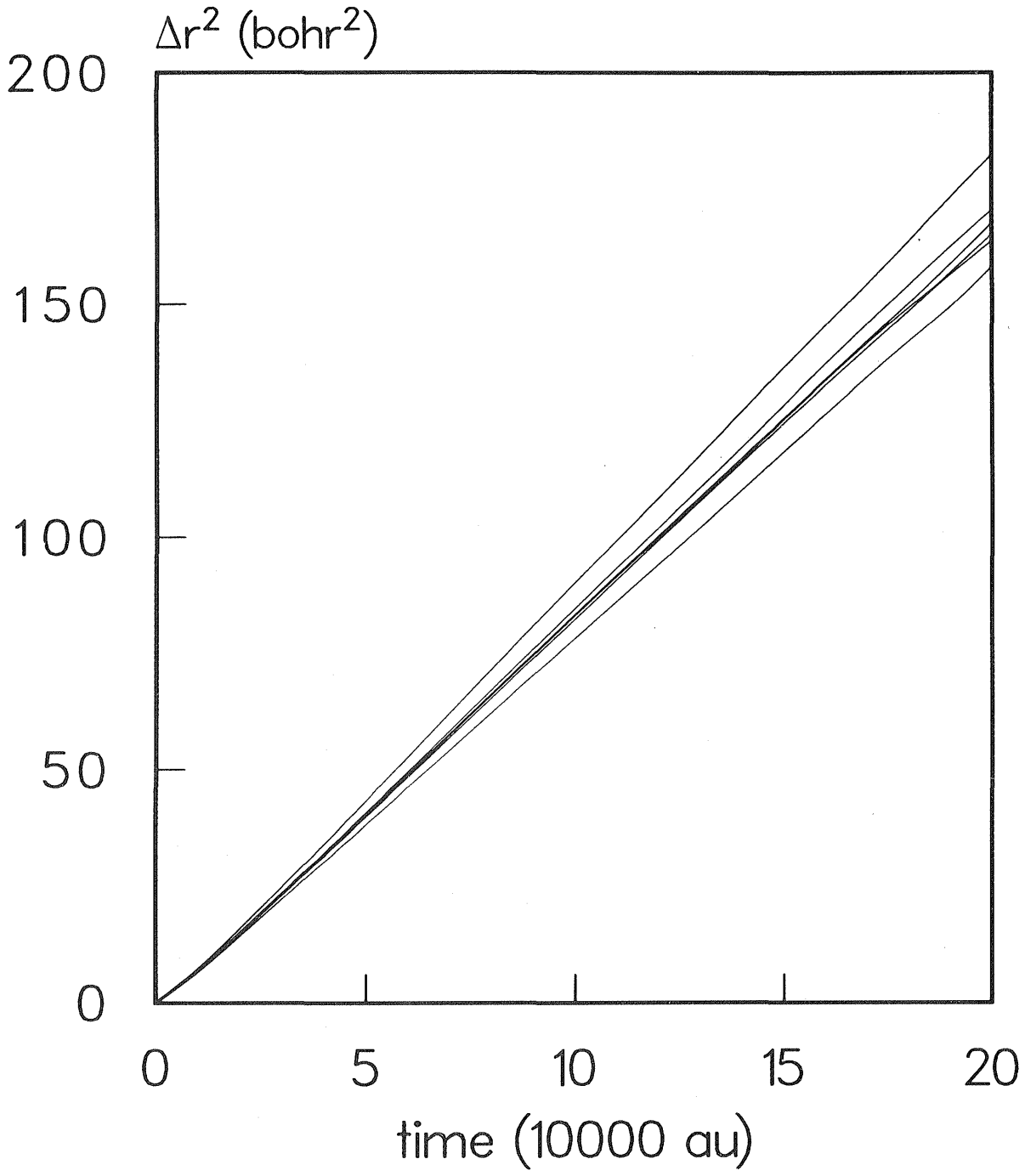

Figure 44. Mean square displacements of Ti at 2000 K as functions of time for collections of 16 trajectories.

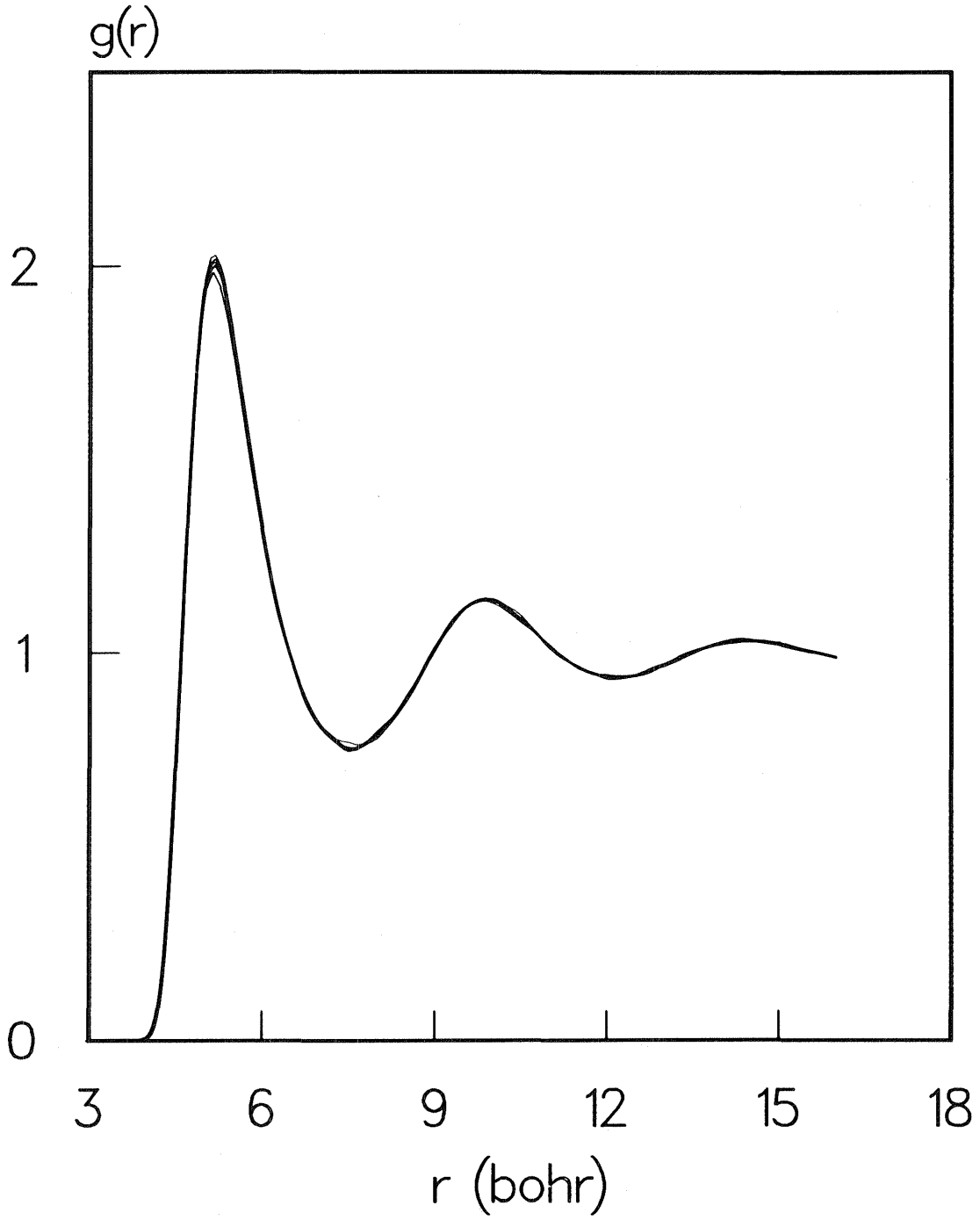

Figure 45. Radial distribution function for Ti at 2000 K for collections of 16 trajectories.

NASA
National Aeronautics and Space Administration

Report Documentation Page

1. Report No.	2. Government Accession No.	3. Recipient's Catalog No.
NASA CR-4163		

4. Title and Subtitle	5. Report Date
Solid-State Combustion Synthesis of Ceramics and Alloys in Reduced Gravity	July 1988
	6. Performing Organization Code
7. Author(s)	8. Performing Organization Report No.
S.M. Valone and R.G. Behrens	None (E-4086)
	10. Work Unit No.
	179-10-10
9. Performing Organization Name and Address	11. Contract or Grant No.
Los Alamos National Laboratory Materials Science and Technology Division Los Alamos, New Mexico 87545	C-80011-F
	13. Type of Report and Period Covered
12. Sponsoring Agency Name and Address	Contractor Report Final
National Aeronautics and Space Administration Lewis Research Center Cleveland, Ohio 44135-3191	14. Sponsoring Agency Code

15. Supplementary Notes

Project Manager, Janet B. Hurst, Materials Division, NASA Lewis Research Center.

16. Abstract

Possible microgravity effects are explored in the combustion synthesis of ceramics and alloys from their constituent elements. Molten intermediates are typically present during the combustion process, thereby offering the chance for natural convection to take place. Numerical simulations suggest that the combustion front in concert with gravity may act as a partial "zone-refinement" mechanism which is attempting to sweep out porosity in the sample. Contrary to suggestions by dimensional analysis, no effects on the combustion rate are seen. An analytical model of the combustion velocity as a function of the gravitational field and the spreading rate of molten material gives the correct order of magnitude of the gravity effect as measured by centrifuge experiments.

17. Key Words (Suggested by Author(s))	18. Distribution Statement
Self propagating high temperature synthesis, Combustion synthesis, Reduced gravity, Microgravity	Unclassified - Unlimited Subject Category 24

19. Security Classif. (of this report)	20. Security Classif. (of this page)	21. No of pages	22. Price*
Unclassified	Unclassified	84	A05

NASA FORM 1626 OCT 86

*For sale by the National Technical Information Service, Springfield, Virginia 22161

NASA-Langley, 1988

End of Document